April 1998 • NREL/SR-520-24580

Development of High, Stable-Efficiency Triple-Junction a-Si Alloy Solar Cells

Final Technical Report

X. Deng, S.J. Jones, T. Liu, and M. Izu
Energy Conversion Devices, Inc.
Troy, Michigan

National Renewable Energy Laboratory
1617 Cole Boulevard
Golden, Colorado 80401-3393
A national laboratory of
the U.S. Department of Energy
Managed by Midwest Research Institute
for the U.S. Department of Energy
under Contract No. DE-AC36-83CH10093

NREL/SR-520-24580 • UC Category: 1262

Development of High, Stable-Efficiency Triple-Junction a-Si Alloy Solar Cells

Final Technical Report

X. Deng, S.J. Jones, T. Liu, and M. Izu
Energy Conversion Devices, Inc.
Troy, Michigan

NREL technical monitor: K. Zweibel

National Renewable Energy Laboratory
1617 Cole Boulevard
Golden, Colorado 80401-3393
A national laboratory of
the U.S. Department of Energy
Managed by Midwest Research Institute
for the U.S. Department of Energy
under Contract No. DE-AC36-83CH10093

Prepared under Subcontract No.ZAN-4-13318-11
April 1998

PREFACE

This Final Technical Report covers the work performed by Energy Conversion Devices, Inc. (ECD) for the three phase period July 18, 1994 to February 15, 1998 under the NREL Subcontract ZAN-4-13318-11 entitled "Development of High, Stable-Efficiency Triple-Junction a-Si Alloy Solar Cells". This research was carried out under the general directions of Mr. S. R. Ovshinsky and Dr. Masat Izu. The large area solar cell research using the 5MW a-Si solar cell processor was done in collaboration with the research team at the United Solar System, Corp. (United Solar).

The research was performed by:

X. Deng
J. Evans
M. Izu
S. J. Jones
R. Kopf
T. Liu
K. L. Narasimhan
S. R. Ovshinsky
B. Viers
Y. Xiao

with the help of the entire photovoltaic teams at Energy Conversion Devices, Inc. and United Solar Systems Corp.. We would like to thank Drs. H. Fritzsche , S. Guha, and J. Yang for discussions, experimental help and collaborations throughout all phases of this research. We would also like to thank Dr. R. Gordon (Harvard U.), Dr. D. Han (U. of North Carolina), Dr. S. Hegedus (IEC), Dr. W. Paul (Harvard U.), Dr. E. Schiff (Syracuse U.) and Dr. D. Williamson (Colorado School of Mines) for collaborations. Discussions with Drs. W. Luft, B. von Roedern, and K. Zweibel are deeply appreciated. Help from J. Osman in the preparation of this manuscript is appreciated.

Table of Contents

	Page
Preface	2
Table of Contents	3
List of Figures	4
List of Tables	9
Executive Summary	12
Section 1. Introduction	
Section 2. Improving the Stability of the Intrinsic a-Si Alloy Materials	18
Section 3. Amorphous SiGe Narrow Bandgap Materials and Devices	30
Section 4. Wide Bandgap Solar Cells	42
Section 5. Microcrystalline Silicon Alloy As Novel p Material	55
Section 6. Schottky Barrier Device as an a-Si Alloy Materials Evaluation Tool	60
Section 7. High Rate Deposition of a-Si using VHF Plasmas	66
Section 8. High Rate Deposition of a-SiGe using VHF Plasmas	72
Section 9. Deposition of Microcrystalline Silicon p-layers using VHF process	77
Section 10. Optimization of Single-junction a-Si Solar Cell	94
Section 11. Optimization of Tunnel Junction	103
Section 12. Optimization of Triple-junction a-Si Alloy Solar Cell	113
Section 13. Optimization of Large Area Deposition of a-Si films and solar cells	116
Section 14. Optimization of Large Area Deposition of a-SiGe films and solar cells	124
Section 15. Optimization of Large Area Deposition of Ag/ZnO back reflectors	142
Section 16. Deposition of ZnO by Sputtering from Metal Zn	146
References	148

List of Figures

Figure 1-1 Structure of ECD's triple-junction a-Si alloy solar cell.

Figure 1-2 Schematic drawing of ECD's roll-to-roll solar cell deposition process.

Figure 2-1 PDS spectrum for a-Si:H:F and a-Si:H thin films before and after light soaking.

Figure 2-2a J-V curve for a-Si:H:F device before light soaking measured under AM1.5 spectrum.

Figure 2-2b J-V curve for a-Si:H:F device measured under weak blue and red light.

Figure 2-3a J-V curve for a-Si:H:F device after 1680 hours of one sun light soaking at 50 °C.

Figure 2-3b J-V curve for a-Si:H:F device after 1680 hours of light soaking measured under weak blue and red light.

Figure 2-4 SIMS analysis depth profile for an a-Si:H:F device.

Figure 3-1 Bandgap grading profiles investigated for a-SiGe narrow bandgap solar cells.

Figure 3-2 J-V curve for a single-junction a-SiGe narrow bandgap solar cell measured under AM1.5 light with a 610 nm red filter.

Figure 3-3 J-V curve for an a-SiGe solar cell with double graded bandgap profile, measured under AM1.5 light with a 610 nm red filter.

Figure 3-4 J-V curve for an a-SiGe solar cell after 300 hours of one sun light soaking at 50°C, measured under AM1.5 light with a 610 nm red filter.

Figure 3-5 J-V curve for an a-SiGe cell used as the middle component cell of a triple-junction solar cell.

Figure 4-1 J-V curve for a wide bandgap a-Si single cell showing initial V_{oc}=1.053V.

Figure 4-2 J-V curve for an a-Si device with the i-layer deposited at relatively high temperature (230 °C) and a hydrogen dilution level exceeding the optimum level.

Figure 4-3(a) J-V curve for a wide bandgap a-Si single cell after 2500 hours of one sun 50 °C light soaking, showing 1.014 V stabilized V_{oc} .

Figure 4-3(b) J-V curve for a wide bandgap a-Si single cell after 2500 hours of one sun 50 °C light soaking, measured under weak blue and red lights.

Figure 4-4 J-V curve for a tandem-junction solar cell with wide bandgap a-Si as the top cell intrinsic layer.

Figure 4-5 J-V curve for a tandem-junction solar cell with a regular top i-layer for reference.

Figure 4-6 IR spectrum for an a-Si film deposited at low temperature and high hydrogen dilution.

Figure 4-7 Small Angle X-Ray Scattering spectrum for an a-Si film deposited at low temperature and high hydrogen dilution.

Figure 6-1 J-V curves for a c-Si(n^+)/a-Si/Pd Schottky barrier device measured under (a) solar simulator white light; (b) weak red light; and (c) HeNe laser light.

Figure 6-2 Correlation of FF for Schottky barrier devices and regular a-Si n-i-p solar cell devices having the same i-layer.

Figure 7-1 Cell efficiencies before and after 1000 hours of one sun light soaking for devices having VHF i-layers deposited at different deposition rates.

Figure 7-2 Light soaking degradation of a VHF device as a function of light soaking time.

Figure 7-3 J-V curve of a single-junction a-Si solar cell with i-layer deposited using VHF plasma, showing η=10.6%.

Figure 8-1 Dependence of V_{oc} on the SiH_4 flow and H_2 dilution..

Figure 8-2 Dependence of V_{oc} on the substrate temperature and applied power.

Figure 9-1 Pareto chart for J_{sc} of n-i-p solar cells with VHF μc-Si p-layer as a function of temperature, BF_3, SiH_4 and deposition time.

Figure 9-2 Response surface plot for J_{sc} as a function of SiH_4 and temperature while keeping the values of BF_3 and deposition time at the center values.

Figure 9-3 Pareto chart for V_{oc} of n-i-p solar cells with VHF μc-Si p-layer as a function of temperature, BF_3, SiH_4 and deposition time.

Figure 9-4 Response surface plot for V_{oc} as a function of deposition time and temperature while keeping the values of BF_3 and SiH_4 at the center values.

Figure 9-5 Pareto chart for P_{max} of n-i-p solar cells with VHF μc-Si p-layer as a function of temperature, BF_3, SiH_4 and deposition time.

Figure 9-6 J-V curve for a representative device with VHF p-layer, showing a V_{oc} of 0.93 V.

Figure 9-7 J-V curve for an a-Si n-i-p device (Sample L2523) with p-layer deposited using the modified VHF PECVD.

Figure 9-8 J-V curve for an a-Si n-i-p device (Sample L2525) with p-layer deposited using the conventional RF PECVD.

Figure 9-9 Quantum efficiency curve for an a-Si n-i-p device (Sample L2523) with p-layer deposited using the modified VHF PECVD, showing high blue response.

Figure 9-10 Quantum efficiency curve for an a-Si n-i-p device (Sample L2525) with p-layer deposited using the conventional RF PECVD.

Figure 9-11 QE curve for an a-Si solar cell with ECD-deposited VHF p-layer and United Solar-deposited n-i layer on a SS/Ag/ZnO substrate, showing an 83% QE at 400nm.

Figure 9-12 RHEED pattern for a device with a VHF p-layer as the top layer, showing high volume fraction of microcrystalline phase in the p-layer.

Figure 10-1 Quantum efficiency spectrum for cell whose ITO was made using a high oxygen pressure.

Figure 10-2 Quantum efficiency spectrum for cell whose ITO was made using a low oxygen pressure.

Figure 10-3 J-V curve for an optimized single-junction a-Si solar cell, showing 10.6% initial efficiency.

Figure 10-4 J-V curve for an optimized single-junction a-Si solar cell measured under weak blue and red lights.

Figure 11-1 J-V curve for an a-Si n-i-p-n tunnel-junction test device with p-layer deposited at different temperatures: (a) 50 ^{o}C; (b) 80 ^{o}C; (c) 120 ^{o}C; and (d) 150 ^{o}C.

Figure 11-2 J-V curve for an a-Si n-i-p-n device with thinner p-layer compared with the device whose data is shown in Figure 11-1.

Figure 11-3 J-V curve for an a-Si n-i-p-n device with thinner n-layer compared with the device whose data is shown in Figure 11-2.

Figure 11-4 J-V curve for an a-Si/a-Si tandem solar cell having an optimized tunnel junction.

Figure 11-5 J-V curve for an n-i-p-n device with a tunnel-junction whose p-layer has a graded doping profile.

Figure 11-6 J-V curve for an n-i-p-n device with a tunnel-junction whose p-layer has a relatively thicker sublayer with less doping.

Figure 12-1 J-V curve of a triple-junction cell after preliminary optimization, showing 11.2% initial efficiency.

Figure 12-2 QE curve of the triple-junction cell showing 11.2% initial efficiency.

Figure 13-1 5MW continuous roll-to-roll a-Si alloy solar cell processor.

Figure 13-2 J-V curve for a typical top cell produced with a large area cathode in the 5MW a-Si solar cell processor.

Figure 13-3 J-V curve for a top cell with V_{oc}=1.00V produced in the 5MW machine.

Figure 14-1 Performance of a-SiGe solar cells with i-layers deposited in a static mode near the exhaust side, the center and the gas inlet side of the cathode burn, showing the unoptimized deposition uniformity with a large area cathode.

Figure 14-2 Deposition uniformity for a-SiGe solar cell before optimization for all of the 10 cathodes used to make the bottom cell a-SiGe layer.

Figure 14-3 Ratio of thickness of films taken from the inlet side of an i-layer burn to the thickness of films taken from the outlet side of the same burn is plotted as a function of deposition rate for several cathodes with the static burns prepared under a variety of deposition conditions, showing that this uniformity problem is strongly related to film deposition rate.

Figure 14-4 Deposition thickness uniformity over large area cathode with different RF power, showing improved uniformity at lower power.

Figure 14-5 Deposition thickness uniformity over large area cathode with different deposition rate, showing high uniformity (I/O uniformity=1) at a desirable deposition rate (Relative deposition rate=1) as required by the machine line speed.

Figure 14-6 Performance of a-SiGe solar cells with i-layers deposited in a static mode near the exhaust side, the center and the gas inlet side of the cathode burn, before and after uniformity optimization.

Figure 14-7 Pareto chart for J_{sc} for a middle a-SiGe solar cell measured under 530 nm filtered light, for the 5-factor middle cell experimental design.

Figure 14-8 Pareto chart for red P_{max} for a middle a-SiGe solar cell in the 5-factor middle cell experimental design.

Figure 14-9 Contour plot of the P_{max} as a function of the applied power and Si_2H_6 flow for a middle Ge/Si ratio. The dark lines represent the contours with the same J_{sc} value, as marked. The point with the highest P_{max} on the 7.0 mA/cm^2 J_{sc} contour line is marked by a cross, indicating a P_{max} value of 3.64 mW/cm^2.

Figure 14-10 Contour plot of the P_{max} as a function of the applied power and Si_2H_6 flow for a higher Ge/Si ratio, compared with the plot in Figure 14-9.

Figure 14-11 Contour plot of the P_{max} as a function of the Si_2H_6 flow and GeH_4/Si_2H_6 ratio with a high RF power.

Figure 14-12 Contour plot of the P_{max} as a function of the Si_2H_6 flow and GeH_4/Si_2H_6 ratio with a lower RF power.

Figure 14-13 J-V curve for a typical a-SiGe middle cell after preliminary process optimization.

Figure 15-1 QE curve for an a-SiGe solar cell deposited on an optimized Ag/ZnO back-reflector made in the 5MW back-reflector sputtering machine.

List of Tables

Table 2-1 Deposition conditions for a-Si:H:F materials using F_2/He and reference a-Si:H material.

Table 2-2 Solar cell data for an a-Si:H:F device after different light soaking step.

Table 2-3 Comparison of the amount of light soaking degradation for an a-Si:H:F device and a-Si:H reference device.

Table 3-1 Cell data for a-SiGe devices made with and without air exposure after each layer deposition.

Table 3-2 J-V properties for n-i-p cells made with the Harvard a-SiGe material.

Table 3-3 Device performances of three a-SiGe solar cells with different Ge contents in the i-layer deposited on SS and BR substrates.

Table 3-4 Device performance of a-SiGe solar cells with different bandgap grading in the a-SiGe i-layer, measured under AM1.5 light.

Table 3-5 Device performance of a-SiGe solar cells with different bandgap grading in the a-SiGe i-layer, measured under AM 1.5 light with a 610 nm cut-on filter.

Table 3-6 Device performance of a-SiGe solar cells with i-layers deposited at different substrate temperatures.

Table 3-7 P_{max} measured under AM1.5 light with 610 nm filter for a-SiGe solar cells with different bandgap grading profiles, after different light soaking times.

Table 3-8 Deposition conditions and device performance for a-SiGe middle component cells deposited on SS.

Table 4-1 Cell performance for devices made at different substrate temperatures.

Table 4-2 Properties for high V_{oc} cells made with different i-layer thicknesses during the initial state and after light soaking for different time periods.

Table 4-3 Data for high V_{oc} devices prepared on bare SS and SS/Ag/ZnO substrates in the same n-i-p deposition.

Table 5-1 Properties for cells made with varying amounts of CO_2 flow while all other parameters were nominally fixed.

Table 5-2 Properties for cells made at different p-layer substrate temperatures while all other parameters were nominally fixed.

Table 5-3 Properties for cells made with varying amounts of CH_4 flow while all other parameters were nominally fixed.

Table 5-4 Properties for cells with μc-Si and μc-SiC p-layers, before and after the devices are exposed to air for an extended period of time.

Table 5-5 Properties for cells made with relatively less hydrogen dilution compared with samples shown in Table 5-4 and varying amounts of CH_4 flow while all other parameters were nominally fixed.

Table 6-1 J-V performance for c-Si (n^+) / a-Si alloy/Pd Schottky barrier devices and a-Si alloy n-i-p solar cells under the illumination of different lights.

Table 7-1 Intrinsic layer growth conditions and the performance of solar cells with VHF i-layers.

Table 7-2 Comparison of light soaking stability between devices with i-layers deposited using RF and VHF.

Table 8-1 Deposition parameters and the experimental results using a Design of Experiments.

Table 8-2 a-SiGe:H cells with i-layers made using VHF at 10 Å/s.

Table 8-3 Properties for a-Si:Ge:H cells prepared at different rates using VHF technique.

Table 9-1 Design parameters and experimental results for the optimization of VHF deposition of microcrystalline p-layer using a 4-factor Draper-Lin small composite design with face-centered design characteristic. Other deposition parameters including VHF power, hydrogen flow and pressure are kept constant for this set of experiments.

Table 9-2 Results for solar cells whose p-layers were deposited using different processes: conventional RF, conventional VHF and a modified VHF process.

Table 10-1 Device performance of single-junction a-Si n-i-p solar cells deposited on bare SS with different i-layer thicknesses, after different light soaking times.

Table 10-2 Performance of reference solar cells coated with different ITO in a routine check of the ITO deposition consistency and reproducibility.

Table 11-1 Performance of solar cell data for n-i-p-n devices with different p- and n-layer deposition temperatures and thicknesses.

Table 11-2 Device performance of triple-junction a-Si/a-SiGe/a-SiGe solar cells with different tunnel-junction n-layer thicknesses.

Table 11-3 The solar cell $V_{oc,}$ FF_r and R_s values for n-i-p and n-i-p-n devices with different p-layers.

Table 13-1 Performance of top component cells as a function of hydrogen dilution, showing an improvement in V_{oc} and FF with increasing H_2 flow. The other deposition conditions such as substrate temperature and RF power are kept constant for these devices.

Table 13-2 Performance of top component cells as a function of top i-layer web temperature during deposition, showing an improvement in FF and J_{sc} with higher substrate temperature. The other deposition conditions such as hydrogen flow and RF power are kept constant for these devices.

Table 13-3 Performance of top component cells as a function of RF power, showing an improvement in V_{oc} and FF with increasing RF power.

Table 14-1 Five-factor Draper-Lin design for the optimization of middle cell a-SiGe i-layer quality.

Table 15-1 Device performance of a-SiGe test solar cells deposited on Ag/ZnO back-reflectors produced in 5MW back-reflector machine with different ZnO sputtering currents.

Table 15-2 Device performance of a-SiGe test solar cells deposited on Ag/ZnO back-reflectors produced in 5MW back-reflector machine using ZnO targets manufactured by different vendors L, T and K.

Table 16-1 Comparison of data for a-Si:H cells co-deposited on Al/ZnO back reflectors. Cell measurements completed using AM1.5 light.

EXECUTIVE SUMMARY

Objectives

The overall objective of this amorphous silicon research program is to develop high efficiency a-Si solar cells and to develop and improve processes for large area deposition of a-Si solar cells and modules. The knowledge obtained and technologies demonstrated in this program will be incorporated into ECD's continuous roll-to-roll deposition process to further enhance its photovoltaic manufacturing technology.

Technology

In ECD's solar cell design, triple-junction a-Si alloy solar cells are deposited onto stainless steel substrates coated with Ag/ZnO back reflector. This type of cell enables us to use a continuous roll-to-roll deposition process to manufacture a-Si PV materials in high volume. Using this design, ECD has previously achieved record high initial solar cell efficiency using the following features: 1) a triple-junction, spectrum splitting solar cell design; 2) a microcrystalline silicon p-layer; 3) a bandgap profiled a-SiGe alloy as the bottom cell i-layer; 4) a high performance Ag/ZnO back reflector; and 5) a high performance tunnel junction between component cells. The research team at United Solar has recently used a similar design to prepare devices with a 13% stable efficiency, a new world record.

Approaches and Accomplishments

In this program, we are further advancing ECD's existing PV technology by performing the following tasks:

Task 1: Optimization of large-area plasma deposition of a-Si films;
Task 2: Optimization of large-area plasma deposition of a-SiGe films;
Task 3: Research on μc-Si p^+ deposition using VHF plasma; and
Task 4: Optimization of a-Si solar cell back-reflector.

In the following, we summarize our research under various tasks of this program.

1. We have explored the deposition of a-Si at high rates using very high frequency (VHF) plasma MHz, and compared these VHF i-layers with RF plasma deposited i-layers. With improved deposition conditions, VHF intrinsic layers deposited at a rate up to 10 Å/s show similar device performance and light stability to VHF and RF i-layers deposited at low rates, and show higher stability than RF i-layers deposited at high rates in the same deposition system. A 10.6% (initial) single-junction solar cell was fabricated using a VHF deposited i-layer.

2. We have conducted comprehensive research to develop a μc-Si p^+ layer using VHF deposition process with the objectives of 1) establishing a wider process window for the deposition of high quality p-materials, and 2) further enhancing the performance of a-Si solar cells by improving its

p-layers. High performance microcrystalline materials with superior properties has been achieved using a modified VHF process. The new process and new p-layer lead to a 6-10% improvements in the solar cell efficiency for single junction solar cells mostly due to enhanced blue light transmission.

3. We have optimized the deposition of the intrinsic a-Si layer and the boron doped μc-Si p^+ layer to improve the V_{oc}. As a result, a V_{oc} of 1.053 V was achieved for a single-junction a-Si n-i-p solar cell. After 2500 hours of light soaking, the stable V_{oc} for this device is 1.014 V. This high V_{oc} is achieved by depositing the intrinsic a-Si layer with high hydrogen dilution of the plasma at a relatively low substrate temperature.

4. We have deposited wide bandgap a-Si films using high hydrogen dilution. Using a VHF deposition, we have deposited solar cell i-layers, at 5 Å/s, which leads to solar cells with V_{oc} of 1.01 V.

5. To reduce the manufacturing cost of our photovoltaic products, we investigated the deposition of the ZnO layer (for use in back-reflector) using a sputter deposition process involving metal Zn targets. The cost of the Zn metal targets is a factor of five less than the ZnO targets presently used in production. Their use in production will lead to a significant cost savings. For these studies, the ZnO layers were evaluated using a single junction solar cell structure. When used in solar back-reflectors, solar cells with ZnO sputtered from metal Zn show similar performance to those from ceramic ZnO targets.

6. We have obtained a baseline fabrication for single-junction a-Si n-i-p devices with 10.6% initial efficiency and a baseline fabrication for triple-junction a-Si devices with 11.2% initial efficiency.

7. We have collaborated with Harvard University to evaluate the Harvard's cathodically deposited a-SiGe material in n-i-p solar cell devices. These devices were then compared with devices having intrinsic layers deposited using the conventional anode deposition technique. We did not find any improvement with use of this cathodically deposited a-SiGe over a-SiGe narrow bandgap material deposited on anode at ECD.

8. We have optimized the deposition parameters for a-SiGe with high Ge content. A bandgap profiled a-SiGe alloy solar cell demonstrates a maximum power output (P_{max}) of 3.6 mW/cm^2 measured under a Xenon solar simulator with a 610 nm cut-on optical filter. After 300 hours of one-sun light soaking, the P_{max} measured with 610 nm filter for this device is stabilized at 2.94 mW/cm^2.

9. We designed a novel structure for the p-n tunnel junction (recombination layer) in a multiple-junction solar cell. In this structure, the doping level of the p-layer is graded so that the sublayer near the p-n tunnel junction has heavier doping to reduce the series resistance and the sublayer near the p-i interface has less doping to maintain a high V_{oc}. We have demonstrated the

improved tunnel junction in the solar cell using an n-i-p-n device structure, which is a standard single-junction n-i-p device with a tunnel junction stacked on top.

10. We have demonstrated, in n-i-p solar cells, the improved stability of a-Si:H:F materials when deposited using a new fluorine precursor. Single-junction n-i-p solar cells with 3000Å to 3500Å thick a-Si:H:F intrinsic layers were deposited onto Ag/ZnO back-reflectors. The initial efficiency of the a-Si:H:F devices were around 9%, which was the same as the baseline unfluorinated a-Si:H n-i-p solar cells deposited in the same deposition system. After 1680 hours of one sun light soaking at 50 °C, the a-Si:H:F devices showed a 13% degradation, which is lower than the 17% degradation usually seen for the baseline a-Si:H n-i-p devices with a 3000Å thick i-layer after the same amount of light soaking.

11. We have investigated the use of a c-Si(n^+)/a-Si alloy/Pd Schottky barrier device as a tool for the effective evaluation of photovoltaic performance of a-Si alloy materials. In this device, the intrinsic a-Si alloy materials are deposited onto a heavily doped n^+ crystalline silicon wafer and a thin layer of palladium (Pd) is subsequently evaporated on top to complete the device structure. The fill factor for such a device under weak red-light reflects the minority carrier transport properties, just as in a real solar cell. We compared the J-V characteristics of these Schottky barrier devices with standard a-Si and a-SiGe n-i-p solar cells having the same intrinsic layer, and established a good correlation between the fill factors of these two type of devices. The c-Si(n^+)/a-Si alloy/Pd device offers a convenient technique to reliably evaluate the material performance in a solar cell device.

12. Through alternations in the deposition conditions and system hardware, we have improved our understanding for the deposition of uniform and high quality a-Si and a-SiGe films over large areas. This improvement has led to the achievement of uniform deposition of a-SiGe films in terms of both film thickness and Ge content over large areas. For the a-Si top solar cell, solar cells with fill factor (FF) up to 0.73 and open circuit voltage (V_{oc}) up to 1.00 V have been achieved over a large area.

13. We have performed extensive research to optimize the deposition process of the newly constructed 5MW back-reflector deposition machine. With our optimized highly textured and highly reflective Ag/ZnO back-reflector, we have prepared a-SiGe solar cells with short circuit currents J_{sc} of 25.6 mA/cm^2, indicating high performance of the back-reflector.

Section 1
Introduction

During the past fifteen years, ECD has pioneered and developed a unique, proprietary a-Si based PV technology embodying several important innovations.[1-15] These include: 1) a record-setting, high efficiency, triple-junction spectrum-splitting thin-film a-Si alloy device structure; and 2) a fully automated roll-to-roll continuous substrate thin-film solar cell manufacturing process.

Record high solar cell efficiencies have been achieved by ECD and its PV joint venture United Solar Systems, Corp. (United Solar) using the following features: 1) a triple-junction solar cell design;[3] 2) a microcrystalline silicon p-layer;[4] 3) a bandgap profiled a-SiGe alloy as the bottom cell intrinsic layer;[5] 4) a high performance Ag/ZnO back-reflector; and 5) a high performance tunnel junction between the component cells. Using these features, United Solar recently achieved a 10.2% stable triple-junction a-Si alloy solar panel with over 1 ft^2 area,[9] and a 14.6% initial and 13% stable efficiencies for small area a-Si alloy solar cells.[14] ECD has achieved 4 ft^2 production modules with 9.5% initial and 8% stable module efficiencies using a 2 MW continuous roll-to-roll manufacturing line.[7] All of these have established world records. Under this Amorphous Silicon Research program, we are further advancing this technology to meet long-term efficiency and cost goals set by the Department of Energy.

The overall objective of this amorphous silicon research program is to develop high efficiency a-Si solar cells and to develop and improve processes for large area deposition of a-Si solar cells and modules. The knowledge obtained and technologies demonstrated in this program will be incorporated into ECD's continuous roll-to-roll deposition process to further enhance its photovoltaic manufacturing technology.

This research consists of studies on small and large area deposition issues critical to the improvement of the existing a-Si PV technologies. The specific program tasks are in the following four areas:

Task 1: Optimization of large-area plasma deposition of a-Si films;
Task 2: Optimization of large-area plasma deposition of a-SiGe films;
Task 3: Research on μc-Si p^+ deposition using VHF plasma; and
Task 4: Optimization of a-Si solar cell back-reflector.

In ECD's solar cell design, triple-junction a-Si alloy solar cells are deposited onto a SS substrate coated with Ag/ZnO back-reflector layers (see Figure 1-1). This type of cell design enables us to use a continuous roll-to-roll deposition process (see Figure 1-2) to manufacture a-Si PV materials in high volume at low cost.

On the small-area solar cell research, we are primarily utilizing three PECVD systems designated as Load Lock 1 (LL1), Load Lock 2 (LL2), and the Box System to perform deposition of materials and devices. The first two systems are multi-chambered, load-locked systems and the Box System is a single chamber deposition system. The LL1 system consists of six chambers: a

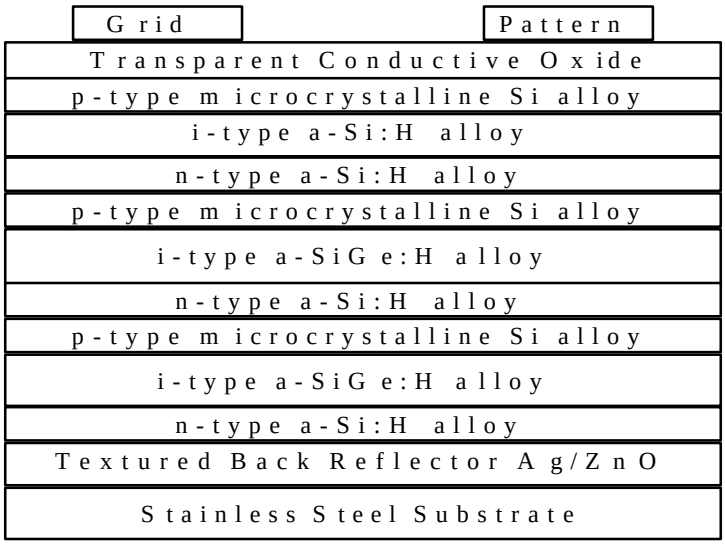

Figure 1-1 Structure of ECD's triple-junction a-Si alloy solar cell.

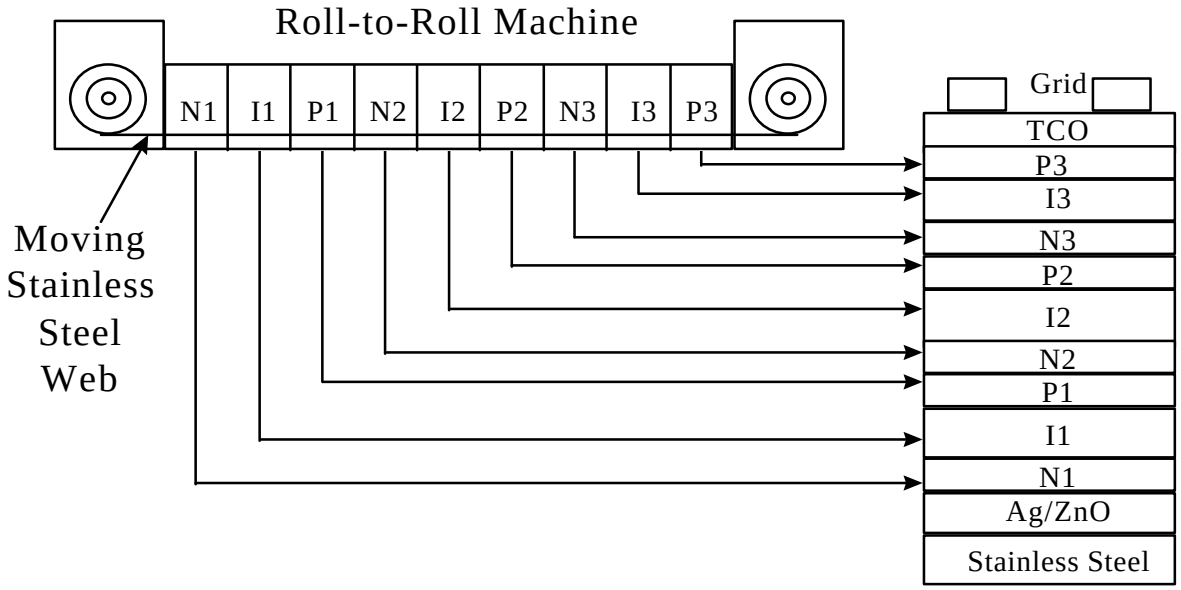

Figure 1-2 Schematic drawing of ECD's roll-to-roll solar cell deposition process.

load chamber, an n chamber, a p chamber, an i chamber for the standard intrinsic layer deposition, a semi-i chamber for miscellaneous research studies including the a-Si:H:F study, and a transfer jar at the center for substrate-holder transportation. In this system, all of the chambers are isolated by gate valves to minimize cross contamination. The LL2 system consists of three chambers, an n/load chamber, a p-chamber, and an i-chamber. Again, all of these chambers are isolated by gate valves. For the large-area deposition research, described in Sections 13-15, we used the 5 Megawatt (MW) continuous roll-to-roll solar cell processing line that ECD designed and built for United Solar, in collaboration with a team of scientists at United Solar. This work was part of the initial optimization of this production line. The line is now in full production mode.

This report summarizes the main results of the research effort under this subcontract. In Section 2, we describe our experimental results that demonstrate improved stability for a-Si:H:F materials. In Section 3, we summarize our collaboration study with Harvard to evaluate the use of their cathodically deposited a-SiGe in a n-i-p solar cell structure, and the optimization of a-SiGe deposition using the LL2 system. In Section 4 we discuss our research efforts to improve the V_{oc} of the wide bandgap solar cells and the achievement of a 1.053 V initial and a 1.014 V stable open circuit voltages. In Section 5, we describe our efforts to develop novel μc-Si alloy materials for use as solar cell p-layers. In Section 6, we report on our development of a Schottky barrier device for use as a materials evaluation tool for a-Si alloy materials. In Section 7, we describe the use of VHF plasmas to achieve the deposition of stable, high-quality a-Si films and i-layers at a rate of 10 Å/s. In Section 8, we describe initial studies of the use of a VHF plasma to prepare a-SiGe cells at high rates. In Section 9, we describe the fabrication of improved μc-Si p-layers using a modified VHF process. In Section 10, we summarize our work involving single junction device research, including the study of ITO deposition for the top electrode. In Section 11, we describe our attempts to develop novel microcrystalline silicon alloys (with C and O) for solar cell p-layers. In Section 12, we highlight our work involving the fabrication of triple-junction solar cells and the fabrication of triple-cells with 11.2% initial efficiencies. In Section 13, we describe our research work in the area of large-area deposition of a-Si using 5 MW production machines, together with the research team at United Solar. In Section 14, we discuss issues related to large area deposition of a-SiGe alloys, including the uniformity and the material quality. In Section 15, we summarize the optimization work on Ag/ZnO and Al/ZnO large-area back-reflectors using the 5 Megawatt back-reflector sputter machine. In Section 16, we describe the deposition of high quality ZnO films using metal zinc sputtering targets in an effort to reduce material cost.

Section 2
Improving the Stability of the Intrinsic a-Si Alloy Materials

2.1 Introduction

Early research at ECD revealed an improvement in the quality of hydrogenated amorphous silicon (a-Si, also denoted as a-Si:H) through appropriate incorporation of fluorine into the material.[1] The beneficial effect is believed to be due to the stronger Si-F bonding which reduces the light-induced degradation, and passivates the weak and dangling bonds.

2.2 a-Si:H:F Materials

To study the effect of fluorine incorporation on the stability of a-Si material, we have recently extended the research and investigated the deposition of fluorinated amorphous silicon (a-Si:H:F) materials using fluorine (F_2) diluted in helium as the source gas.[6] It was found that this a-Si:H:F material showed a lower stable density of defect states after light soaking when compared with samples deposited in the same reactor without fluorine.

In that study, fluorinated a-Si was prepared with a gas mixture of SiH_4 or Si_2H_6 and F_2 diluted in He at substrate temperatures up to 430 ^oC. Table 2-1 lists the deposition conditions for a typical a-Si:H:F film (F1) together with two a-Si:H films (H2 and H3) used as references. Sample H2 was made at the same temperature and with the same gas mixture as sample F1 except without F_2. The high temperature (430 ^oC) and high negative bias (-150 V) on the substrate will likely promote F mobility on the growth surface, which consequently leads to a high-quality material.

Table 2-1. Deposition conditions of a-Si:H:F material using F_2/He and reference a-Si:H material.

Sample	Type	Gas Mixture	Pressure (mTorr)	T_s (C)	Power (W)	Bias (V)	Time (min)	Thickness (μm)
F1	a-Si:H:F	Si_2H_6:F_2:He=1:1.7:40	250	430	10	145	300	2.1
H2	a-Si:H	Si_2H_6:He=2.7	250	430	4	69	40	1.8
H3	a-Si:H	SiH_4	250	250	2	16	150	2

We light soaked samples F1, H2 and H3 under approximately 800 mW/cm^2 of white light for 72 hours. The Photothermal Deflection Spectroscopy (PDS) spectra of these three samples before (F1a, H2a, H3a) and after (F1b, H2b, H3b) light soaking are shown in Figure 2-1. The density of defect states (N_s), calculated from PDS absorption spectra are also given in Figure 2-1. Although the density of defect states for sample F1 is higher than for sample H3 in the initial state, the

defect density for sample F1 is the lowest among the three samples in the degraded state. The low stable defect density in a-Si:H:F is possibly due to the strong passivation of dangling bonds and the elimination of weak bonds by fluorine. Since F is the most electronegative of the elements, it bonds to Si almost twice as strongly as H. When properly incorporated, F can replace weakly bonded H and passivate dangling and weak bonds more efficiently. Structural changes due to the enhanced film surface etching with F during deposition might lead to improved material stability.

2.3 a-Si:H:F Solar Cell Device Deposited Using F_2/Ne as a Source Gas

We have studied the deposition of a-Si:H:F material using F_2 diluted in neon and used solar cell performance to evaluate the quality and stability of these a-Si:F:H materials. The n-i-p structures were deposited onto bare SS or SS/Ag/ZnO substrates. The Ag/ZnO back reflector layers were deposited previously in ECD's continuous roll-to-roll back-reflector sputtering machine. As in the standard cell fabrication process, ITO top contacts were reactively evaporated onto the existing SS/n-i-p structures. Ag grids were then evaporated onto the ITO using a separate evaporator to complete the device.

We have deposited a-Si:H:F devices with 3000Å thick intrinsic layers. These devices were deposited using a variety of conditions including different F_2/Ne flow rates, different deposition temperatures for the i-layer, and with and without the a-Si buffer layers on both sides of the a-Si:H:F i-layer. As a result, we found that all of the fluorinated devices in this group showed lower conversion efficiency compared with the standard unfluorinated a-Si:H n-i-p devices. Also, the light soaking degradation of these a-Si:H:F devices did not exhibit an improvement from that of a-Si:H devices. Therefore, addition of F_2/Ne into the gas mixture does not seem to produce material with improved stability compared with standard glow discharge deposited a-Si:H.

In order to understand the lack of an improvement, we have analyzed the intrinsic material deposited using F_2 as the source gas. There is about 0.5 to 1% oxygen in these a-Si:H:F materials as measured by Auger and Wavelength Dispersive Spectroscopy. This unwanted oxygen may be incorporated into the material from the F_2 gas source. According to the gas analysis report, the purity of F_2 was 97.5% before it was mixed with Ne. In the 2.5% contaminates of F_2 gas, there is a significant amount of oxygen, which may be responsible for the oxygen contamination in the a-Si:H:F films deposited using F_2/Ne. Unfortunately, F_2 with 97.5-98% purity is the purist F_2 gas available on the market. It is also known from the study of Knight et al.[16] that the addition of Ne to the gas plasma can lead to the formation of columnar film microstructure and the possibility of oxygen being incorporated upon exposure to air. This may also be why the films made with F_2/He seem to be better than those made with F_2/Ne.

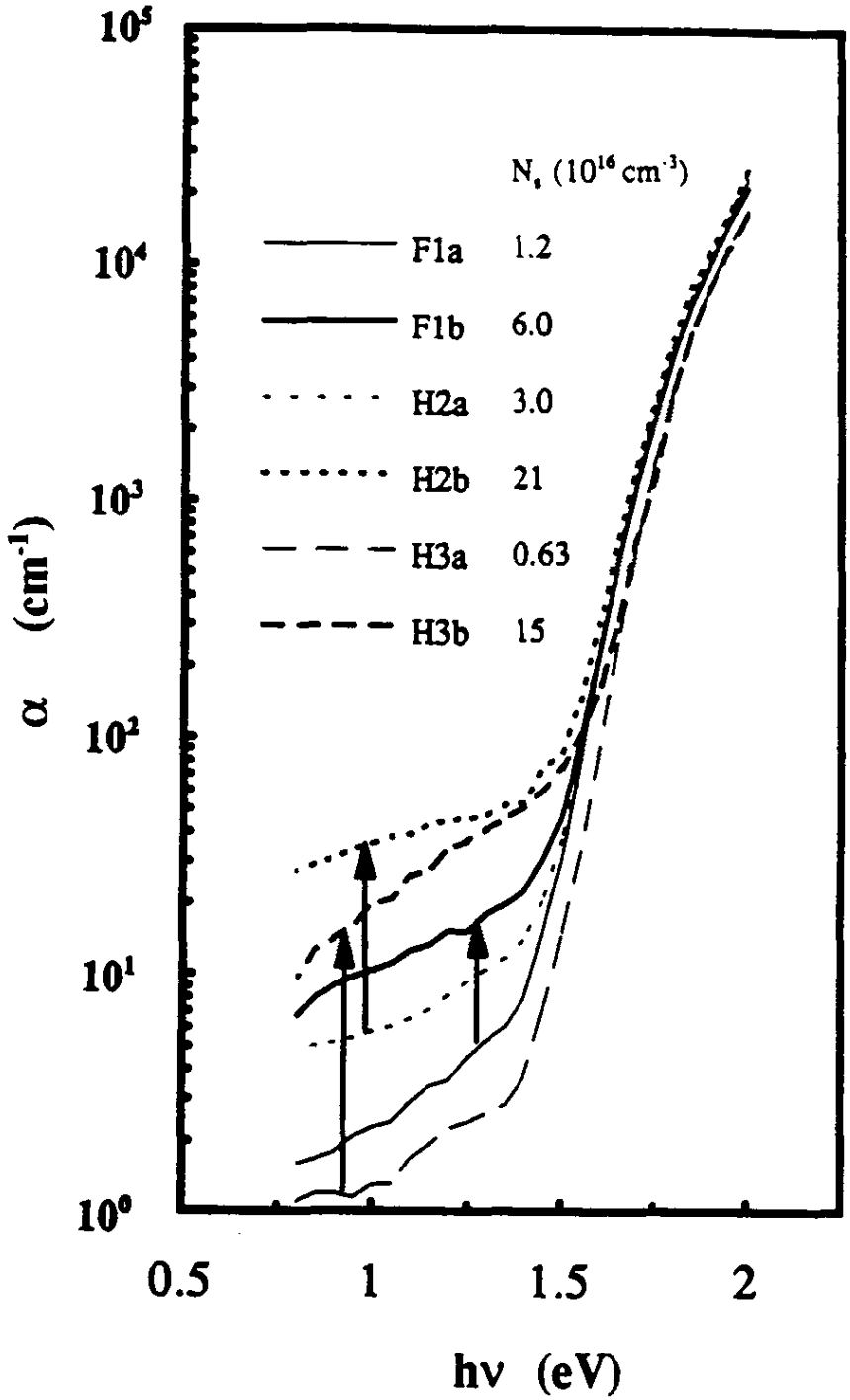

Figure 2-1 PDS spectrum of a-Si:H:F and a-Si:H thin films before and after light soaking.

2.4 a-Si:H:F Devices with Improved Stability Using New Fluorine Precursor

In order to reduce the contamination induced from the source gas, we identified a new fluorine precursor with 99.99% purity. This new precursor can be mixed with hydrogen for dilution, and it produces only atomic fluorine in plasma rather than silicon fluoride radicals. Therefore, fluorine would preferably bond to silicon in a monofluoride form.

With this a-Si:H:F material as an intrinsic layer, n-i-p solar cells were deposited on SS/Ag/ZnO back-reflectors in the LL1 deposition system. The n- and p-layers were standard doped layers for single-junction devices. The a-Si:H:F intrinsic layers were deposited under the following conditions:

Gas mixture:	52 sccm H_2, 1.5 sccm of Si_2H_6, and 0.1 sccm of fluorine precursor
Temperature:	300°C
Power:	5 Watt
Pressure:	600 mTorr
Time:	22 min. at a deposition rate of 2.3 Å/s

The a-Si:H:F layer thickness is around 3000Å. Figure 2-2(a) is a J-V curve of such an a-Si:H:F single-junction solar cell before light soaking. Figure 2-2(b) is the same device measured under weak blue and red light. The initial solar cell efficiency is 9.0%, which is approximately the same as the efficiency for the baseline a-Si:H device deposited in this deposition system.

We have light-soaked this and a number of other a-Si:H:F single-junction solar cell devices under one sun light at 50 ^{o}C. After 1680 hours of light soaking, the solar cell showed a degraded efficiency of 7.9%, representing a 12 % drop in efficiency with light soaking. Figure 2-3a is the J-V curve for this device under AM1.5 light after 1680 hours of light soaking. Figure 2-3b is the J-V curve under weak blue and red light after 1680 hours of light soaking.

Table 2-2 lists the J-V data after each light soaking step for this a-Si:H:F device prepared without the benefit of the Ag/ZnO back reflectors. From the table, we find that the degradation has already come to a saturation point after 97 hours of light soaking.

In comparison, unfluorinated a-Si:H n-i-p solar cells deposited in the same reactor with similar deposition conditions show higher degradation after similar light soaking treatments. For example, the baseline a-Si:H single-junction solar cells without fluorine also have initial efficiencies of 9% for this deposition system. The light soaking degradation after 1000 hours is typically 16-20% for devices with 3000Å thick intrinsic a-Si:H layers. Table 2-3 lists the light soaking data for the a-Si:H:F device and the a-Si:H reference device. From these data, we conclude that the fluorine incorporation into these a-Si:H:F films has led to improved stability.

Table 2-2 Solar cell data of an a-Si:H:F device (LL945) after different light soaking steps under one sun at 50°C.

Light Soaking	Substrate	Dot	V_{oc} (V)	J_{sc} (mA/cm^2)	FF	Eff	FF_b	FF_r
0 hrs.	SS	32	0.937	10.23	0.625	5.99	0.738	0.625
0 hrs.	BR	22	0.932	15.37	0.638	9.14	0.744	0.661
0 hrs.	BR	24	0.934	14.49	0.642	8.69		
0 hrs.	BR	32	0.931	15.16	0.636	8.89	0.741	0.663
0 hrs.	BR	33	0.931	15.05	0.637	8.93	0.738	0.664
97 hrs.	BR	32	0.897	14.89	0.596	7.96	0.679	0.595
384 hrs.	BR	11	0.896	15.12	0.589	7.97	0.676	0.589
384 hrs.	BR	12	0.896	14.91	0.589	7.87	0.673	0.585
384 hrs.	BR	13	0.897	14.33	0.59	7.58	0.678	0.589
384 hrs.	BR	22	0.896	15.1	0.592	8.01	0.671	0.589
384 hrs.	BR	23	0.897	14.72	0.591	7.8	0.677	0.591
384 hrs.	BR	31	0.897	15.54	0.596	8.3		
384 hrs.	BR	41	0.897	15.15	0.597	8.12	0.68	0.595
384 hrs.	BR	43	0.897	14.42	0.592	7.66	0.671	0.591
1056 hrs.	BR	11	0.885	15.13	0.592	7.92	0.672	0.59
1056 hrs.	BR	12	0.885	14.91	0.589	7.77	0.674	0.587
1056 hrs.	BR	22	0.883	15.05	0.589	7.82	0.672	0.591
1056 hrs.	BR	31	0.883	15.45	0.594	8.1	0.666	0.583
1056 hrs.	BR	43	0.883	14.43	0.592	7.59	0.676	0.59
1680 hrs.	BR	11	0.888	15.03	0.588	7.85	0.672	0.584
1680 hrs.	BR	12	0.886	14.9	0.59	7.78	0.667	0.584
1680 hrs.	BR	22	0.887	15.15	0.589	7.92	0.671	0.587

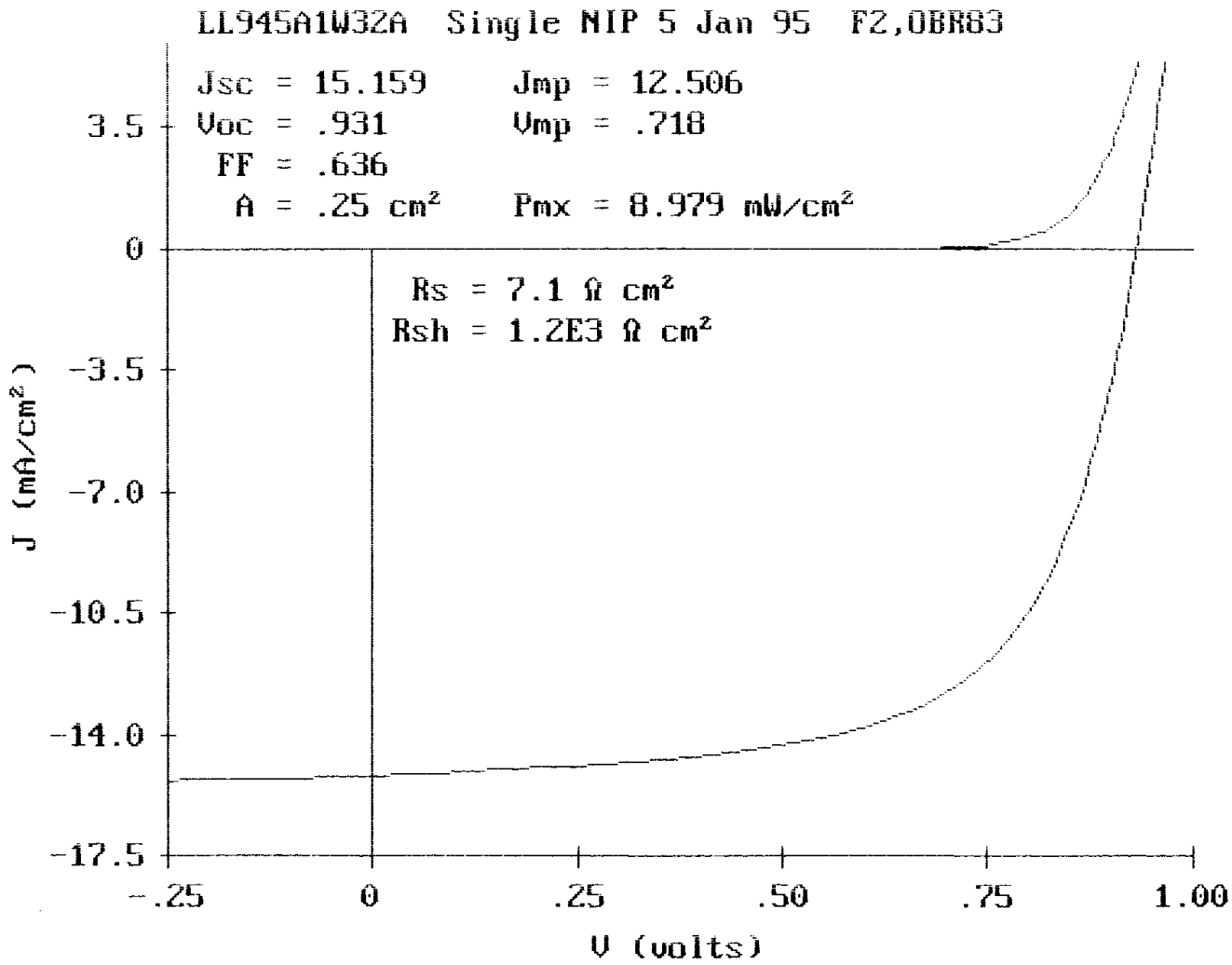

Figure 2-2a J-V curve of a-Si:H:F device before light soaking measured under AM1.5 spectrum.

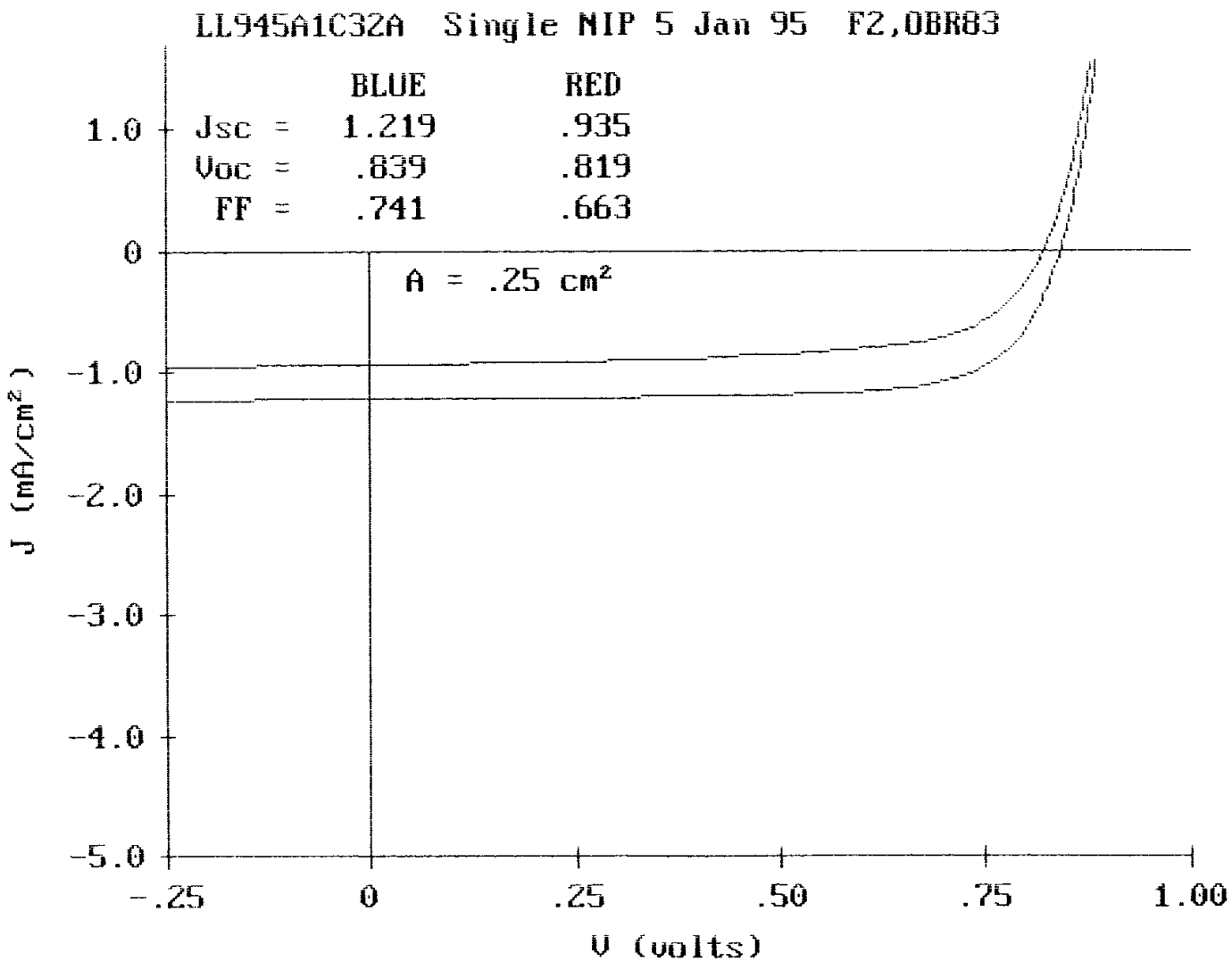

Figure 2-2b J-V curve of a-Si:H:F device measured under weak blue and red light.

Table 2-3 Comparison of the light soaking degradation of an a-Si:H:F single-junction solar cell and an a-Si:H reference single-junction solar cell.

Solar cell i-layer	Light soaking	V_{oc} (V)	J_{sc} (mA/cm^2)	FF	Eff (%)	Drop in Efficiency
a-Si:H:F	0 hrs	0.932	15.37	0.638	9.14	------
on Ag/ZnO	380 hrs	0.896	15.10	0.592	8.01	12.3%
	1680 hrs	0.887	15.15	0.589	7.92	13.3%
a-Si:H	0 hrs	0.951	10.86	0.601	6.21	------
on SS	380 hrs	0.916	10.29	0.554	5.22	15.9%
	620 hrs	0.910	10.38	0.550	5.20	16.3%

2.5 Discussion

Having demonstrated the improved stability of a-Si:H:F devices, an important question that needs to be answered is: what is the function of fluorine and how much fluorine is actually incorporated into these films? To answer these questions, SIMS measurements were completed to identify the amount of fluorine in these samples. Figure 2-4 is a SIMS analysis depth profile measured at Evans East, Inc. for the a-Si:H:F device which had an 8% stable efficiency. To our surprise, the amount of fluorine in this film is only on the order of $1.0\times10^{18}/cm^3$. A sample made without fluorine precursor in the gas mixture shows a small fluorine concentration of about $5\times10^{17}/cm^3$, which may have been incorporated from the walls of the deposition chamber that was also used to deposit both the a-Si:H:F and a-Si:H materials.

There could be three mechanisms in which fluorine in the gas plasma improves material stability: 1) fluorine incorporation reduces the amount of weak bonds; 2) fluorine incorporation reduces dangling bonds; and 3) etching from fluorine plasma helps to produce a denser amorphous material which is more stable.

Since we have detected a concentration of only $1.0\times10^{18}/cm^3$ fluorine in a device with the improved stability, the majority of weak bonds would not have a fluorine nearest neighbor. If the weak bond reduction case holds true, it would have to be an indirect result of the conditions surrounding material growth rather than the chemical composition of the material. Therefore, it is more likely that the improved stability in the a-Si:H:F is from a reduction in dangling bonds and/or production of a denser material from etching of fluorine plasma.

2.6 Summary

Appropriate use of fluorine based gases during the making of a-Si:H material has improved its stability. This improvement is demonstrated in solar cell devices. The amount of fluorine found in the more stable material is on the order of 1.0×10^{18} $/cm^3$. It is likely that the use of fluorine

improves the materials stability through 1) dangling bond reduction, and/or 2) fluorine plasma etching which produces a denser material with higher stability.

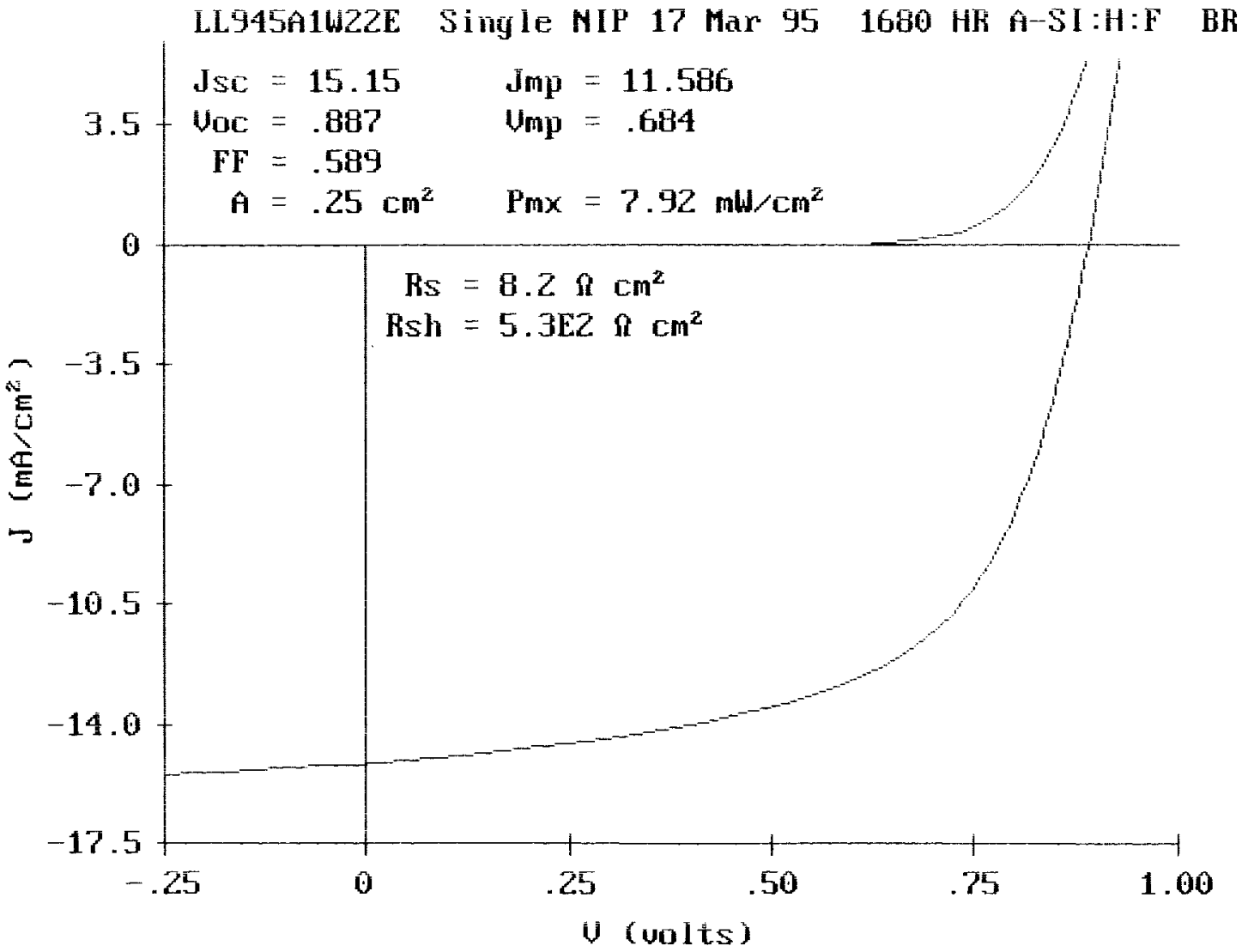

Figure 2-3a J-V curve of a-Si:H:F device after 1680 hours of one sun light soaking at 50 °C.

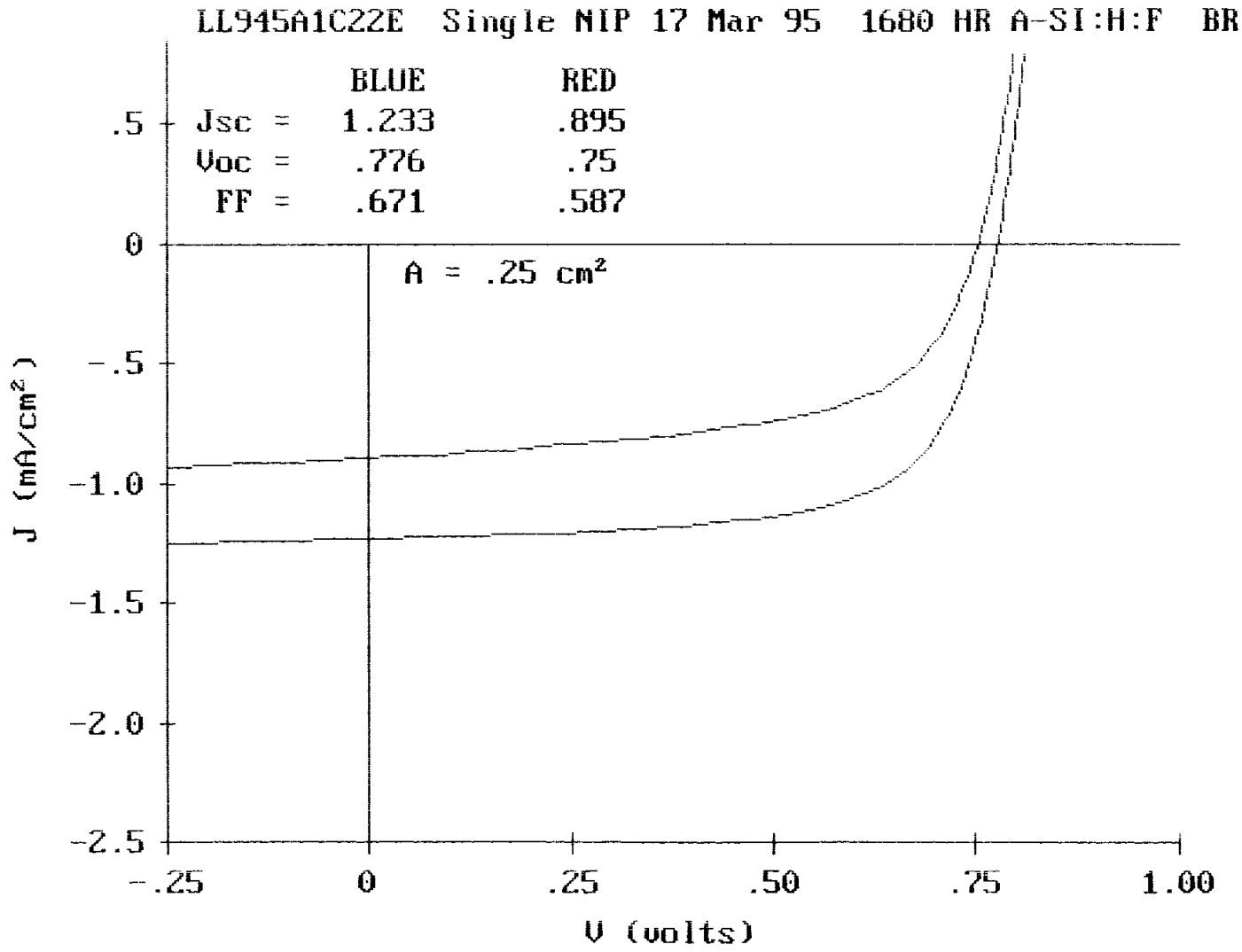

Figure 2-3b J-V curve of a-Si:H:F device after 1680 hours of light soaking measured under weak blue and red light.

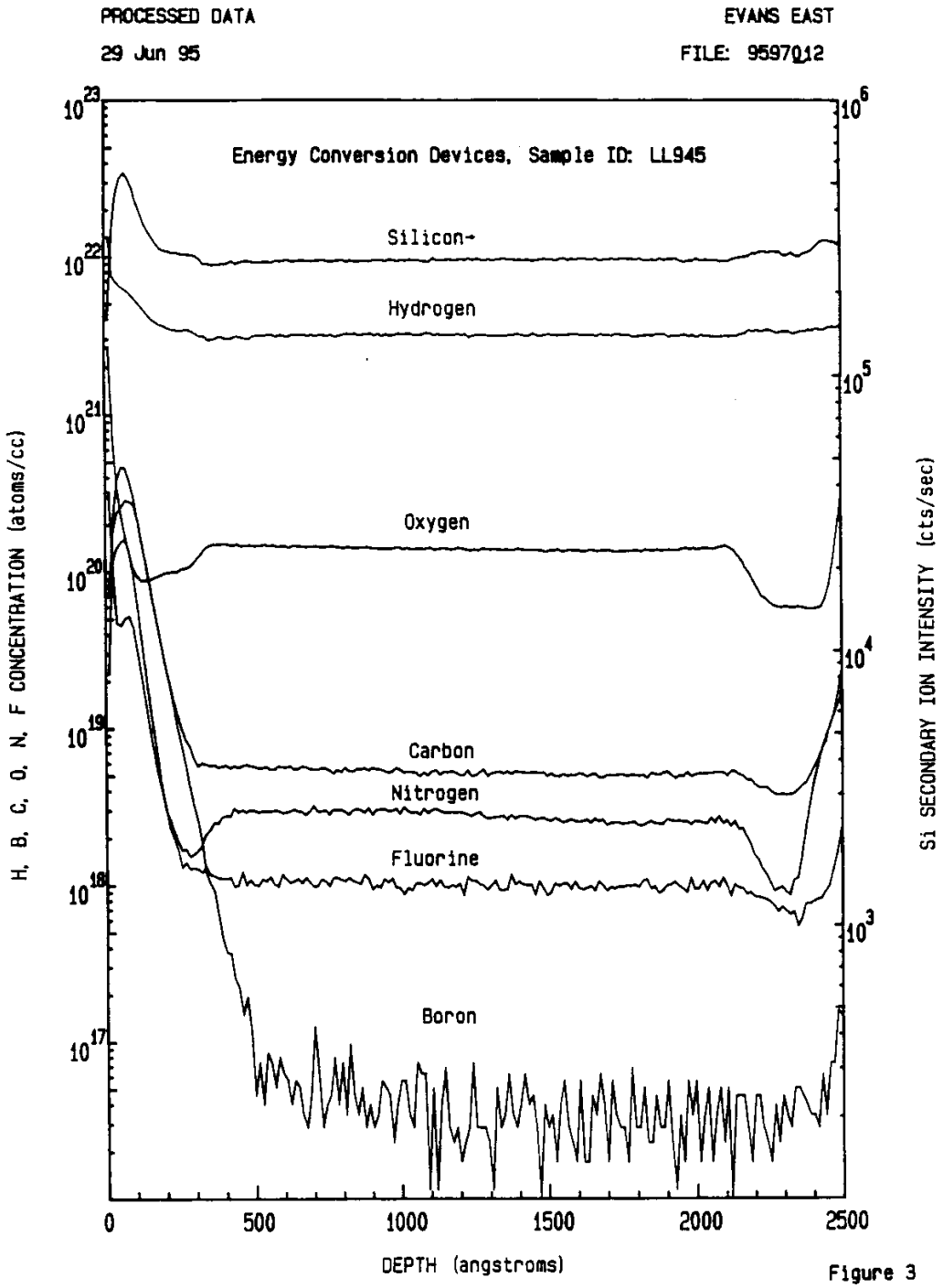

Figure 3

Figure 2-4 SIMS analysis depth profile of an a-Si:H:F device.

Section 3
Amorphous SiGe Narrow Bandgap Materials and Devices

3.1 Introduction

ECD has pioneered the development of high quality low bandgap a-SiGe and developed proprietary deposition conditions to produce high quality a-SiGe with a 1.4 eV to 1.5 eV bandgap. This material was used to achieve 13.7% initial efficiency for triple-junction a-Si alloy solar cells.

To better utilize the long wavelength part of the solar spectrum and achieve a higher efficiency multiple-junction a-Si alloy solar cell, we need to develop a higher quality material with still lower bandgap for the bottom cell intrinsic layer. In particular, a 1.3 eV bandgap alloy with properties that are at least comparable with those for the current 1.5 eV alloy is desired.

The deterioration in the material and cell properties with increased Ge content beyond 20 at. % is well documented. However, improvements in the properties of a-Ge and Ge-rich a-SiGe alloys with increased ion bombardment of the growing surface have been suggested. In particular, Aoki et al.[17] using an ECR microwave plasma process found that the optoelectronic properties of a-Ge are improved when a negative bias of around 150 V is applied to the substrate. Also, Paul et al.[18] of Harvard University and Karg et al.[19] from Siemens have found that a-Ge and Ge-rich a-SiGe alloys deposited on the cathode have much better optoelectronic and structural properties. In the case of a-Ge, the photoconductivity of this material deposited on the cathode is two orders of magnitude better ($\eta\mu\tau = 3\times10^{-7}$ cm^2/V) and the density of defect states is one magnitude lower ($N_s=5\times10^{16}$ /cm^3 and at 0.7 eV α=8.3 cm^{-1}) than the best a-Ge deposited on the anode, the electrode which is typically used to produce device quality a-Si. While not proven, it has been speculated that the improved properties are a result of the relatively high amount of ion bombardment of the cathode surface.

While it does seem that the material properties for Ge-rich a-SiGe alloys are improved with some amount of ion bombardment, these types of alloys have yet to be incorporated into a device. Thus in terms of solar cell use, they have not been truly tested. As part of our work, we have completed a collaborative effort with the Harvard group to incorporate their a-SiGe into n-i-p devices. Several devices have been made and the results are discussed below.

3.2. Collaboration with Harvard to Demonstrate the Cathode Deposited a-SiGe in Solar Cells

Using n- and p-layers produced at ECD using the LL1 system, several devices have been made using Harvard's alloy as the i-layer. The exact procedure followed in making these devices is listed below:

1) n-layers were deposited on SS substrates at ECD using LL1;

2) the day after n-layer deposition, a-SiGe i-layers were grown at Harvard. (In some cases, a thin a-Si buffer layer was then deposited without breaking vacuum);

3) on the third day, the i-layer/buffer layer surface was "cleaned" using a short hydrogen plasma etch and a p-layer was then deposited, again using LL1 at ECD; and finally

4) ITO/Ag contacts were deposited and the cells were measured at ECD.

We found that it was not necessary to etch the n-layer surface prior to depositing the i-layers. To test the effects of exposing each layer to air prior to the next deposition, we made two a-SiGe devices under nominally the same conditions except in one case each layer was exposed to air prior to the next deposition, while for the other device the n-i-p section was made without breaking vacuum. The cell performances for both of these devices are shown in Table 3-1. These devices were made without a full scan of deposition parameter space to find the optimum conditions for a V_{oc} =0.45 V device prepared in this particular system. With the air exposure, slightly lower J_{sc}, V_{oc} and FF are obtained. However, the FF measured using weak red light (FF_r), a parameter typically used to judge bottom cell i-layer quality, is similar for both of the devices. Thus, we chose to use FF_r as a measure of the quality of the Harvard material.

Table 3-1 Cell data for a-SiGe devices made with and without air exposure after each layer deposition.

Run Number	Air Exposure?	J_{sc} (mA/cm^2)	V_{oc} (V)	FF	FF_r	P_{max} (mW/cm^2)
LL986	No	14.3	0.46	0.39	0.45	2.5
LL996	Yes	13.3	0.43	0.37	0.45	2.0

The properties for the cells made with the Harvard a-SiGe material are listed in Table 3-2. For comparison, data for a device (LL 996) made in LL1 with a V_{oc} =0.43 V are also included in the table. During the preparation of this device, it was exposed to air overnight after both the n and i-layer depositions to mimic the conditions the Harvard samples were prepared under. For all of the devices listed in the table, the i-layer thicknesses were measured and found to be between 1500 and 2000Å. As can be seen from the table, devices with two different bandgaps were made, with and without buffer layers. While these parameters were varied, no discernibly large differences in FF_r can be seen between the data for the Harvard and ECD prepared devices. Since the conditions used for making the ECD device may not have been optimum, larger FF_r may be obtainable for Ge-rich devices made on the anode.

Table 3-2 J-V Properties for n-i-p solar cells made with the Harvard a-SiGe material.

Devices	E_g (eV)	Buffer Layer?	V_{oc} (V)	FF_r
Harvard 483A	1.4	No	0.42	0.39
Harvard 483D	1.4	No	0.44	0.39
Harvard 485A	1.4	No	0.42	0.38
Harvard 485D	1.4	No	0.45	0.41
Harvard 498	1.4	No	0.44	0.43
Harvard 502	1.4	Yes	0.50	0.41
Harvard 501	1.5	No	0.53	0.45
Harvard 500	1.5	Yes	0.55	0.44
ECD LL996	-	No	0.43	0.45

The fact that the devices prepared on the cathode do not show larger FF_r than those for anode deposited cells is consistent with the average hole transport properties for the Harvard material. Ambipolar diffusion lengths of 600-700Å were obtained at Harvard for the cathode deposited material, assuming a surface recombination velocity of zero. If a surface recombination velocity of infinity is assumed, one obtains diffusion lengths from 130 to 170Å. Since the cell performance for a-Si devices are limited by the hole transport, it is not surprising that we were unable to prepare superior devices by straight incorporation of the Harvard material into a cell structure.

3.3 Optimization of a-SiGe Bottom Cell

After Phase I of the program, we installed the new LL2 deposition system. As part of the installation procedures, we optimized the deposition of narrow bandgap a-SiGe solar cells using techniques previously developed at ECD.[5] Three bandgap profile schemes: 1) a flat bandgap, 2) a graded bandgap with an a-Si buffer layer, and 3) a double graded bandgap with a-Si buffer layers, as is shown in Figure 3-1, were used to study the effect of bandgap grading and to optimize the a-SiGe deposition conditions.

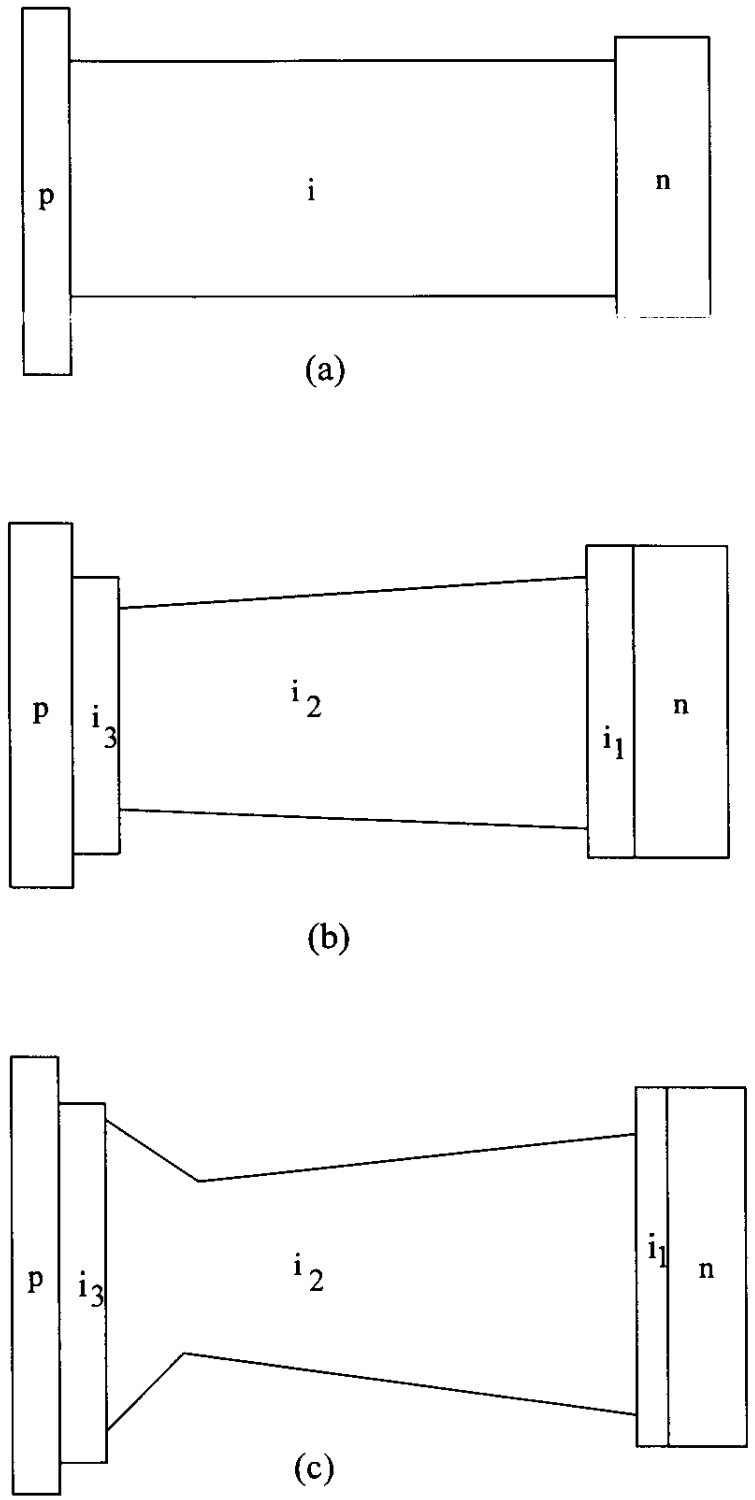

Figure 3-1 Bandgap grading profiles investigated for a-SiGe narrow bandgap solar cells.

For the flat bandgap a-SiGe solar cells, three devices with i-layers having different Ge concentrations were fabricated on both bare SS and SS/Ag/ZnO substrates. Table 3-3 shows the i-layer deposition conditions and solar cell performance for these devices. As expected, when the Ge concentration increases, the solar cell J_{sc} increases, while V_{oc} and FF decrease at the same time. When the GeH_4 to Si_2H_6 ratio is about 50:50 (sample L2101), the FF drops down to around 0.55. However, without enough Ge in the i-layer, the J_{sc} is only around 17 mA/cm^2 (see sample L2103). Therefore, none of the three devices would be a good candidate as the bottom cell of a triple-junction solar cell.

Table 3-3 Device performances of three a-SiGe solar cells with i-layers having different Ge contents (flat bandgap) in the i-layer deposited on SS and BR substrates.

Run #	i-layer gas $GeH_4/Si_2H_6/H_2$	Substrate	V_{oc} (V)	J_{sc} (mA/cm^2)	FF	R_s (Ωcm^2)	Eff (%)
L2101	1.5/1.5/54.0 (50:50)	SS	0.574	14.48	0.547	9.4	4.55
		BR	0.552	19.13	0.553	5.5	5.83
L2103	0.82/1.0/33.1 (45:55)	SS	0.674	13.68	0.597	7.3	5.51
		BR	0.667	17.11	0.574	5.9	6.55
L2106	0.68/1.0/30.6 (40:60)	SS	0.708	12.16	0.640	6.1	5.51
		BR	0.689	15.84	0.606	5.5	6.62

We then fabricated three single-junction a-SiGe devices with different degrees of bandgap grading (see Figure 3-1b). During the a-SiGe i-layer deposition, the Si_2H_6 flow was fixed, while the GeH_4 flow was increased linearly. The highest Ge content, hence the smallest bandgap, is near the p-i interface. The graded bandgap results in a majority of the carriers being generated near the p-layer so that the average distance that holes travel before collection is less. In addition, it generates an internal field which helps holes to drift towards the p-layer. Approximately 200Å thick a-Si buffer layers were deposited on both sides of this a-SiGe layer to ensure good interfaces. Table 3-4 shows the device performance of these a-SiGe solar cells measured under AM1.5 light and Table 3-5 shows the device performance of these a-SiGe solar cells measured under AM1.5 light with a 610 nm cut-on filter, i.e., a red filter to simulate the absorption of the top and middle component cells in a triple-junction solar cell. Among the three devices, sample L2230 shows the highest P_{max}. The one sun P_{max} is 8.2 mW/cm^2 and the P_{max} after 610 nm red filter is 3.66 mW/cm^2. Figure 3-2 shows the J-V curve of this single-junction a-SiGe solar cell measured under a xenon solar simulator with a 610 nm red filter.

Table 3-4 Device performance of a-SiGe solar cells with different bandgap grading in the a-SiGe i-layer, measured under AM 1.5 light.

Run #	Si_2H_6/GeH_4 (sccm)	i-layer thickness (Å)	V_{oc} (V)	J_{sc} (mA/cm^2)	FF	R_s (Ωcm^2)	P_{max} (mW/cm^2)
L2230	1.0/0.68-1.00	1850	0.699	20.40	0.599	5.7	8.17
L2156	1.0/0.54-1.22	1960	0.612	19.01	0.531	9.4	6.18
L2187	1.5/1.20-2.00	1690	0.620	19.86	0.525	8.5	6.47

Table 3-5 Device performance of a-SiGe solar cells with different bandgap grading in the a-SiGe i-layer, measured under AM 1.5 light with a 610 nm cut-on filter.

Run #	Si_2H_6/GeH_4 (sccm)	i-layer thickness (Å)	V_{oc} (V)	J_{sc} (mA/cm^2)	FF	R_s (Ωcm^2)	P_{max} (mW/cm^2)
L2230	1.0/0.68-1.00	1850	0.639	9.14	0.627	9.6	3.66
L2156	1.0/0.54-1.22	1960	0.569	8.18	0.548	16.4	2.55
L2187	1.5/1.20-2.00	1690	0.594	8.55	0.560	14.9	2.84

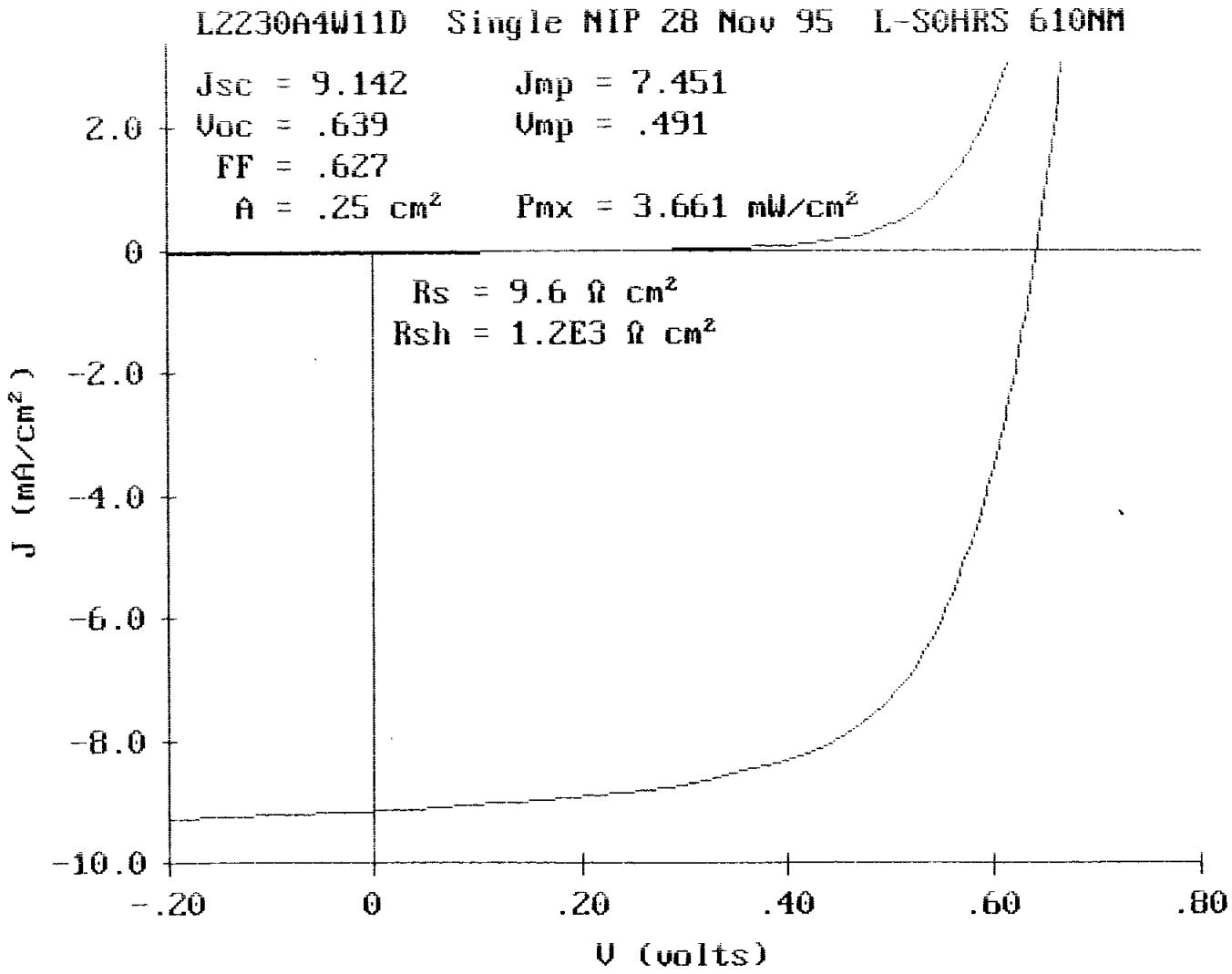

Figure 3-2 J-V curve of a single-junction a-SiGe narrow bandgap solar cell measured under AM1.5 light with a 610 nm red filter.

We have also fabricated a-SiGe devices with i-layers deposited at different substrate temperatures. Table 3-6 shows two devices having a-SiGe i-layers deposited at 250 and 300 ^{o}C. The device deposited at higher temperature has a higher fill factor indicating a superior quality a-SiGe material as has been suggested previously.[20] This higher substrate temperature enhances the surface mobility of Ge atoms during growth, and consequently improves the material's quality.

Table 3-6 Device performance of a-SiGe solar cells with i-layer deposited at different temperatures.

Run #	T_s (°C)	i-layer thickness (Å)	V_{oc} (V)	J_{sc} (mA/cm^2)	FF	R_s (Ωcm^2)	P_{max} (mW/cm^2)
L2257	250	2100	0.688	20.39	0.554	8.7	7.78
L2230	300	1850	0.669	20.40	0.599	5.7	8.17

In an effort to further improve the a-SiGe bottom cell, we deposited a-SiGe cells with a double graded profile as shown in Figure 3-1(c). Figure 3-3 shows the J-V curve for such a device (L2241) measured under the simulator with a 610 nm filter. The results are similar to those for L2230. Therefore, both profiles (b) and (c) in Figure 3-1 can be used to fabricate narrow bandgap a-SiGe bottom cells.

We have light soaked a representative device from each of the three group of samples having different bandgap profiles. Table 3-7 lists the light soaking performance measured with a 610 nm filter before and after light soaking. After 300 hours of one-sun light soaking, the a-SiGe devices with optimized bandgap profiles and deposition conditions have a degraded P_{max} of around 2.9 mW/cm^2, as is shown in Figure 3-4.

Table 3-7 P_{max} measured under AM1.5 light with 610 nm filter for a-SiGe solar cells with different bandgap grading profiles, after different light soaking times.

Light Soaking Time (hr)	Pmax (mW/cm^2)		
	L2106 (a)	L2230 (b)	L2241 (c)
0	2.56	3.66	3.63
300	2.13	2.89	2.94

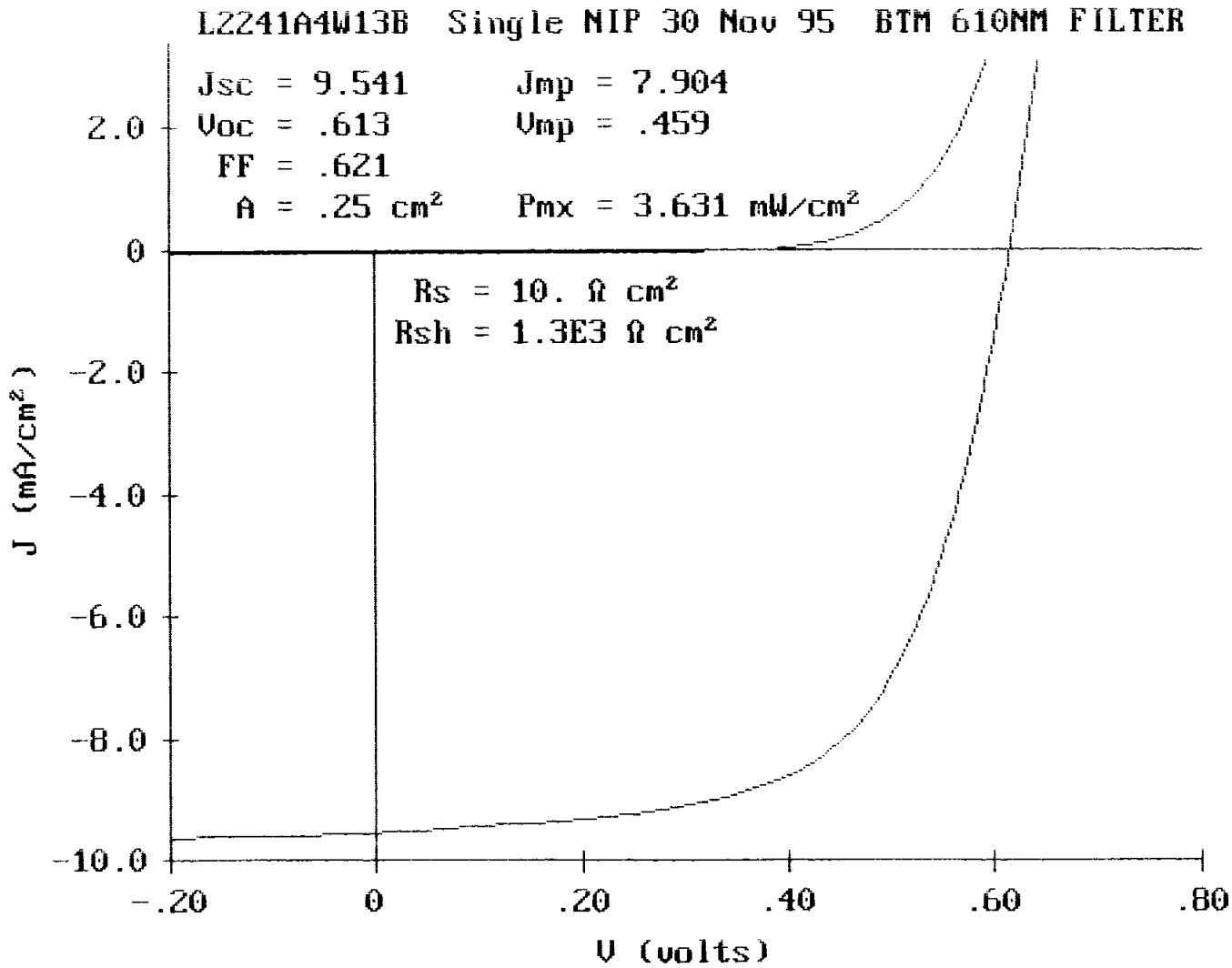

Figure 3-3 J-V curve of an a-SiGe solar cell with double graded bandgap profile, measured under AM1.5 light with a 610 nm red filter.

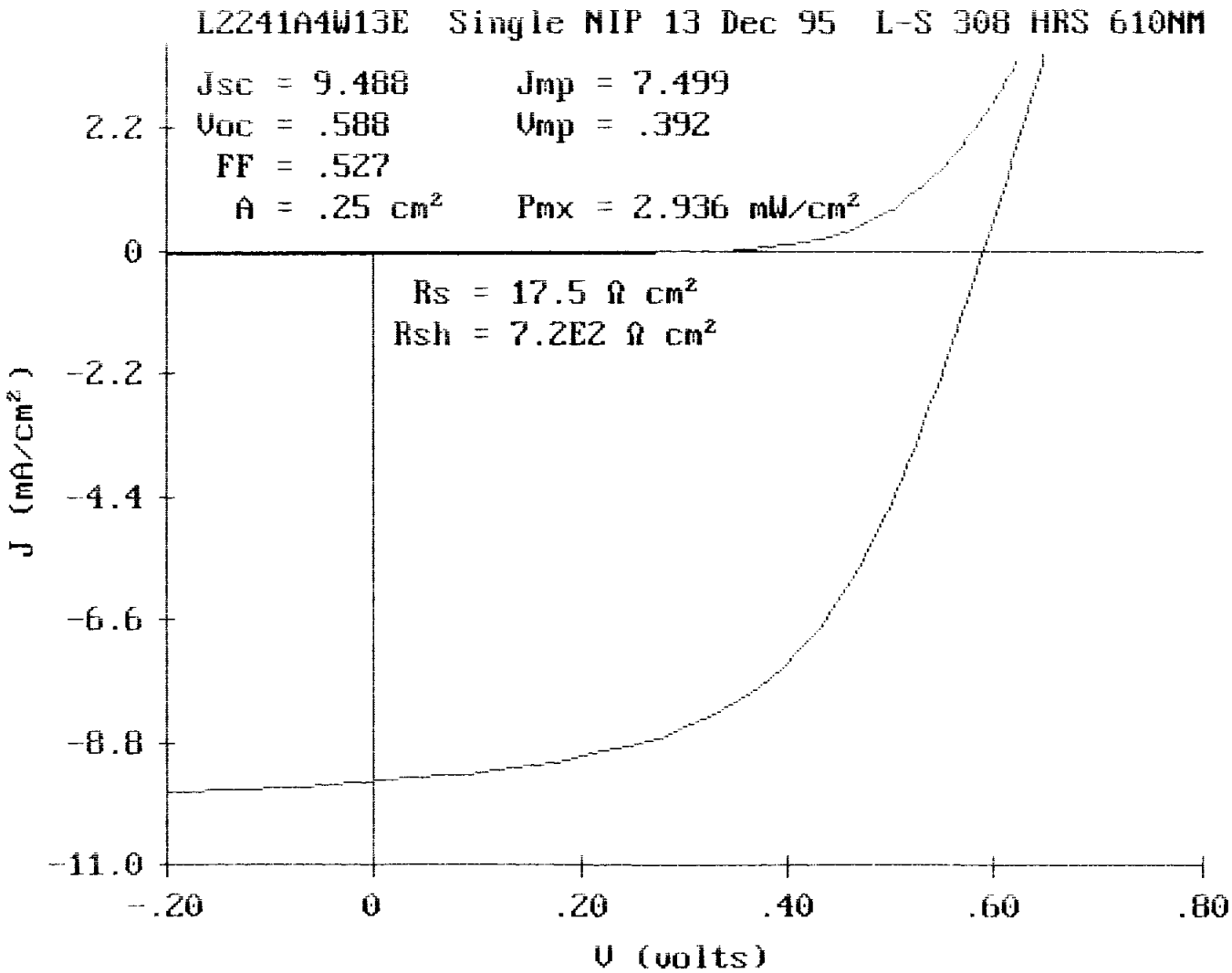

Figure 3-4 J-V curve of an a-SiGe solar cell after 300 hours of one sun light soaking at 50 °C, measured under AM1.5 light with a 610 nm red filter.

3.4 Optimization of a-SiGe Middle Cell

When a-Si is used as the middle cell i-layer of a triple-junction solar cell, the i-layer needs to be at least 4500Å thick to achieve component cell current matching. Such a cell shows large light soaking degradation.[21] In order to improve the triple-junction solar cell light stability, a middle cell with a relatively thinner a-SiGe i-layer was optimized in the LL2 deposition system.

Table 3-8 shows the deposition temperature and GeH_4 and Si_2H_6 gas flows for three a-SiGe middle component cells deposited on SS. A J_{sc} of 14 mA/cm^2 is needed for such a device on SS substrate to achieve current matching. Among this group of samples, L2184 shows the highest P_{max} and is therefore used as the standard middle cell i-layer. Figure 3-5 is an initial J-V curve of an a-SiGe middle component cell.

Table 3-8 Deposition conditions for and device performance of a-SiGe middle component cells deposited on SS.

Run #	T_s (°C)	Si_2H_6/GeH_4	i-layer thickness (Å)	V_{oc} (V)	J_{sc} (mW/cm^2)	FF	R_s (Ωcm^2)	P_{max} (mW/cm^2)
L2163	250	1.5/0.270	3000	0.889	13.58	0.596	12.3	7.20
L2165	250	1.5/0.375	2700	0.827	13.63	0.619	9.0	6.98
L2184	300	1.5/0.375	3000	0.849	14.82	0.581	9.4	7.31

3.5 Summary

We have studied and evaluated the a-SiGe material deposited at Harvard on the cathode plate using n-i-p solar cells. These solar cells did not show better performance than cells with a-SiGe i-layers having similar bandgap deposited at ECD on an anode.

We have optimized the deposition of a-SiGe solar cells with different bandgap grading profiles and with different deposition conditions. Both narrow and middle bandgap a-SiGe cells have been improved in the LL2 system. The optimized a-SiGe narrow bandgap solar cells show a stabilized P_{max} of 2.94 mW/cm^2, measured with a 610 nm red filter, after 300 hours of one-sun light soaking at 50 ^{o}C.

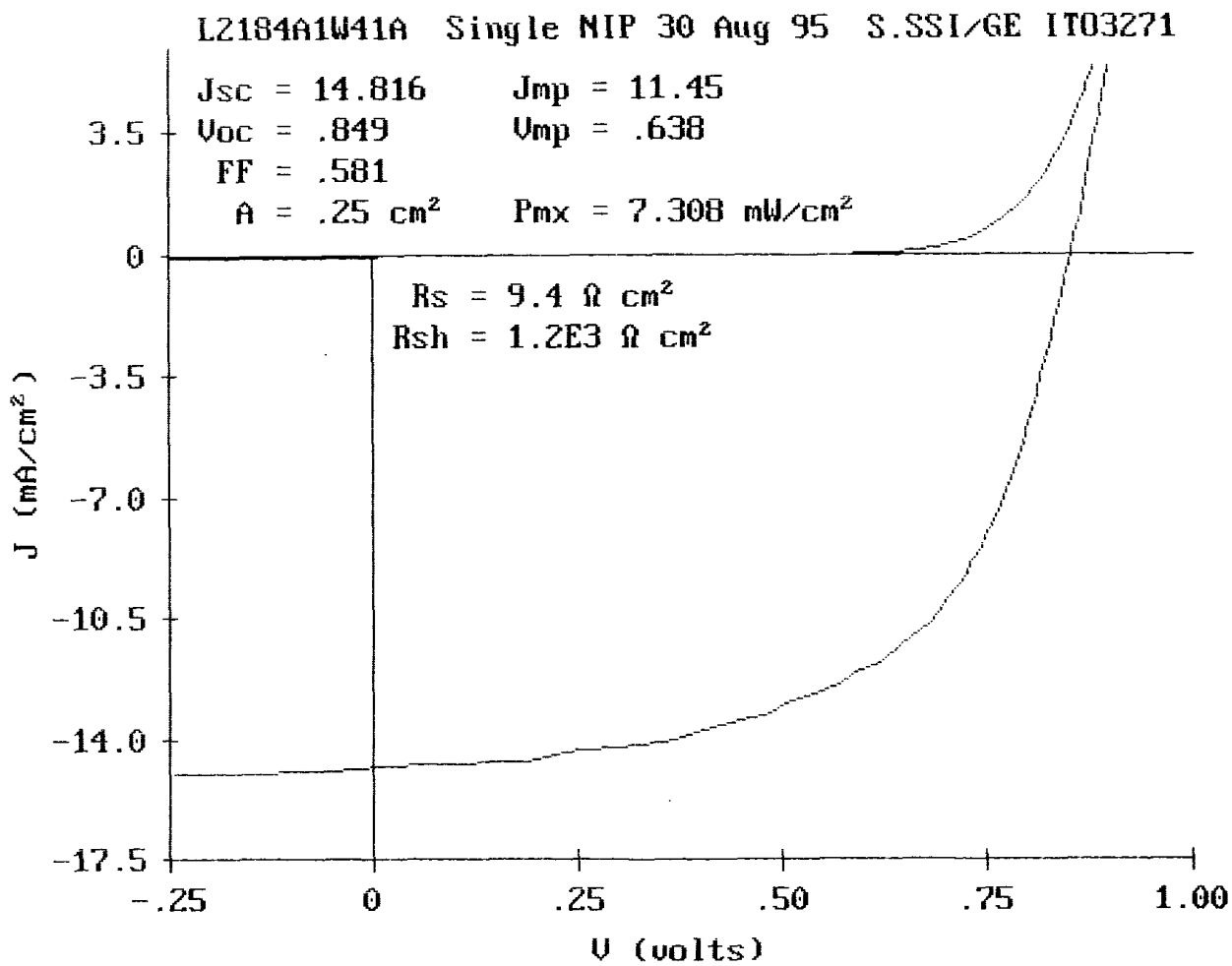

Figure 3-5 J-V curve of an a-SiGe cell being used as the middle component cell of a triple-junction solar cell.

Section 4
Wide Bandgap Solar Cells

4.1 Introduction

The open circuit voltage (V_{oc}) of an a-Si single-junction solar cell with a μc-Si p-layer deposited in our laboratory is normally in the range of 0.93-0.96 V. In an effort to optimize the top component cell for a triple-junction solar cell, we realized that the major limitation to the V_{oc} is not the p-layer but the intrinsic a-Si layer. Therefore, we began a study to improve the V_{oc} of the single-junction a-Si top cell by improving the a-Si intrinsic layer deposition conditions.

Wide bandgap alloys such as a-SiC had been extensively studied for use as the intrinsic layer of the top cell of an a-Si alloy triple-junction solar cell in many laboratories.[22] However, when a-Si is alloyed with carbon, oxygen or nitrogen, the density of defect states increases rapidly making them undesirable for use as the intrinsic absorber layer for a-Si based solar cells.

Thus, it may be more beneficial to widen the bandgap by increasing the hydrogen content in the a-Si cells.[23,24] It has been shown that this can be done by lowering the substrate temperature. In addition, to maintain a reasonable film quality, the amount of hydrogen dilution usually has to be raised as the temperature is lowered. Other laboratories have used these conditions to prepare high V_{oc} a-Si solar cells.[25,26] It has also been found that the solar cells fabricated with this intrinsic layer are more stable after prolonged light soaking. We have systematically investigated the growth of a-Si at low temperature with strong hydrogen dilution, and have incorporated this material into an n-i-p top cell to improve the solar cell open circuit voltage.

4.2 Experimental Details

We have primarily used an a-Si n-i-p solar cell device structure for the optimization of the a-Si intrinsic layer deposition. The device structure principally used for this study is SS/a-Si n^+/a-Si intrinsic/μc-Si p^+/ITO. A bare SS substrate without back-reflector was, for the most part, used in this work, since the top a-Si cell is grown on the middle cell in a triple-cell structure and does not benefit significantly from the optical enhancement with use of the back-reflector. The a-Si intrinsic layers were deposited at different substrate temperatures ranging from 150 to 250 °C with a wide range of hydrogen dilution, a deposition pressure of 1 Torr, and a power density of 20 mW/cm^2. The p-layer is boron-doped microcrystalline silicon. When such an μc-Si p^+ is used for the p-layer, the V_{oc} of the solar cell is limited mainly by the properties of the intrinsic layer. As is usually done, the ITO layer was deposited using reactive evaporation of an indium-tin alloy in oxygen.

4.3 Results and Discussions

In Table 4-1, we list the solar cell performance for single-junction a-Si devices made with heavily H_2 diluted plasmas at different substrate temperatures. All of these devices were deposited on bare SS with no back reflector. The progressive increase in V_{oc} with decreasing substrate

temperature is apparent. At 150 °C, a high V_{oc} of 1.04 V is achieved. After further improving the deposition process, we have achieved cells with initial V_{oc} of 1.053 V. The J-V curve for such a device is shown in Figure 4-1. This 1.053 V value is among the highest V_{oc} reported for any single-junction a-Si solar cell. The FF for the 1.05 V device is high, indicative of a high quality a-Si i-layer material. As the substrate temperature is lowered beyond 150 °C, the cell properties dramatically deteriorate, possibly due to polysilicon chain or microcrystalline formation. We should note that in terms of FF the material deposited at the higher substrate temperatures was not made under optimum conditions. Less hydrogen dilution and different RF powers are typically used when T_s ~ 230-250 °C. Also to obtain the high V_{oc} cells with the optimum cell properties, the p-layer preparation conditions were correspondingly adjusted.

Table 4-1 Cell performance for devices made at different substrate temperatures with high hydrogen dilution.

Cell Number	Substrate Temperature (^oC)	V_{oc} (V)	J_{sc} (mA/cm^2)	FF	i-layer thickness (Å)
LL712	250	0.951	12.1	0.585	3200
LL723	230	0.959	11.3	0.608	3200
LL722	210	0.980	11.7	0.615	3100
LL731	210	0.986	12.0	0.626	3300
LL732	175	1.026	10.0	0.670	2850
LL746	150	1.040	9.4	0.652	2640
LL853	125	0.398	6.7	0.619	-

To study the properties of this new i-layer material, single layer films were deposited for materials characterization. However in most cases, the films peeled off the substrates even for the thinnest films, suggesting high compressive stress in these films.[27] We were able to get some films to stick to 7059 glass for optical absorption measurements. From a Tauc plot, we obtained, somewhat surprisingly, a bandgap of 1.80 eV, a typical value for a-Si. Although the extrapolation in the Tauc plot gives 1.80 V, the absorption coefficient of this high V_{oc} material is indeed lower than that for the conventional a-Si. It has a rather high E_{04} (photo energy at which $\alpha = 10^4$ cm^{-1}) value for "device quality" a-Si.

When the a-Si deposition temperature is reduced, more hydrogen dilution is needed to achieve high quality material. However, when the hydrogen dilution increases beyond a certain limit, V_{oc} as well as other parameters for the solar cell drastically decrease, due to microcrystalline formation. Figure 4-2 shows the J-V curve for a device with the i-layer deposited at 230 °C using the high hydrogen dilution level which is optimized for 150°C wide bandgap a-Si deposition. One can see that V_{oc} has dropped to 0.86 V. The FF is slightly higher than for device LL723 in Table 4-1 because its i-layer is thinner.

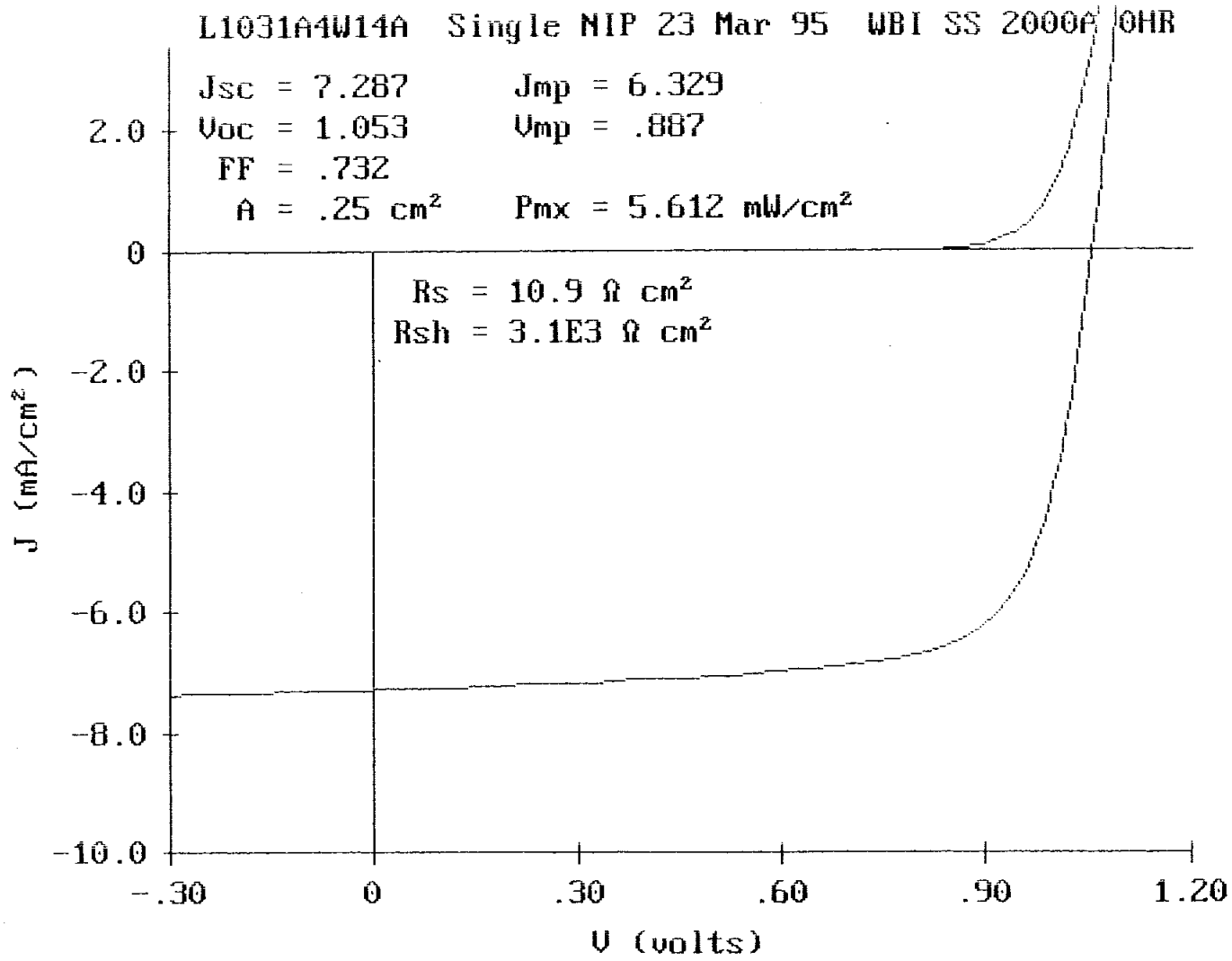

Figure 4-1 J-V curve of wide bandgap a-Si single cell showing 1.053 V initial V_{oc}.

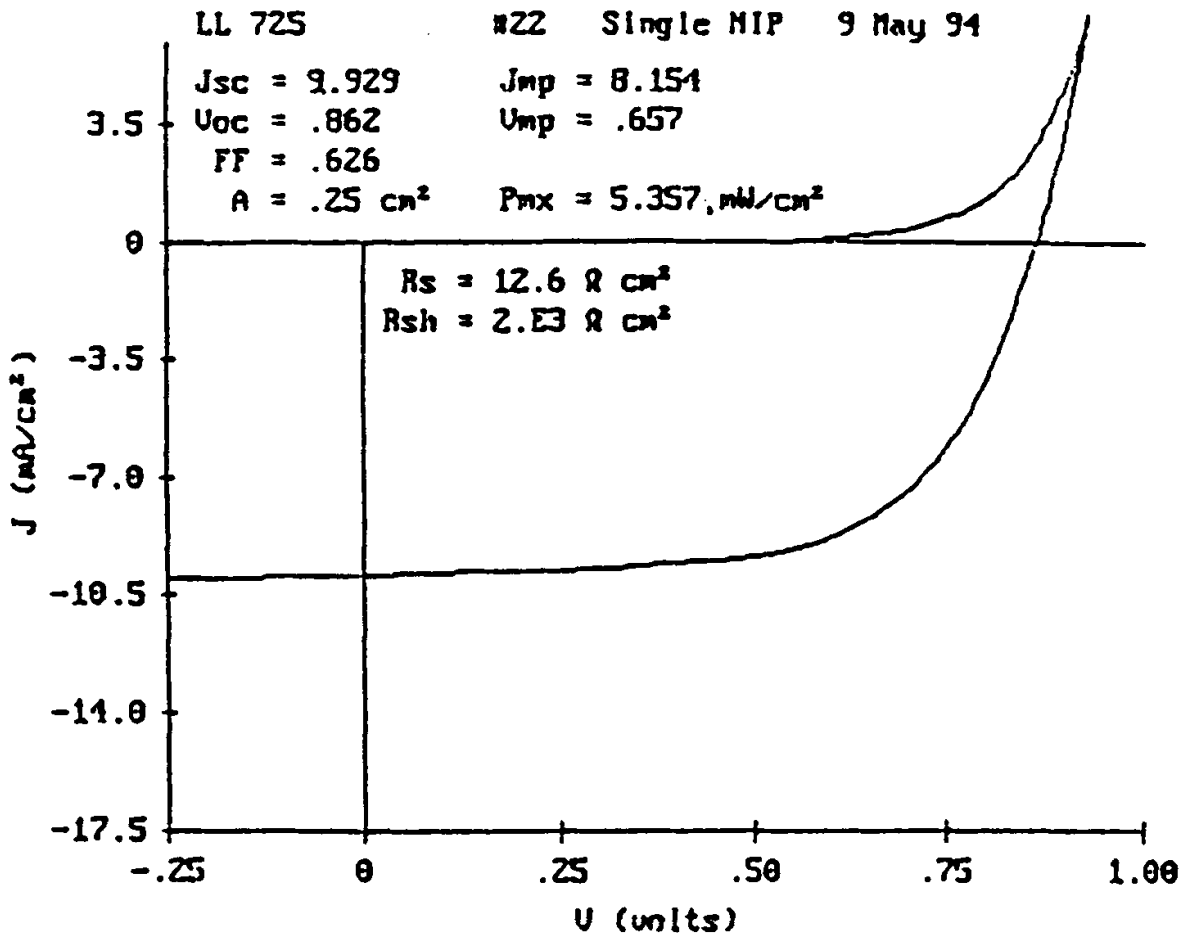

Figure 4-2 J-V curve of a-Si device with i-layer deposited at relatively high temperature (230 °C) with too strong a dilution.

Table 4-2 summarizes the cell performance for these high V_{oc} devices as a function of i-layer thickness. We remind the reader that these cells were prepared without back-reflectors. The expected trends of increasing J_{sc} as well as the decrease in FF with increasing i-layer thickness are obvious. We found that beyond an i-layer thickness of 2000Å, the V_{oc} decreases slightly to a value of 1.02 V at a thickness of 4000Å.

Also included in the table is the trend in the properties for the devices with increased light soaking. After 2500 hrs of light soaking, these cells degrade by 13-20% with the thinner samples degrading less as expected. Figure 4-3 shows the J-V curve for a wide bandgap a-Si single cell demonstrating a stable V_{oc}=1.014 V after 2500 hours of one sun light soaking at 50 ^{o}C. This is the highest stable V_{oc} reported for single-junction a-Si solar cells. As we see from the table, after this amount of light soaking, all of the cells with i-layer thicknesses less than 3000Å have stable V_{oc} greater than or equal to 1.00V after 2500 hours of light soaking.

Table 4-2 Properties for high V_{oc} cells made with different i-layer thicknesses during the initial state and after light soaking for different time periods.

Sample	i-layer thickness (Å)	Light soaking Time (hrs)	J_{sc} (mA/cm^2)	V_{oc} (V)	FF	P_{max} (mW/cm^2)
L1036	1500	0	6.88	1.04	0.742	5.26
		72	6.76	1.01	0.696	4.74
		2500	6.47	1.01	0.696	4.57
L1031	2000	0	7.29	1.05	0.732	5.60
		72	7.13	1.01	0.686	4.96
		2500	6.95	1.01	0.646	4.53
L1041	2400	0	8.17	1.03	0.707	5.96
		72	7.68	0.998	0.634	4.86
L1014	2800	0	8.15	1.03	0.691	5.78
		72	8.17	1.01	0.645	5.27
L1032	4000	0	11.59	1.02	0.592	6.96
		72	10.88	0.997	0.551	5.86
		2500	10.76	0.977	0.556	5.84

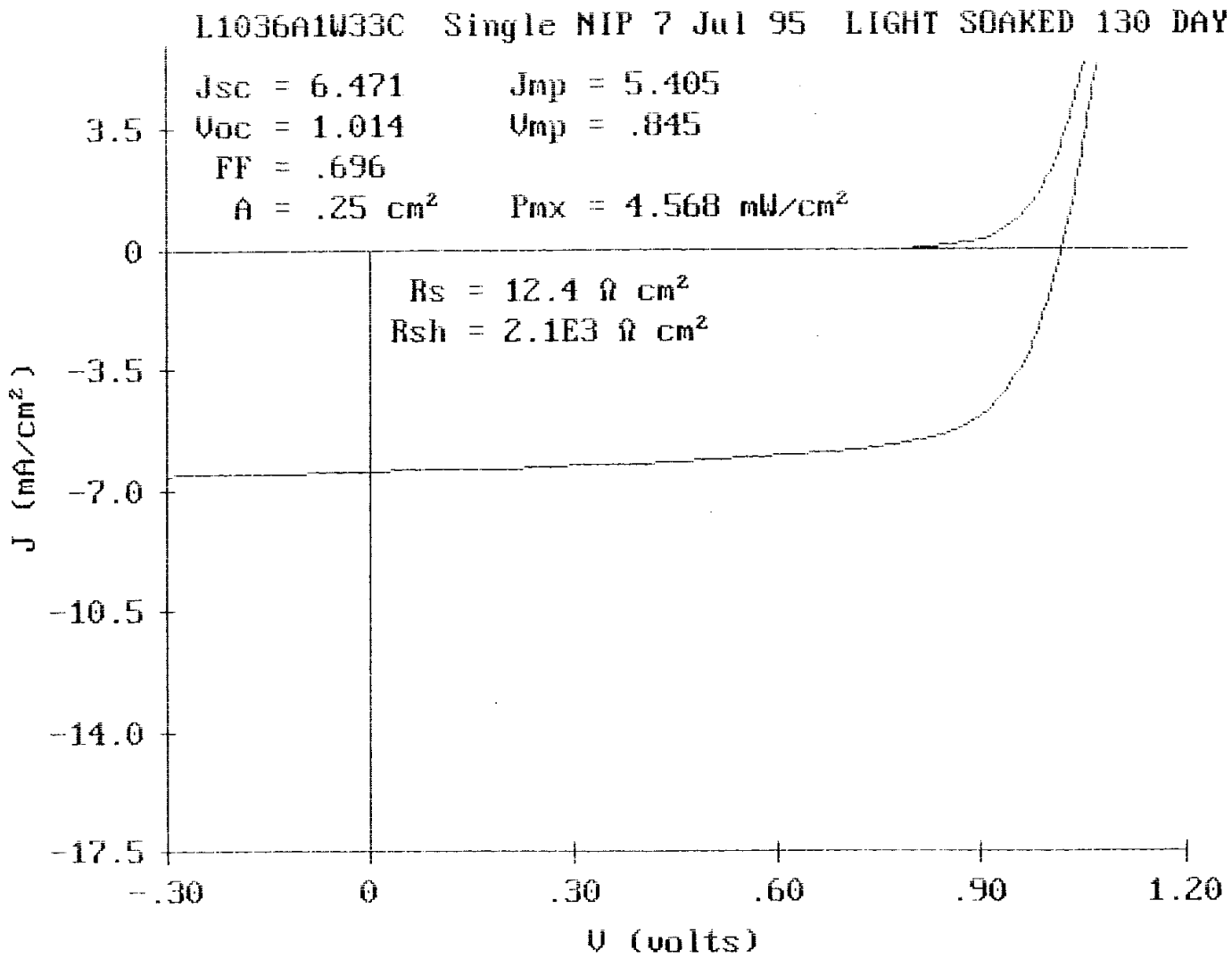

Figure 4-3(a) J-V curve of a wide bandgap a-Si single cell after 2500 hours of one sun 50 °C light soaking, showing 1.014 V stabilized V_{oc} .

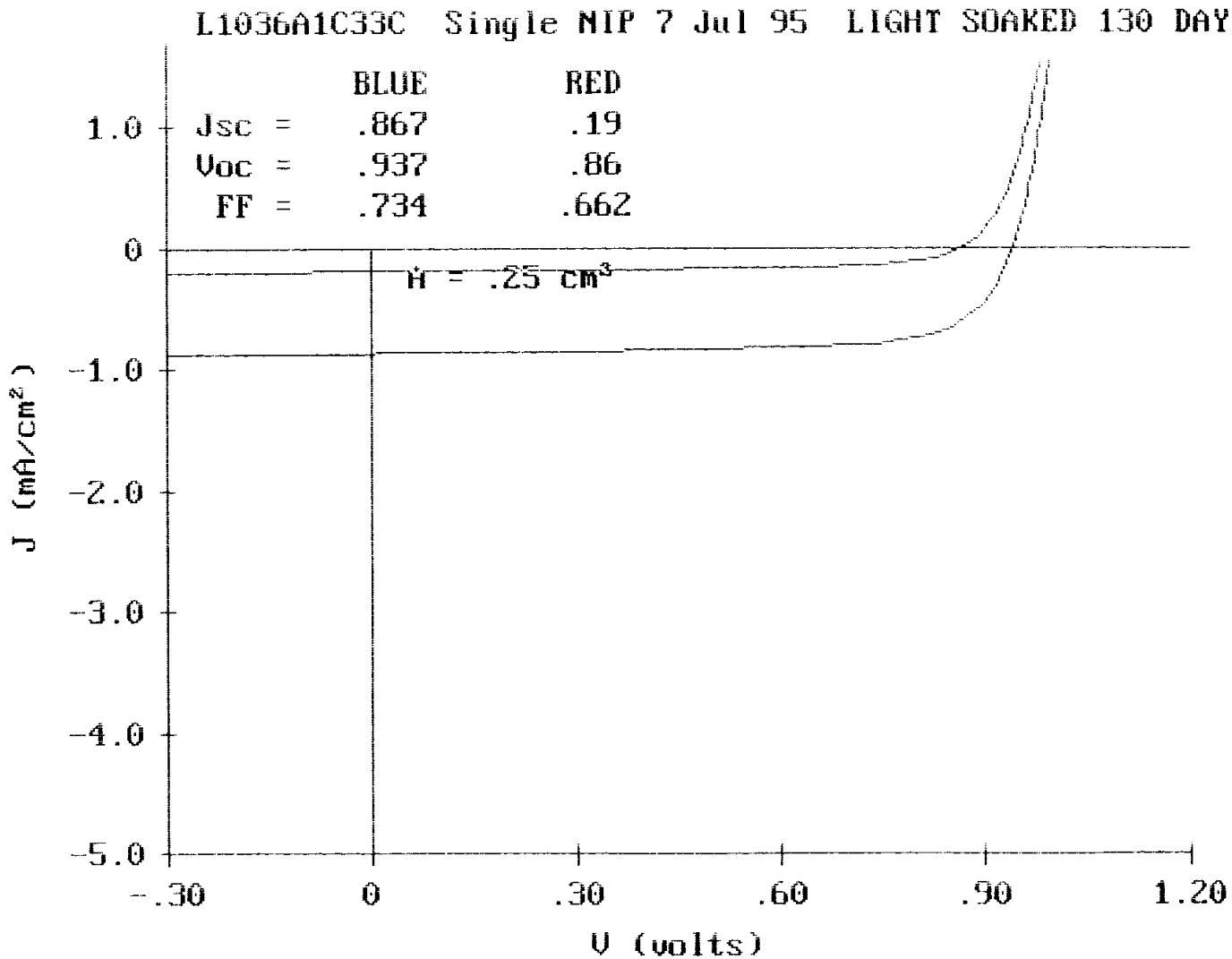

Figure 4-3(b) J-V curve of a wide bandgap a-Si single cell after 2500 hours of one sun 50 °C light soaking, measured under weak blue and red lights.

When these high V_{oc} devices are grown on Ag/ZnO back reflectors, the V_{oc} values are lower. Table 4-3 displays initial cell data for devices prepared on bare SS and SS/Ag/ZnO substrates in the same n-i-p deposition. For the cells with i-layer thicknesses below 3000Å, V_{oc} is generally 30 mV smaller for the devices with back reflector. The thicker devices display smaller differences. These differences have been minimized through increased p-layer thicknesses. However since these high V_{oc} n-i-p devices will be used as the top cell of a triple, they will be deposited on top of the middle and bottom cells so this drop in V_{oc} will be less critical in the multijunction devices.

Table 4-3 Data for high V_{oc} devices prepared on bare SS and SS/Ag/ZnO substrates in the same n-i-p deposition.

Sample	i-layer thickness (Å)	Substrate	J_{sc} (mA/cm^2)	V_{oc} (V)	FF	P_{max} (mW/cm^2)
L1036	1500	Bare SS	6.88	1.04	0.742	5.26
		Ag/ZnO	9.90	1.01	0.715	7.17
L1031	2000	Bare SS	7.29	1.05	0.732	5.60
		Ag/ZnO	10.41	1.01	0.705	7.40
L1032	4000	Bare SS	11.59	1.02	0.592	6.96
		Ag/ZnO	14.78	1.01	0.610	9.14

To demonstrate the improvement in V_{oc} in a multijunction device, we deposited the best high V_{oc} n-i-p device on a standard a-Si cell to form an a-Si/a-Si tandem structure. The complete device structure is: SS/Ag/ZnO/standard a-Si n-i-p/high-V_{oc}-a-Si-n-i-p/TCO/Ag grid. Figure 4-4 displays the J-V curve for such a tandem device. As a comparison, we have also fabricated a tandem device with both intrinsic layers deposited using the standard conditions, i.e. 250 ^{o}C and regular hydrogen dilutions. The J-V curve for such a reference device is shown in Figure 4-5. In the tandem device, the V_{oc} has increased from 1.77 V to 1.84 V with the use of the high V_{oc} top cell. The 68 mV gain is approximately the same as the gain noted in the single devices (from 0.96 to 1.04-1.05 V). The slightly lower FF in the first tandem-junction cell is due to a different mismatch in currents. We have incorporated the high V_{oc} cells into the triple-junction design and report the results in a later section of this report.

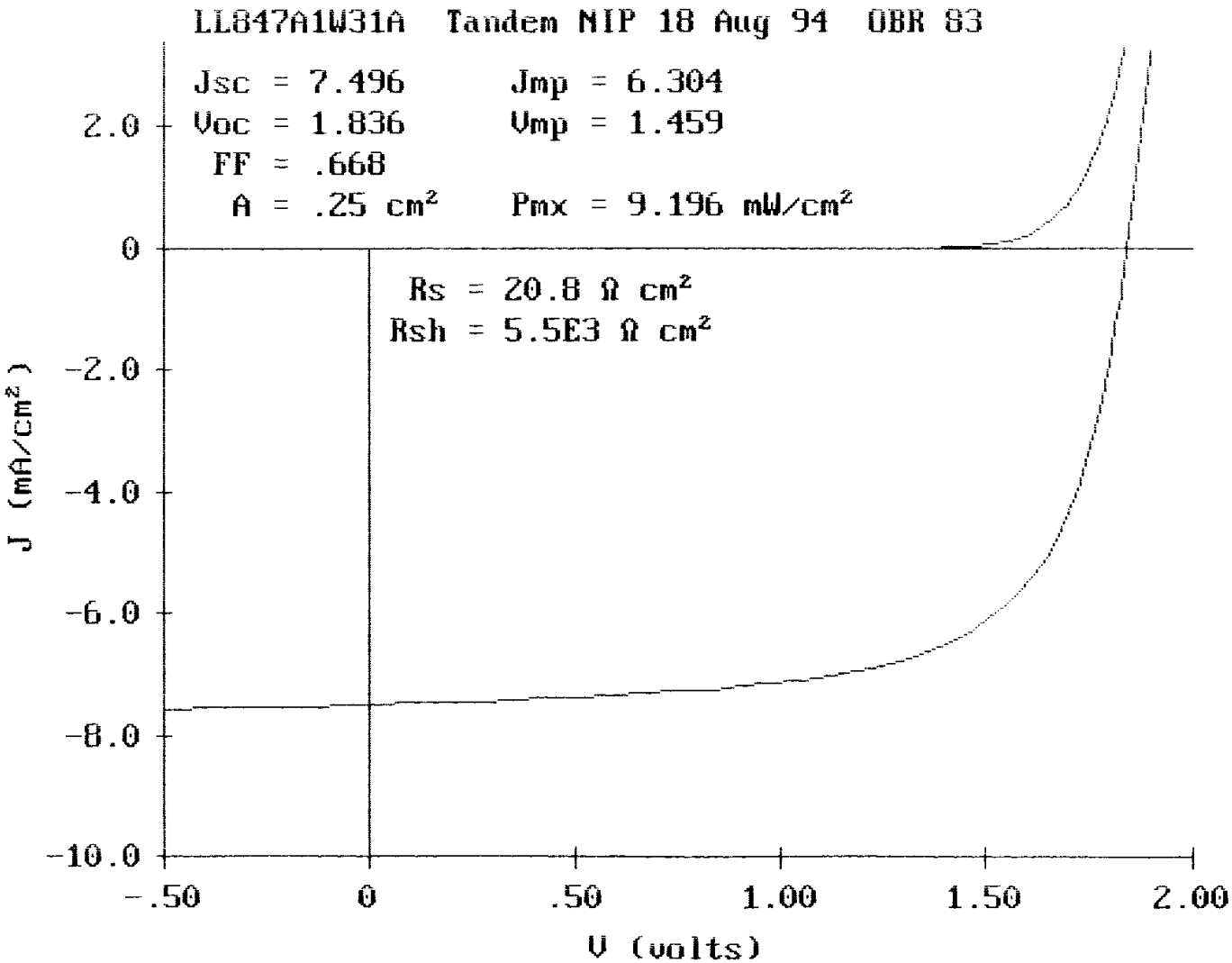

Figure 4-4 J-V curve of a tandem-junction solar cell with wide bandgap a-Si as the top cell intrinsic layer.

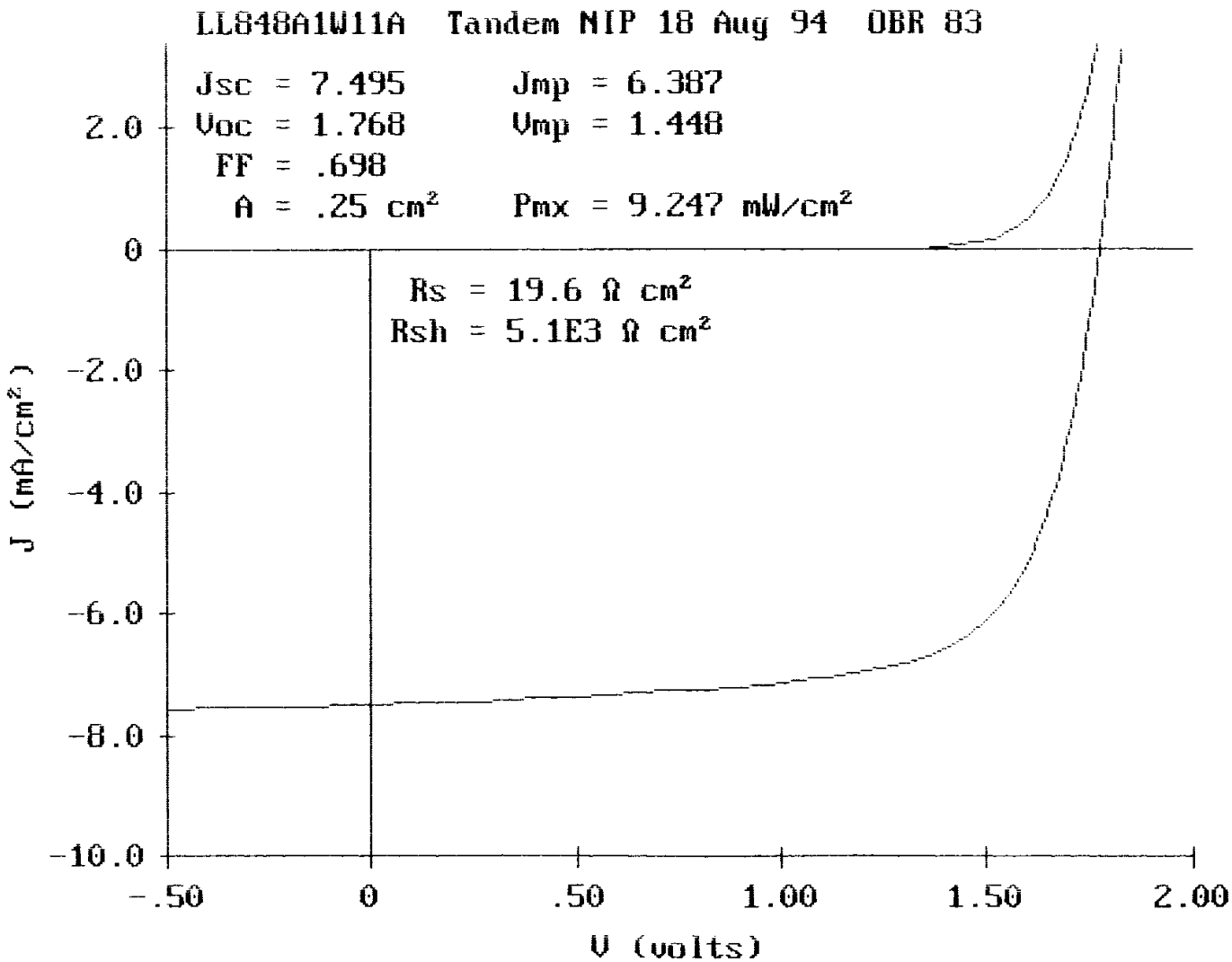

Figure 4-5 J-V curve of a tandem solar cell with a regular top i-layer for reference.

4.5 Structural Study of High V_{oc} i-layer Materials

We have prepared films for Infrared Absorption Spectroscopy (IR), Small-Angle X-ray Scattering (SAXS) and Raman Spectroscopy Analysis to study the structure of these films. The IR and Raman analysis was done in-house while the SAXS measurements were done at the Colorado School of Mines by Don Williamson.[28] Figure 4-6 displays IR data for one of these low T_s, high dilution films. One can see the presence of small peaks between 840 and 890 cm^{-1} associated with scissors and wag modes of $(SiH_2)_n$ in the figure. The presence of a small amount of polyhydride modes is consistent with a film prepared at rather low substrate temperatures and the recent findings of the group at United Solar for their films prepared under high hydrogen dilution conditions. Because the film peeled off the substrate during film thickness measurements, we were not able to obtain an accurate thickness measurement and thus a bonded hydrogen content was not obtained. As a general note, these films peeled off glass and c-Si substrates easily upon exposure to the atmosphere when the film thickness was greater than 0.3 μm. This is consistent with film with very high compressive stresses, which is usually associated with a-Si material with a high density and few voids.

SAXS data for a 1 μm thick film is shown in Figure 4-7. Very little scattering is seen suggesting that there are few voids in the material. As a comparison, the dashed line represents the amount of scattering expected from a film with a void fraction of 0.1%. The amount of scattering from our sample is clearly less implying that the void fraction is even less than 0.1%. As might be expected from a sample with very weak SAXS, no change in the data was observed when the sample was measured in the tilted configuration suggesting that any voids that might be present are not of a columnar nature. Comparing the IR and SAXS data, it seems that the hydrogen bonding which leads to the polyhydride IR signals are not related to hydrogen near void surfaces.

4.5 Summary

An initial V_{oc} of 1.053 V has been achieved for an a-Si solar cell using an a-Si intrinsic layer deposited at relatively low temperature with high hydrogen dilution. After 2500 hours of light soaking under one sun at 50 ^{o}C, the V_{oc} stabilized to a value of 1.014 V. Compared to the alternative a-SiC high bandgap intrinsic layer, this a-Si material absorbs light more efficiently and the material quality is higher. We thus conclude that the high V_{oc} a-Si material is a better choice than high bandgap a-SiC alloys as the top cell intrinsic layer of a triple-junction a-Si alloy solar cell rather.

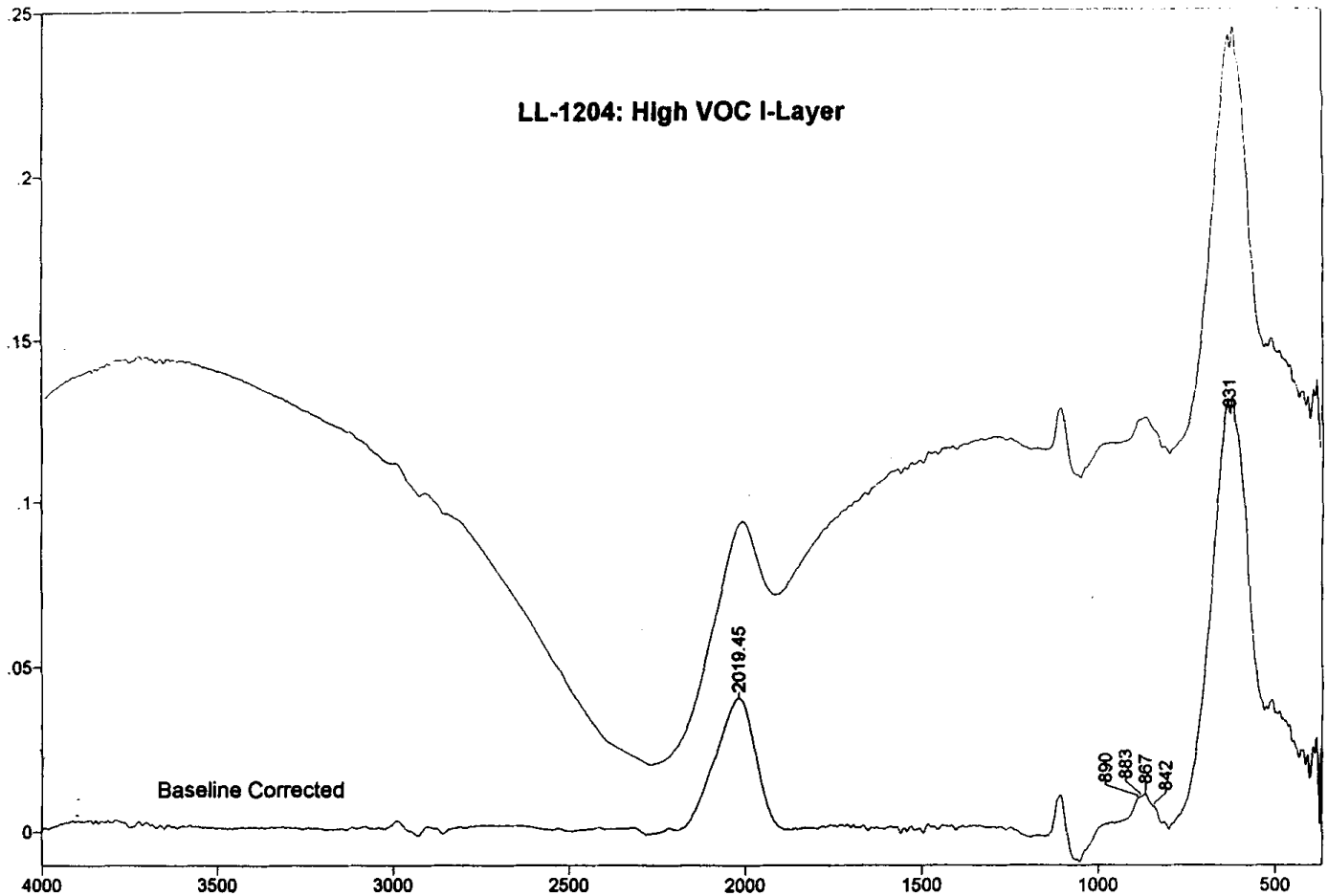

Absorbance / Wavenumber (cm-1)

Number of Scans= 32 Apodization= Strong

File # 1 : LL-1204F

3/1/96 10:03 AM Res=4 cm-1

a-Si:H High VOC on c-Si, Baseline Flattened

Figure 4–6 IR spectrum of an a-Si film deposited at low temperature and with high hydrogen dilution.

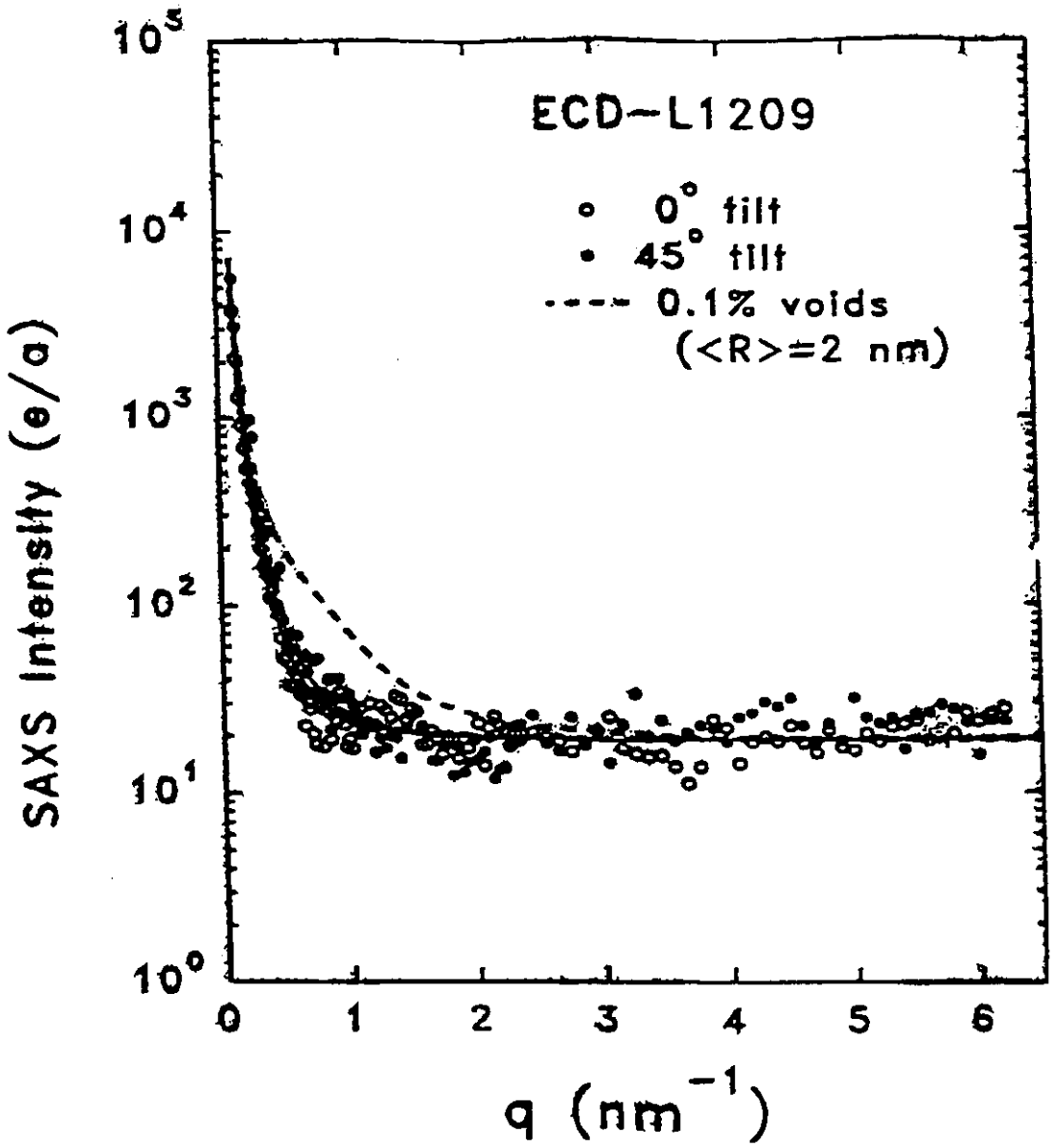

Figure 4-7 Small Angle X-Ray Scattering spectrum of an a-Si film deposited at low temperature and with high hydrogen dilution.

Section 5
Microcrystalline Silicon Alloy As Novel p-type Materials

5.1 Introduction

With the boron doped microcrystalline Si as the p-layers, we routinely obtain V_{oc} of 0.93-0.96 V for single-junctions a-Si devices made using our solar cell deposition systems. The microcrystalline layer, with its wider direct bandgap, also leads to higher currents as compared with devices with amorphous p-layers.

The μc-Si p-layer still has some volume fraction of amorphous phase, which has smaller bandgap and hence less transmission than the microcrystalline phase. In order to achieve higher current and higher V_{oc} for a-Si devices, we explored microcrystalline silicon oxide (μc-SiO) and microcrystalline silicon carbide (μc-SiC) p-layers by alloying the amorphous silicon phase of the p-layer with oxygen or carbon to widen its effective bandgap.

A similar approach of widening the bandgap and improving the current by alloying Si with O has been studied by researchers at Fuji Electric for their amorphous p-layers.[29,30] With the a-SiO_x p-layer, they have obtained 18.8 mA/cm^2 short circuit current densities in a single-junction a-Si p-i-n solar cell with 4000Å thick a-Si i-layers. Although Fuji's a-SiO_x layer has a 2.15 eV bandgap, the V_{oc} for their p-i-n devices is only 900 mV. This is because the amorphous oxide material has a broader valence band tail and a fermi level which is farther from the band edge than that for μc-Si. Devices made with our μc-SiO and μc-SiC p^+ layers were expected to have significantly higher V_{oc} and higher J_{sc} than those with a-SiO_x p^+ layers.

Along the same lines, Ma et al.[31] have produced microcrystalline SiC p-layers using ECR microwave plasmas. With this larger bandgap material, they also obtained higher short circuit currents (19.6 mA/cm^2) as compared with cells made with the conventional boron-doped a-Si p-layers. The V_{oc} values for cells with this new p-layer were around 0.94 V, a value we routinely match or exceed with our μc-Si p-layer. Thus if we alloy our p-layer with O or C while maintaining it's microcrystalline state, we should at least see an improvement in J_{sc} while maintaining or improving the V_{oc}. In addition, unlike ECR microwave deposition, the growth technique we explored is easily scaleable to large area PV manufacturing processes.

5.2 Experimental

Both types of alloys were prepared using ECD's Box deposition system. We used SS/n/i produced in ECD's roll-to-roll machine as the substrate for this study. The i-layer were nominally 3000Å thick. These n-i layers lead to 6.2-6.7% devices when standard p-layers were deposited on them using the LL1 system.

CO_2 and CH_4 were used as source gases for μc-SiO and μc-SiC deposition and their flows were systematically varied. SiH_4, BF_3 and H_2 were the other gases used. Total gas flow, chamber pressure, substrate temperature, applied power and substrate bias were also systematically varied.

After p-layer deposition, our standard ITO and Ag grids were deposited onto the p-layers to complete the devices.

5.3 Microcrystalline SiO

Table 5-1 displays the properties for cells made with varying CO_2 flow while all other parameters were nominally fixed. The unoxidized μc-Si p-layers were prepared under similar conditions to those used for the LL1 p-layer except that relatively thicker p-layers were used so that any small change in p-layer thickness with varying CO_2 flow would not alter V_{oc} drastically.

Table 5-1 Properties for cells made with varying amounts of CO_2 flow while all other parameters were nominally fixed.

Sample	Relative CO_2 flow (sccm)	J_{sc} (mA/cm^2)	V_{oc} (V)	FF	P_{max} (mW/cm^2)	R_S (Ωcm^2)
563	0	9.6	0.95	0.66	6.0	10
520	0	9.4	0.95	0.68	6.0	8
538	1.0	9.9	0.96	0.63	6.0	13
547	1.0	9.4	0.95	0.64	5.8	12
540	2.0	10.2	0.96	0.56	5.4	37
544	2.0	9.6	0.95	0.52	4.7	52
541	5.0	No Measure able J-V curves				

As can be seen from the data, the V_{oc} stays constant and the J_{sc} is improved slightly as the CO_2 flow is increased. However, the series resistance increases and the FF decreases at the same time. We believe the deterioration in the cell properties is related to an observed formation of powder in the chamber when CO_2 was incorporated into the gas mixture. By increasing the substrate temperature by 40 ^oC from 140 to 180 ^oC, we were able to almost entirely eliminate the powder formation. And, as can be seen from the data listed in Table 5-2, the FF and R_s values for cells prepared at this higher temperature (180 ^oC) are comparable to those for the cells with unoxidized p-layers made at the lower temperature (samples 520 and 563 in Table 5-1). We have not yet obtained a μc-SiO p-layer that is superior in an n-i-p solar cell than the μc-Si p-layers that are routinely deposited in our laboratory.

Table 5-2 Properties for cells made at different p-layer substrate temperatures while all other parameters were nominally fixed.

Sample	Substrate Temp. (^oC)	Relative CO_2 flow (sccm)	J_{sc} (mA/cm^2)	V_{oc} (V)	FF	P_{max} (mW/cm^2)	R_S (Ωcm^2)
544	140	2.0	9.6	0.95	0.52	4.7	52
550	180	2.0	9.3	0.91	0.67	5.7	9
554	180	2.0	9.1	0.89	0.67	5.3	9

5.4 Microcrystalline SiC

In the deposition of μc-SiC, we used a gas mixture of SiH_4, H_2, BF_3 and CH_4 and started with the deposition conditions which produce a high quality μc-Si p-layer. Table 5-3 displays cell data for devices with p-layers made with different methane flows at substrate temperatures of 140 ^oC and 180 ^oC. As can be seen from the table, devices with μc-SiC p-layers show slightly higher J_{sc} as compared with μc-Si p-layers deposited at 180 ^oC. However, μc-Si p-layer deposited at 140 ^oC results in the same J_{sc} value as that for μc-SiC. We have also investigated deposition of μc-SiC p-layer at 140 ^oC and found that the lower temperature results in a device with a higher R_s and a lower FF. This is likely due to an observed powder formation in the deposition chamber.

Table 5-3 Properties for cells made with varying amounts of CH_4 flow and different substrate temperatures while all other parameters were nominally fixed.

Sample	Subst. Temp. (^oC)	Relative CH_4 flow (sccm)	J_{sc} (mA/cm^2)	V_{oc} (V)	FF	P_{max} (mW/cm^2)	R_S (Ωcm^2)
684	140	0	11.1	0.93	0.66	6.8	8.6
685	140	0	11.1	0.92	0.68	6.9	7.3
686	180	0	10.8	0.93	0.69	6.9	8.5
687	180	0	10.7	0.91	0.66	6.4	7.3
690	180	1.0	11.6	0.94	0.64	7.0	8.6
691	180	1.0	12.0	0.91	0.65	7.1	7.6
692	180	2.0	11.5	0.93	0.64	6.9	8.5
693	180	2.0	11.8	0.92	0.65	7.0	8.0

While the as-deposited μc-SiC p-layers deposited at 180 ^oC show performance similar to that of the μc-Si p-layer, they degraded with long-term air exposure. Table 5-4 shows performance of devices with μc-SiC p-layer and μc-Si p-layer before and after weeks of air exposures. Performance of devices with μc-Si p-layers is unchanged while those with μc-SiC p-layers degraded significantly. From Auger measurement, we found a significant amount of oxygen in

the unstable μc-SiC p-layers. We suspect that the changes with air exposure are related to the formation of a porous, columnar microstructure.

We have also studied the deposition of μc-Si and μc-SiC with relatively less hydrogen dilution compared with devices shown in Table 5-4. Table 5-5 shows the performance of devices with both μc-SiC and μc-Si p-layers. The J_{sc} of the μc-Si device has decreased. However, the J_{sc} and other solar cell performance characteristics of the μc-SiC device remain the same. Therefore, before any extended air exposure, the solar cell performance of devices with μc-SiC p-layer is superior to that of μc-Si p-layers deposited at this same dilution level.

Table 5-4 Properties for cells with μc-Si and μc-SiC p-layers, before and after the devices are exposed to air for an extended period of time.

Sample	Relative CH_4 flow (sccm)	When J-V curve taken	J_{sc} (mA/cm^2)	V_{oc} (V)	FF	P_{max} (mW/cm)	R_s (Ωcm^2)
615 μc-Si p^+	0	< 24 hrs after deposition	10.4	0.957	0.647	6.43	8.5
		2 months after deposition	10.4	0.949	0.644	6.39	8.7
713 μc-Si p^+	0	< 24 hrs after deposition	11.7	0.942	0.638	7.00	8.7
		3 weeks after deposition	11.7	0.939	0.639	7.04	8.5
705 μc-SiC p^+	1.5	< 24 hrs after deposition	12.0	0.952	0.661	7.58	6.9
		2 days after deposition	11.8	0.910	0.615	6.59	9.7
719 μc-SiC p^+	1.5	< 24 hrs after deposition	11.9	0.932	0.665	7.35	7.9
		2 days after deposition	11.9	0.904	0.607	6.53	9.1

5.5 Summary

We have studied the use of boron doped microcrystalline SiO and SiC alloy systems as wide bandgap p-layers for n-i-p devices. In both cases, because of powder formation, substrate temperatures higher than those typically used to deposit our μc-Si p-layers were required to make the best material with reasonable FF. However, use of these higher temperatures caused lower V_{oc} values to be obtained. For the SiC alloys, higher short circuit currents and better efficiencies were found in the initial state for p-layers prepared with CH_4 under moderate hydrogen dilution conditions, and no benefit was found when higher dilution conditions were used.

Table 5-5 Properties for cells made with relatively less hydrogen dilution compared with samples shown in Table 5-4 and varying amounts of CH_4 flow while all other parameters were nominally fixed.

Sample	Relative CH_4 flow (sccm)	J_{sc} (mA/cm^2)	V_{oc} (V)	FF	P_{max} (mW/cm^2)	R_s (Ωcm^2)
579	0	9.6	0.92	0.67	5.9	7.8
617	0	9.7	0.94	0.66	6.0	8.6
580	0.05	9.9	0.93	0.67	6.2	7.9
574	0.13	9.8	0.92	0.67	6.0	7.5
599	0.30	10.1	0.89	0.66	6.0	7.5
600	0.50	10.5	0.90	0.67	6.3	6.9
617	0.50	11.3	0.90	0.65	6.6	7.7
620	0.80	10.9	0.95	0.66	6.8	7.9
619	1.2	11.3	0.92	0.65	6.7	8.2
626	1.2	10.8	0.90	0.68	6.6	6.8
624	2.4	11.3	0.91	0.65	6.6	8.2
625	3.2	11.2	0.90	0.67	6.7	7.5

Section 6
Schottky Barrier Device as an a-Si Alloy Materials Evaluation Tool

6.1 Introduction

The deposition of a-Si alloy materials including a-Si, a-SiGe and a-SiC is often optimized using single layer measurements such as photoconductivity, Photothermal Deflection Spectroscopy (PDS), Constant Photocurrent Method (CPM) or Steady State Photocarrier Grating Technique (SSPG). Recent reports indicate that none of these material characterization tools can reliably predict the performance of a material in a solar cell device.[25] An alternative, reliable and easy measurement for the photovoltaic properties of materials is therefore desirable.

The metal/a-Si(n^+)/a-Si alloy/metal Schottky barrier device has been widely used as an alternative evaluation tool for the photovoltaic performance of a-Si alloy material, since it: 1) more reliably reflects the carrier transport in a solar cell than the conventional material characterization tools previously mentioned, and 2) is easier to fabricate than a complete solar cell. However, such a device still requires the deposition of an n^+ a-Si layer and thus a multiple chamber device producing system, since one does not want to deposit the a-Si intrinsic material to be studied together with an n^+ layer in the same chamber.

In this work, we have studied a new Schottky barrier device with a heavily doped n-type c-Si substrate for the back ohmic contact. Such a new test structure is easily fabricated and therefore can be widely used as an evaluation tool for measuring a-Si alloy transport properties. With n^+ c-Si rather than n^+ a-Si, laboratories which only have single chamber systems can conveniently produce these devices without having to prepare doped layers.

6.2 Device Structure, Fabrication and Measurement

The specific structure of the device we used is: c-Si(n^+)/a-Si alloy/Pd. In this device, a Schottky barrier is formed at the a-Si/metal contact and an ohmic contact is formed at the c-Si(n^+)/a-Si interface. The c-Si is a heavily phosphorus doped crystalline wafer substrate with resistivity lower than 0.02 Ωcm. We selected a thin Palladium metal layer for the semitransparent Schottky contact, as was done in other laboratories, because of its high work function.[32]

For the production of the devices, the c-Si wafer was etched in a buffered HF solution for a few minutes prior to loading into the chamber for the a-Si alloy growth to remove the surface oxide layer. This was followed by a deionized water rinse and blow dry. After loading, the substrates were baked at 250 ^oC for 30 min and then etched with a hydrogen plasma for 2 minutes.

Together with the c-Si substrates, a set of SS substrates, precoated with an a-Si n^+ layer, were also loaded into the system for the deposition of reference n-i-p solar cells. After a-Si alloy i-layer deposition and the removal of the c-Si/a-Si alloy samples from the multiple chamber deposition system, these SS/a-Si(n^+)/a-Si alloy samples were loaded into the p chamber for deposition of the μc-Si p-layer, while the c-Si(n^+)/a-Si alloy samples were immediately transferred to a vacuum

evaporator for the Pd deposition. An effort was made to minimize the exposure of the sample to air to less than 10 min. A glass substrate was also loaded into the evaporation system for monitoring the thickness and the optical transmission of the Pd layer. Approximately 50-200Å of Pd was evaporated at a rate of 0.2Å/s at nominally room temperature through a mask to complete the c-Si/a-Si/Pd Schottky barrier device.

In measuring the J-V characteristics for these devices, we applied a drop of Ag paste at a corner of the Pd film to assure good contact between the probe and the metal film. Ag was also applied as a paste or an evaporated layer to the other side of the c-Si substrate to improve the probe contact.

6.3 Results

Figure 6-1 illustrates the J-V curves for a c-Si(n^+)/a-Si/Pd device with a 2000Å thick i-layer measured under our typical AM1.5 white light (curve a), the same simulator light after a red cut-on filter (curve b) and a broadened 628 nm HeNe laser light with a flux of 10^{16} photons/cm^{2}sec (curve c). The curves in (b) and (c) were enlarged by a factor of 10 in Figure 6-1 for clarity. Measurement with the HeNe light has several advantages: the light is more uniformly absorbed by the material, the photon flux can be easily calibrated so that the short circuit current and the quantum efficiency can be calculated, and the laser itself is usually available in most laboratories. From curve (a), the FF is around 0.59. The V_{oc} is 0.47 V, which is typical for a Schottky barrier device with a barrier height of 0.9-1.0 V at room temperature. The J_{sc} of 3.5 mA/cm^2 is lower than that for a standard n-i-p device with similar intrinsic layer thickness due to the absorption of Pd film and Pd_2Si formed at the a-Si/Pd interface.[34]

In order to demonstrate the response of the Schottky barrier device FF to the deposition conditions of the intrinsic a-Si alloy material, we have fabricated devices with different a-Si and a-SiGe intrinsic layers to show the dependence of the device performance on the intrinsic layer quality and thickness. Table 6-1 lists the device performance data for all of the Schottky barrier devices and the reference n-i-p solar cells, fabricated at the same time in the same i-layer deposition. The first set of data in the top of the table is for the a-Si Schottky devices with different intrinsic layer thicknesses and an a-SiGe Schottky device with a 2000 Å thick i-layer. The second set of data is for n-i-p devices which were made with a vacuum break between the layers so that the Schottky barrier devices can be made at the same time. The third set of data is for n-i-p devices made without vacuum breaks between the different layer depositions. We observed that the FF for all of these devices decrease with increased Ge content in the a-SiGe alloy and with increased thickness of the a-Si layer, as should be expected. The correlation in FF between the Schottky barrier devices and the reference n-i-p devices is consistent.

Compared with the FF measured under the simulator light, the FF_r measured under a weak red light, such as the HeNe laser light, better reflects the intrinsic layer quality since red light is more uniformly absorbed by the bulk intrinsic material and thus depends less on any possible variations at the interfaces. To better show the correlation, Figure 6-2 plots the FF for Schottky barrier devices as a function of those for the n-i-p devices. For the FF measured with both the HeNe light and the simulator light after a red filter, we observed a good correlation. With the

measured FF for a Schottky barrier device made with a new material, one could use the trend seen in Figure 6-2 to find the expected FF of an n-i-p device made with this material. Of course, since the FF for an n-i-p solar cell depends also on other device layers, such as the p, n and ITO layers, the relation in Figure 6-2 should not be extrapolated for devices made at different laboratories. However, the relative change in the FF of the Schottky barrier device for materials made with different deposition conditions can be used as a yard stick for the optimization of the intrinsic layer deposition.

Finally, the c-Si(n^+)/a-Si alloy/Pd Schottky barrier device has several advantages over the n-i-p solar cell as an a-Si alloy evaluation tool. It can be easily fabricated, its FF under weak HeNe light depends less sensitively on the p/i interface (due to the easy formation and good reproducibility of the Pd_2Si interface), and the use of the c-Si(n^+) as the substrate minimizes the deposition of other solar cell layers such as p, n and ITO layers. We believe that this is an excellent tool for laboratories with single chamber systems to use.

6.4 Summary

The c-Si(n^+)/a-Si alloy/Pd Schottky barrier device studied here can be used as an evaluation tool for the photovoltaic properties of solar cell materials. Such a device has been demonstrated to provide reliable and direct information on the photovoltaic properties. In addition, due to the simplicity of the device structure, it can be fabricated without multichamber solar cell deposition facilities. Such a new device structure can be used for effective optimization of deposition conditions for amorphous silicon alloy material fabrication.

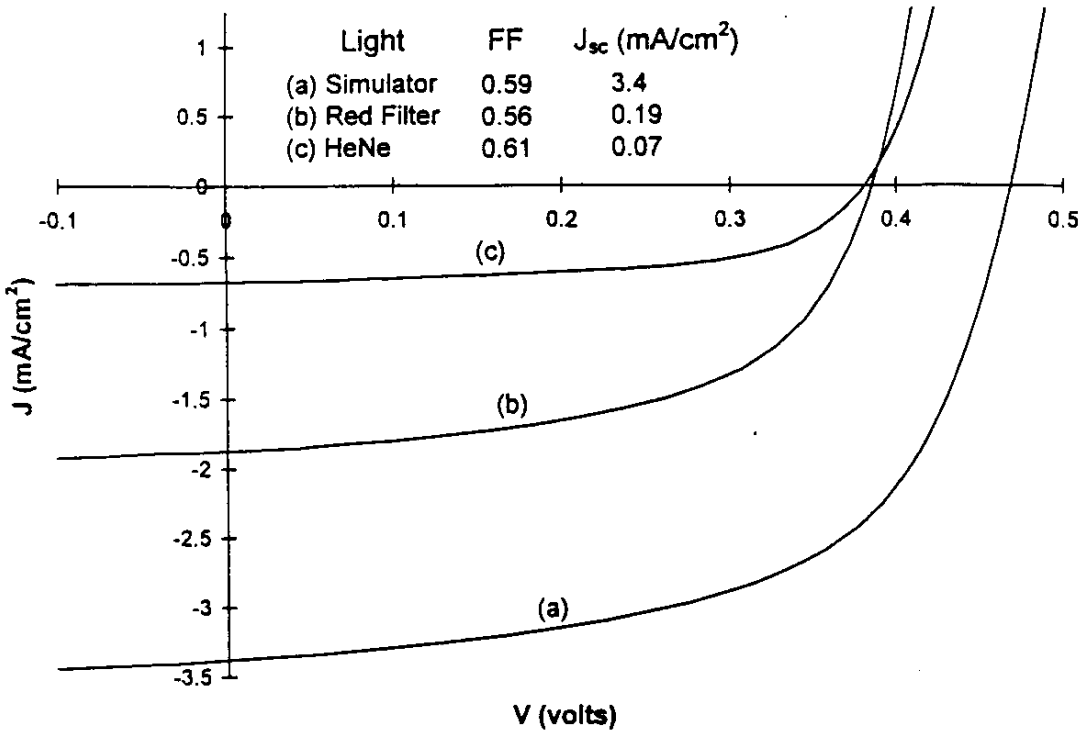

Figure 6-1 J-V curves of a c-Si(n+)/a-Si/Pd Schottky barrier device measured under (a) solar simulator; (b) weak red light; and (c) HeNe laser light.

Table 6-1 J-V performance of c-Si (n^+) / a-Si alloy/Pd Schottry barrier devices and a-Si alloy n-i-p solar cells under the illumination of different lights.

Devices	i-layer thickness (Å)	Simulator (100 W/cm^2)						HeNe Laser (10^{16} photons/cm^{2}s)		
		FF	J_{sc} (mA/cm^2)	V_{oc} (V)	R_s (Ω/cm)	FF_r	FF_b	FF	J_{sc} (mA/cm^2)	V_{oc} (V)
c-Si/a-Si:H/Pd	2000	0.577	3.5	0.47	20	0.570	0.610	0.602	0.07	0.38
c-Si/a-Si:H/Pd	3000	0.536	3.9	0.48	25	0.542	0.580	0.564	0.12	0.39
c-Si/a-si:H/Pd	4000	0.552	4.6	0.49	19	0.515	0.605	0.530	0.15	0.40
c-Si/a-Si:H/Pd	5000	0.474	4.5	0.48	37	0.460	0.507	0.479	0.20	0.41
c-Si/a-SiGe:H/Pd	2000	0.31	5.1	0.48	16	0.492	0.513	0.511	0.31	0.24
N / I / P a-Si:H	2000	0.594	9.8	0.95	24	0.664	0.720	0.673	0.33	0.82
N / I / P a-Si:H	3000	0.530	10.8	0.95	24	0.524	0.691	0.555	0.52	0.83
N / I / P a-Si:H	4000	0.516	11.2	0.95	16	0.452	0.684	0.464	0.71	0.83
N / I / P a-Si:H	5000	0.493	12.0	0.95	18	0.410	0.669	0.434	0.73	0.82
N / I / P a-SiGe:H	2000	0.484	12.8	0.65	16	0.498	0.630	0.524	1.0	0.54
nip a-Si:H	2000	0.657	11.2	0.95	11	0.655	0.749	-	-	-
nip a-Si:H	3000	0.601	12.1	0.94	8.9	0.570	0.735	-	-	-
nip a-Si:H	4000	0.560	13.0	0.94	9.1	0.503	0.728	-	-	-
nip a-Si:H	5000	0.534	13.3	0.94	9.2	0.415	0.720	-	-	-

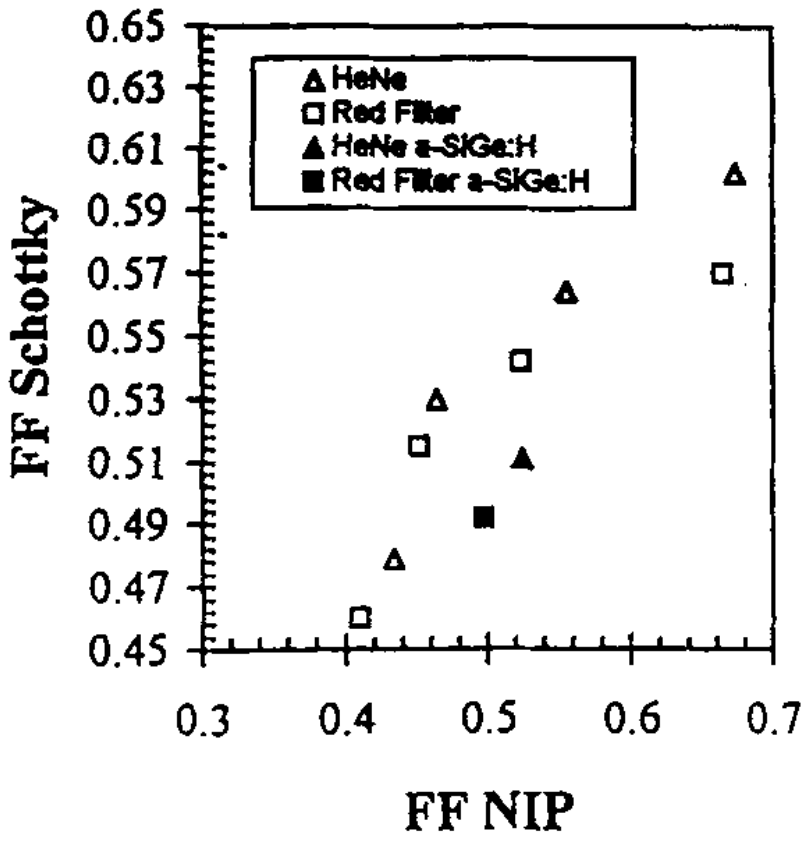

Figure 6-2 Correlation of FF for Schottky barrier devices and regular a-Si n-i-p solar cell devices having the same i-layer.

Section 7
High Rate Deposition of a-Si Using VHF Plasmas

7. 1 Introduction

The high rate deposition of a-Si using VHF has previously been studied .[35,36] However, the focus of most of these studies was on the thin film properties of the VHF deposited materials. Few studies were carried out using solar cell devices to characterize the VHF material and those that were used the glass superstrate structure rather than the stainless steel (SS) based substrate structure used by ECD.[36] In this study, we have investigated the application of VHF plasma deposited a-Si material in substrate type solar cells. It is generally found that the deposition rate of a-Si on a conductive substrate such as SS is often sizably higher than that on glass under otherwise identical deposition conditions. Therefore, the feasibility study involving a substrate type solar cell structure is important for the high rate a-Si material deposited using a VHF plasma.

7.2 High-rate deposition of a-Si for solar cells on SS substrates using a VHF plasma

We investigated the deposition of a-Si for SS substrate type solar cells using a VHF plasma under various deposition conditions. Table 7-1 shows the device performance for five groups of solar cells having the i-layer deposited at different VHF powers, silane flows, and/or pressures. Variation of such a large number of conditions lead to a large variation in the i-layer deposition rates. The deposition times for the i-layer were adjusted so that the thickness is around 2500 Å. All of these solar cells were deposited on bare SS substrate without the use of back-reflectors. The data in Table 7-1 is an average for many solar cells on the same sample piece. The hydrogen flow in the gas mixture is the same for all these samples. Let us first look at samples in group 1 (Samples 4 to 11) for which the deposition pressure was 0.5 Torr. As we see from the table, with increasing power from 2 W up to 15 W, the deposition rate increases from 1.4 Å/s up to 5.3 Å/s as expected. However, the device performance as indicated by V_{oc}, J_{sc} and FF and maximum power output P_{max} remain approximately the same. This result is important since higher rate deposition of a-Si with the same device quality would result in a significant reduction in manufacturing cost. With the VHF power further increased to 30 W, the further increase in deposition rate was small, yet the a-Si material quality experienced a sizable deterioration.

Another way to increase the deposition rate is by increasing the chamber pressure. Samples 12-18 (group 2) have i-layers deposited at 1 Torr. Compared with Sample 10, Sample 16 showed an 88% increase in deposition rate when the pressure was increased from 0.5 to 1 Torr. Samples deposited under 1 Torr showed a similar trend as those deposited under 0.5Torr, i.e., a higher VHF power leads to a higher deposition rate, yet no apparent deterioration was observed in the device performance.

Table 7-1 Intrinsic layer growth conditions and the performance of solar cells with VHF i-layers.

Table 2 Intrinsic layer growth conditions and the performance of solar cells with VHF i-layers.

Sample No.	Group No.	Ref. No.	SiH4 (sccm)	H2 (sccm)	Power (W)	P (Torr)	Dep. time (min)	d (A)	Dep. rate (A/s)	Voc (V)	Jsc (mA/cm2)	FF	Pmax (mW/cm2)	Stability 1000hrs (%)
Sample 4	1	L2636	5	Std	2	0.5	30	2530	1.4	0.938	10.14	0.67	6.37	
Sample 5	1	L2638	5	Std	4	0.5	15	2600	2.89	0.956	9.97	0.676	6.44	
Sample 6	1	L2697	5	Std	4	0.5	13.5	2360	2.9	0.95	10.4	0.692	6.88	86.7
Sample 7	1	L2652	5	Std	6	0.5	11.5	2540	3.68	0.963	9.97	0.695	6.67	
Sample 8	1	L2699	5	Std	6	0.5	10	2550	4.3	0.961	10.27	0.686	6.77	86.2
Sample 9	1	L2644	5	Std	10	0.5	8.17	2400	5	0.966	9.55	0.68	6.28	
Sample 10	1	L2653	5	Std	15	0.5	8	2530	5.26	0.957	10.02	0.677	6.49	
Sample 11	1	L2654	5	Std	30	0.5	5.83	2340	6.67	0.973	8.44	0.64	5.25	
Sample 12	2	L2701	5	Std	4	1	21	2190	1.74	0.926	9.65	0.687	6.14	83.8
Sample 13	2	L2711	5	Std	6	1	14.5	2520	2.9	0.941	11.27	0.673	7.14	78.9
Sample 14	2	L2707	5	Std	10	1	5.83	2940	8.4	0.957	10.04	0.679	6.52	81.8
Sample 15	2	L2706	5	Std	15	1	3.83	2340	10.2	0.956	8.46	0.69	5.58	85.5
Sample 16	2	L2656	5	Std	15	1	4.5	2670	9.9	0.977	9.58	0.696	6.51	90
Sample 17	2	L2694	5	Std	15	1	4	2800	10.93	0.965	9.65	0.67	6.12	
Sample 18	2	L2702	5	Std	20	1	3.5	2480	11.8	0.956	9.2	0.674	5.93	87.7
Sample 19	3	L2698	10	Std	15	1	2.5	2220	14.8	0.963	8.96	0.69	5.96	
Sample 20	3	L2655	10	Std	15	1	3	2600	14.5	0.957	9.36	0.702	6.19	81
Sample 21	3	L2712	10	Std	20	1	2.5	2560	17	0.961	9.6	0.67	6.18	
Sample 22	3	L2704	12	Std	20	1	2.33	2480	17.7	0.954	9.33	0.68	6.05	74.2
Sample 23	3	L2662	12	Std	20	1	2.5	2680	17.89	0.957	9.46	0.675	6.1	
Sample 24	3	L2708	12	Std	40	1	1.5	2230	24.8	0.943	9.56	0.671	6.04	78.1
Sample 25	3	L2674	12	Std	40	1	1.58	2460	25.9	0.957	9.16	0.678	5.95	
Sample 26	4	L2661	10	Std	15	1.5	3.67	2480	11.29	0.954	9.12	0.675	5.9	
Sample 27	4	L2660	10	Std	15	2	2.33	1110	7.94	0.949	5.4	0.672	3.45	
Sample 28	5	L2688	2.5	Std	15	1	7.33	2280	5.18	1.01	8.65	0.668	5.83	
Sample 29	5	L2690	1	Std	15	1	42	3000	1.19	0.405	8.09	0.585	1.92	

To further increase the deposition rate, i-layers were deposited with higher SiH_4 flows and increased power, as is shown for Samples 19-25. Essentially no apparent deterioration in device performance was observed when the deposition rate was around or below 10 Å/s.

The initial cell efficiencies (diamonds, in the figure) for a number of cells prepared under a variety of conditions are plotted as a function of deposition rate in Figure 7-1. All of the cells had J_{sc} near 10 mA/cm^2 and i-layers which were roughly 2300 Å thick. This figure displays the strong dependence of the efficiency on the deposition rate. Below a deposition rate of 12-13 Å/s, the initial cell efficiencies are relatively the same with the small amount of scatter (±5%) related to experimental measurement procedures and variations in a few deposition parameters. Beyond 13 Å/s, the initial efficiencies are lower. The 6.4-6.6% efficiencies are typical for those cells whose

i-layers were prepared using the standard 13.56 MHz frequency at 1 Å/s in the same deposition reactor. The fact that we can prepare cells with the same efficiencies up to 10 Å/s using the VHF is contrary to what is found using the 13.56 MHz signal where the efficiencies degrade almost linearly with increasing deposition rate[12].

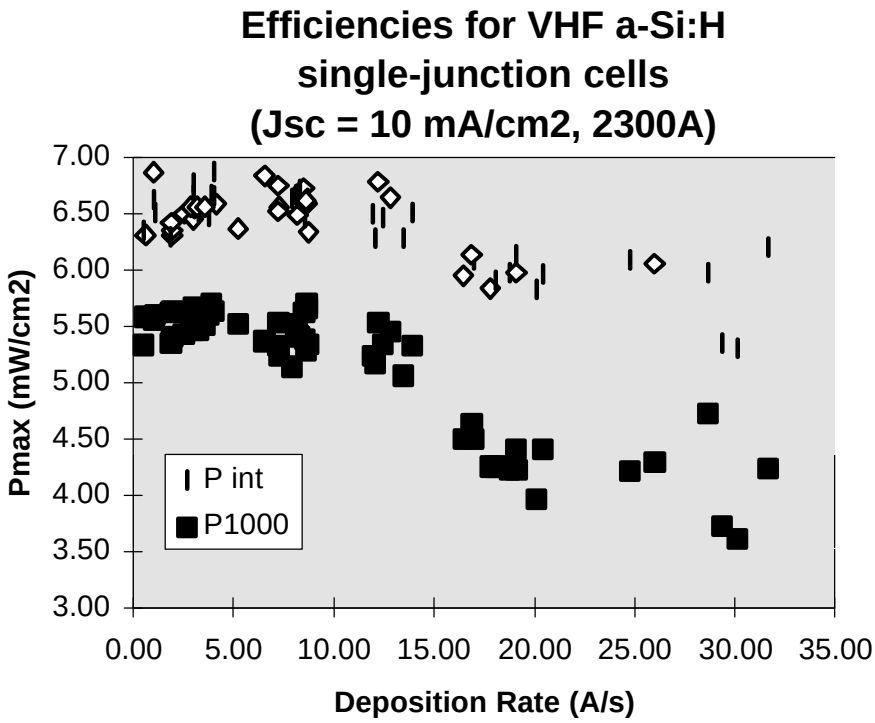

Figure 7-1 Cell efficiencies for a-Si:H devices with Jsc = 10 ± 0.5 mA/cm^2.

Also included in Figure 7-1 are efficiencies for the same cells after the cells had been light soaked for 1000 hrs. under AM1.5 conditions at 50°C (squares in the figure). We remind the reader that it is recognized that after 1000 hrs. of light soaking, the efficiencies are said to be stable and will not degrade further with additional light soaking. Within the scatter of the data, the light soaked efficiencies for cells with i-layers deposited at deposition rates below 10 Å/s are similar. This result is also contrary to what has been observed for cells whose i-layers were prepared by the standard 13.56 MHz method. The percentage of degradation for the standardly produced cells increases again almost linearly with increasing deposition rate[12]. Thus, with this new VHF technique, one can produce high quality a-Si:H single-junction cells at much higher deposition rates than those obtainable with the standard 13.56 MHz standard technique.

Besides using VHF plasma to search for high rate deposition, we also used a VHF plasma to deposit intrinsic a-Si with wider bandgap at relatively lower substrate temperatures. This wider bandgap leads in turn to a higher V_{oc}. A high hydrogen dilution approach was used for depositing wider bandgap a-Si material. As we can see from Samples 28 in Table 7-1, a two fold reduction in SiH_4 flow, therefore a two fold increase in hydrogen dilution, leads to an increase in V_{oc} up to

1.01 V. Further increases in hydrogen dilution causes the formation of microcrystals in the material which results in a significant drop in V_{oc} and FF (See Sample29 in Table 7-1).

Figure 7-2 shows the time dependence of P_{max} upon light soaking for a VHF device (Sample 16). We see that the device performance have come to an equilibrium within 100 hours of light exposure. In fact, the majority of degradation occurred during the initial 3 hours of light soaking.

The type of a-Si solar cell investigated in this study is to be used as the top cell in a triple-junction solar cell. A top-cell is usually deposited directly on the middle component cell rather than directly on a back-reflector. The majority of the i-layer optimization was therefore performed on SS substrates without the use of a back-reflector. However, we have also deposited a VHF device on a textured Ag/ZnO back-reflector for an evaluation purpose. Figure 7-3 shows an J-V curve for a single-junction a-Si solar cell with the i-layer deposited using VHF plasma deposition, showing an initial solar cell efficiency of 10.6%, which is comparable, if not better, than what we usually obtained for a-Si solar cells deposited using RF plasma deposition in the same deposition system.

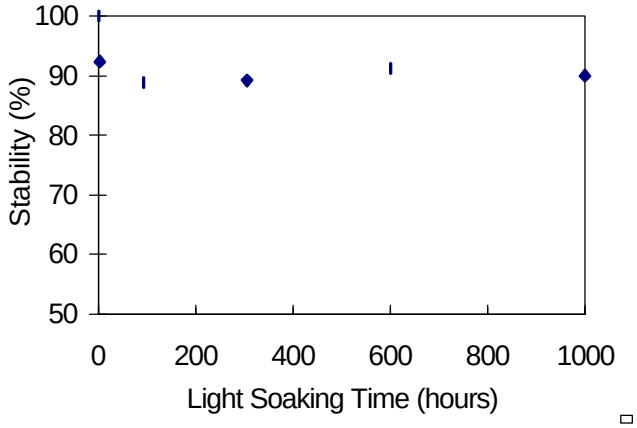

Figure 7-2 Light soaking degradation of a VHF device as a function of light soaking time.

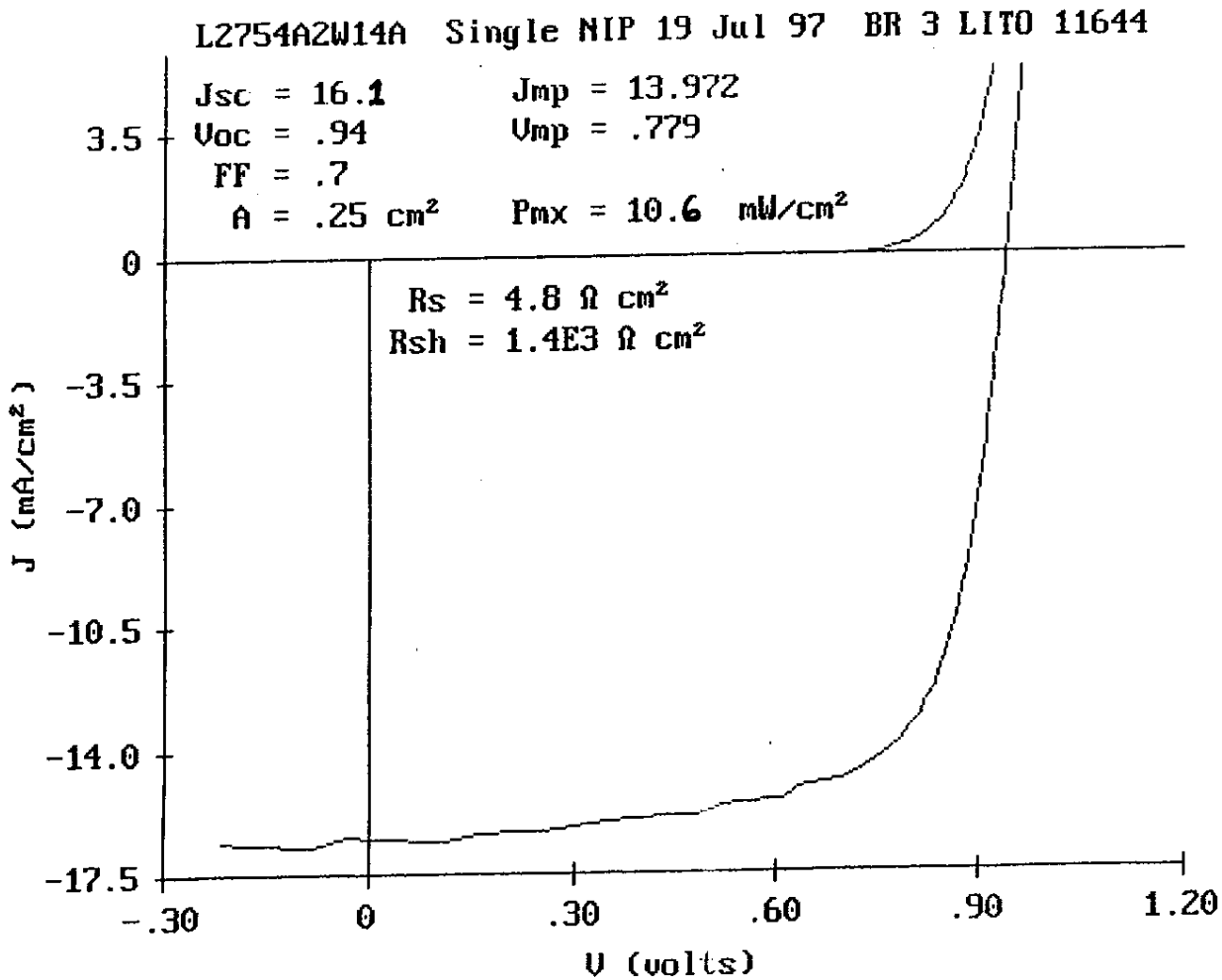

Figure 7-3 J-V curve of a single-junction a-Si solar cell with the i-layer deposited using VHF plasma deposition.

In Table 7-2, we compare the light stability of a-Si solar cells with i-layers deposited using VHF and RF at both high and low deposition rates. All devices in Table 7-2 have i-layer thicknesses around 2500 Å and were deposited on bare stainless steel without back-reflectors. After 1000 hours of light soaking under one sun light at 50 ^{o}C, optimized i-layers deposited in the same system using an RF plasma at low deposition rate (0.61 Å/s) lead to a light degradation of 14.3% while i-layers deposited using VHF at 10 Å/s lead to a light degradation of only 10% for otherwise identical devices. Although the degradation of a VHF device with i-layer deposited at 24.8 Å/s increased to around 22%, that of an RF device with i-layer deposited at 16 Å/s (a lower rate) showed a degradation of 36% (a higher degradation). Therefore, VHF deposited i-layers show superior stability properties compared to RF i-layers when deposited at high rates.

Table 7-2 Comparison of light soaking stability between devices with i-layers deposited using RF and VHF.

Sample No.	Ref. No.	Plasma Frequency (MHz)	Dep. Rate (Å/s)	Initial P_{max} (mW/cm^2)	Light degrad. (%)
Sample 30	L2710	RF (13.56)	0.61	6.65	14.3
Sample 16	L2656	VHF (70)	9.9	6.51	10
Sample 31	L2715	RF (13.56)	16	5.3	36.2
Sample 24	L2708	VHF (70)	24.8	6.04	21.9

7.3 Summary

For the deposition of i-layers at high rate using a VHF plasma, we were able to fabricate solar cells with a-Si i-layers deposited at rates as high as 10 Å/s yet with similar device performance and light stability as the low-rate deposited samples. The i-layers deposited using a VHF plasma at high rates show superior performance and better stability than i-layers deposited in the same deposition system at high rate using a conventional RF plasma. As an additional benefit, the VHF process can be easily incorporated into a large scale production process such as ECD's continuous roll-to-roll a-Si PV production line.

Section 8
High Rate Deposition of a-SiGe Using VHF Plasmas

We have extended our high-deposition-rate VHF study from a-Si:H to a-SiGe alloys.[37] There are three i-layers in our triple-junction a-Si alloy based solar cells. Besides a-Si:H for the top cell i-layer, we also use a-SiGe layers with different amounts of Ge in the alloy for the middle and bottom cell absorber layers. In order to increase the manufacturing throughput of a-Si PV modules, high-rate deposition of high quality a-SiGe alloy materials is important.

We have recently studied the high rate deposition of a-Si:H without Ge and obtained stable a-Si:H materials at a rate up to 10 Å/s while the quality and light stability of the high-rate deposited a-Si:H are as good as those made at lower i-layer deposition rates. In this work, we are focusing on the high rate deposition of a-SiGe alloys using a VHF plasma.

The i-layer deposition conditions, including VHF power, SiH_4 or Si_2H_6 flows, GeH_4/SiH_4 ratios, H dilution, substrate temperature were varied to optimize the i-layer quality. At this moment, we are focusing our study on using SiH_4 rather than Si_2H_6 due to the lower gas cost of SiH_4 gas. Single-junction a-SiGe solar cells having the a-SiGe i-layers were used to evaluate the quality of VHF plasma deposited a-SiGe alloys.

In order to understand the dependence of the i-layer quality and the solar cell performance on the growth conditions, we explored the deposition parameters using a Design of Experiments (DOE) approach. A 4-factor Draper-Lin small composite design with face-centered design characteristics was used to study the dependence of a-SiGe quality on the following crucial deposition parameters: VHF power, SiH_4 gas flow, hydrogen dilution, substrate temperature. Table 8-1 lists the deposition conditions for the 18 experiments that were conducted for this experimental design. Except those parameters listed in this table, other deposition and device parameters including GeH_4 flow for the a-SiGe i-layer, the chamber pressure, and all the deposition conditions for the doped layers were kept the same.

Figures 8-1 and 8-2 show the dependence of V_{oc} on the various parameters. V_{oc} depends strongly on the temperature, the applied power and the SiH_4 flow. With increasing SiH_4 flow, V_{oc} increases due to the widening of the i-layer bandgap with the addition of more Si to the lattice. The increase in V_{oc} with increasing applied power is likely related to a combination of three effects, 1) an increased amount of hydrogen in the i-layers, 2) an increased amount of preferential etching of Ge from the film surface, and 3) an increased amount of silane decomposition. As the substrate temperature is increased, the hydrogen content decreases causing the observed decrease in V_{oc}. We used this data obtained using the DOE method to pinpoint the various combinations of conditions where the V_{oc}=0.70-0.75 V and near each of these conditions found the optimum cell properties.

Table 8-1 Deposition parameters and the experimental results using a Design of Experiments.

run #	trial #	SiH4(sccm)	H2 dilution	Temp(C)	Power(W)	D-rate(A/S)	Voc(V)	Jsc (mA/cm2)	FF	Pmax (mW/cm2)
L2836	1	2.5	7	250	15	10.3	0.695	11.54	0.567	4.55
L2857	2	3	4	200	20	12.9	0.795	10.25	0.587	4.78
L2838	3	2.5	7	250	10	9.3	0.658	12.66	0.557	4.64
L2839	4	2.5	4	250	15	11.5	0.738	10.33	0.568	4.33
L2855	5	2	10	300	20	5.5	0.576	14.08	0.482	3.91
L2840	6	2	4	300	10	8.5	0.569	11.43	0.421	2.74
L2747	7	2.5	7	300	15	10	0.669	11.26	0.519	3.91
L2845	8	2	7	250	15	9.7	0.674	9.91	0.528	3.53
L2856	9	2	4	200	10	8.6	0.732	10.33	0.531	4.02
L2858	10	3	4	300	20	12.5	0.744	11.23	0.565	4.72
L2848	11	2.5	10	250	15	9	0.669	10.46	0.519	3.63
L2852	12	2	10	200	20	9.2	0.726	7.39	0.530	2.84
L2844	13	2.5	7	250	20	11.1	0.744	10.11	0.577	4.34
L2841	14	3	10	200	10	8.4	0.676	11.29	0.528	4.03
L2851	15	2.5	7	200	15	10.5	0.748	9.96	0.584	4.35
L2854	16	3	10	300	10	5.7	0.566	14.63	0.459	3.80
L2837	17	3	7	250	15	11	0.746	11.27	0.613	5.15
L2853	18	2.5	7	250	15	10.4	0.723	11.62	0.582	4.89

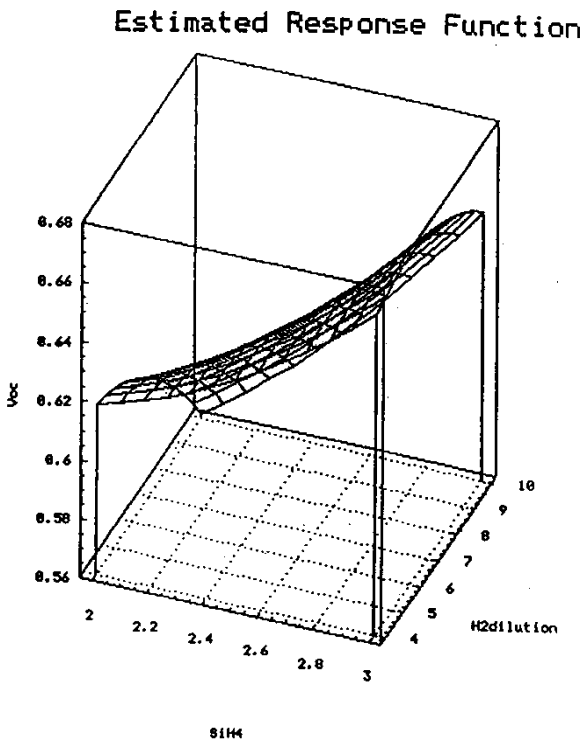

Figure 8-1 Dependence of V_{oc} on the SiH_4 flow and H_2 dilution.

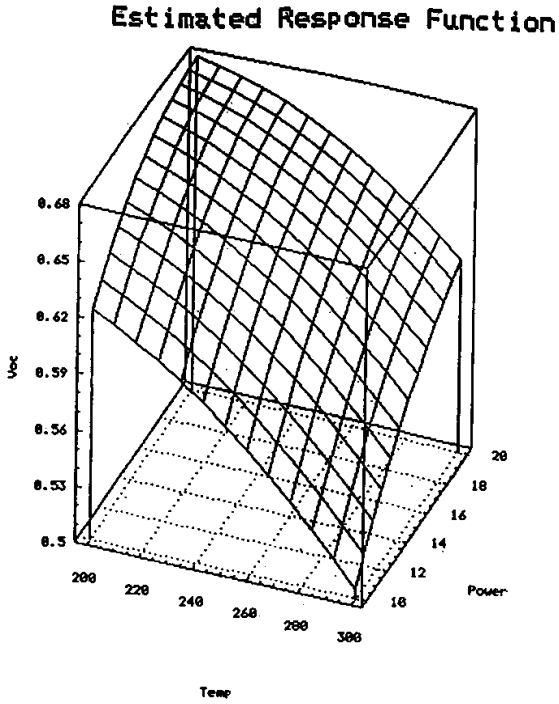

Figure 8-2 Dependence of V_{oc} on the substrate temperature and applied power.

Beyond altering the common parameters (substrate temperature, applied power, gas flows, etc.), we also varied the profiling or grading of the Ge content across the i-layer thickness. For devices prepared by the 13.56 MHz PECVD technique, it is well known that by grading the Ge content across the i-layer such that the largest Ge concentrations in the layer are near the p-layer, one can obtain better minority carrier collection and higher efficiencies. Having the more defective Ge rich material closer to the p-layer, the holes in the Ge-rich material have less distance to travel before getting collected at the p-layer and thus have a lower probability of getting trapped in the highly defective material. In Table 8-2, we compare the properties for two a-SiGe:H cells with V_{oc}=0.74V made with and without Ge profiling. The i-layers for both cells were made using the VHF technique at 10 Å/s. The cell measurements were done prior to light soaking. The cell made with the grading has a higher efficiency due to an improved short circuit current and a higher fill factor. Thus, the Ge profiling is also beneficial for the VHF cells.

Table 8-2 a-SiGe:H cells with i-layers made using VHF at 10 Å/s.

i-layer Ge Grading	Light Meas. Cond.	V_{oc} (V)	J_{sc} (mA/ cm^2)	FF	R_s (Ωcm^2)	P_{max} (mW/ cm^2)
No	AM1.5	0.737	17.7	0.569	5.8	7.41
	AM1.5+ 630 nm cutoff filter	0.678	6.1	0.506	15.7	2.11
Yes	AM1.5	0.739	18.1	0.595	6.3	7.96
	AM1.5+ 630 nm cutoff filter	0.688	6.3	0.569	14.6	2.47

Table 8-3 compares the properties for a-SiGe:H cells prepared under the best conditions, thus far, by the VHF technique at deposition rates of 2 and 10 Å/s. Again the measurements were made prior to light soaking the cells. For these initial measurements, the cells made at the 10 Å/s rate have slightly lower efficiencies to those for cells made at the lower deposition rate. However, this fall off in efficiency with increasing deposition rate is much smaller than what is observed for cells made using the 13.56 MHz technique.

Table 8-3 Properties for a-Si:Ge:H cells prepared at different rates using VHF technique.

Depos. Rate (Å/s)	Light Meas. Cond.	V_{oc} (V)	J_{sc} (mA/ cm^2)	FF	R_s (Ωcm^2)	P_{max} (mW/ cm^2)
2	AM1.5	0.739	19.4	0.599	5.3	8.58
	AM1.5+ 630 nm cutoff filter	0.687	7.3	0.556	12.8	2.78
10	AM1.5	0.739	18.1	0.595	6.3	7.96
	AM1.5+ 630 nm cutoff filter	0.688	6.3	0.569	14.6	2.47

For the cells prepared by the 13.56 MHz method, the efficiency drops by over a factor of two when the deposition rate is increased to 10 Å/s. Thus, there is a benefit to using the VHF technique to prepare a-SiGe:H cells at high rates.

We are presently starting light soaking studies of our best a-SiGe:H cells prepared at 10 Å/s and plan on further optimizing the a-SiGe:H deposition conditions to further improve the cell efficiencies.

In terms of improving the efficiencies for the a-SiGe:H cells, there are several avenues to follow which we did not have a sufficient amount of time to follow in this program. For example, we have yet to fully optimize the a-Si:H buffer layer thicknesses and deposition rates and the i-layer substrate temperatures. The buffer layer properties can strongly affect carrier collection in the cells and thus the cell efficiencies. Also, the substrate temperature used to prepare our best a-SiGe:H layers was at the limit of our present system's capability. We are now in the process of altering our system so that higher substrate temperatures and potentially higher efficiencies can be obtained. We have also yet to make the i-layers using Si_2H_6 rather than SiH_4 as the silicon source. The advantage of using Si_2H_6 is that it has a similar decomposition rate to GeH_4 while the rate for SiH_4 is roughly a factor of two lower. It has been argued that higher quality material is made when the Si and Ge incorporation rates are similar. Thus, higher cell efficiencies may be obtained with use of Si_2H_6. However, Si_2H_6 is roughly nine times more expensive than SiH_4. Since we were testing a new deposition method to reduce costs, we felt that it was more important to test the use of a $SiH_4/GeH_4/H_2$ gas mixture. Thus, we should test the use of Si_2H_6 to see if higher efficiencies can be obtained. We plan to test all of these parameters in the future.

Section 9
Deposition of Microcrystalline Silicon p-Layers Using VHF Plasma

9.1 Introduction

ECD previously developed microcrystalline p materials for use in amorphous silicon solar cell fabrication.[4] Such a p-layer increases solar cell V_{oc}, J_{sc} and FF compared with amorphous p-layers. Upon further refinement, microcrystalline Si p-layer materials have been widely used in a-Si solar cell research and manufacturing to achieve record high solar cell efficiency. However, the process window in parameter space to produce a high performance p-layer is relatively narrow using conventional RF PECVD. Thus high quality p materials can not easily be reproduced at different laboratories or on different manufacturing machines. We have investigated the deposition of μc-Si p materials using a 70 MHz Very High Frequency (VHF) PECVD process[38,39] with the objectives of 1) establishing a wider process window for the deposition of high quality p-materials, and 2) further enhancing the performance of a-Si solar cells by improving its p-layers.

We deposited μc-Si p-materials using a VHF plasma enhanced CVD process in the multi-chamber load-locked LL1 solar cell deposition system. The substrate was a SS/n-i in which the doped n-layer and the undoped a-Si intrinsic layer were deposited previously in a roll-to-roll process. Thus these SS/n-i substrates had high uniformity, which is important for optimizing the p-layer with a wide parameter space.

9.2 Process optimization using Design of Experiment

For the p-layer research, a design of experiments (DOE) approach[40] was used for the exploration and optimization of deposition parameter space. Such statistical analysis is widely used in semiconductor industry when there are many interacting process conditions that affect the final device performance and each experiment is time consuming and costly. By taking advantage of the symmetry and the orthogonality of the designed experiments, we were able to obtain in only a few experiments the amount of information that otherwise requires a large number of experiments without using DOE. The benefit of using DOE would be even greater if more process parameters are involved. The DOE approach has led to the quick optimization of a new deposition process which has a broad parameter space.

Table 9-1 lists the initial deposition parameter space used for the p-layer research. It is a four-factor, five-variable Draper-Lin small composite design with face-centered design characteristic. The limits of the design parameters were carefully selected based on our understanding of the deposition process. These four parameters were chosen because they should most strongly affect the performance of the p-layer. Other parameters which were fixed included the VHF power (75W), the hydrogen flow, and the chamber pressure (2 Torr).

Table 9-1 Design parameters and experimental results for the optimization of VHF deposition of microcrystalline p-layer using a 4-factor Draper-Lin small composite design with face-centered design characteristic. Other deposition parameters including VHF power, hydrogen flow and pressure are kept constant for this set of experiments.

Run #	Exp.#	Temp (°C)	BF_3 (sccm)	SiH_4 (sccm)	Time (min)	V_{oc} (V)	J_{sc} (mA/cm^2)	FF	R_s	P_{max} (mW/cm^2)
L2372	1	100	4	0.6	4	0.879	10.02	0.67	9.7	5.76
L2373	2	100	4	0.8	4	0.88	8.91	0.651	10.8	5.1
L2374	3	100	4	0.6	6	0.81	9.39	0.61	10	4.64
L2375	4	60	6	0.8	6	0.864	9.07	0.633	11.1	4.96
L2376	5	100	4	0.4	4	0.868	9.73	0.64	13	5.29
L2377	6	60	2	0.8	2	0.873	9.09	0.619	19.7	4.91
L2378	7	140	2	0.4	6	0.876	9.12	0.678	8.5	5.3
L2379	8	100	4	0.6	2	0.89	9.83	0.657	10.4	5.75
L2380	9	100	2	0.6	4	0.884	10.13	0.643	12.4	5.76
L2381	10	140	4	0.6	4	0.843	8.48	0.661	8.7	4.73
L2382	11	140	6	0.8	2	0.856	8.51	0.671	8.8	4.89
L2383	12	60	6	0.4	6	0.831	10.31	0.56	36	4.71
L2384	13	100	6	0.6	4	0.891	9.28	0.67	10.9	5.44
L2385	14	140	2	0.8	6	0.882	8.89	0.658	7.1	5.16
L2386	15	60	4	0.6	4	0.889	9.74	0.649	11.2	5.52
L2387	16	140	6	0.4	2	0.88	8.91	0.663	8.2	5.2
L2388	17	60	2	0.4	2	0.861	9.31	0.621	23.6	4.98
L2389	18	100	4	0.6	4	0.887	9.48	0.664	8.9	5.47

Figure 9-1 is the Pareto chart of J_{sc} for n-i-p solar cells with a VHF μc-Si p-layer as a function of temperature, BF_3, SiH_4 and deposition time. It was found that within the above described four dimensional block of parameter space, the J_{sc} is most statistically dependent on the SiH_4 flow and deposition temperature. Figure 9-2 is the response surface plot for the J_{sc} as a function of SiH_4 and temperature while keeping the values of BF_3 and deposition time at the center values (average values). Figures 9-1 and 9-2 suggest that J_{sc} increases with decreasing SiH_4 flow and temperature within the selected parameter ranges. The increase of J_{sc} at low SiH_4 is most likely due to two reasons: 1) the decreased p-layer thickness when less SiH_4 is used in the gas mixture of SiH_4, BF_3 and H_2; and 2) the increased hydrogen dilution (H_2/SiH_4) could increase the microcrystallinity and hence the transmission of the p-layer. The increase in J_{sc} with lower deposition temperature is likely due to the increased microcrystallinity when the process temperature is lowered. As a reminder, the actual substrate temperatures could be much higher than the temperature values read from the thermal couples reported here due to the heating of the substrate by the intense VHF plasma. The surface plot in Figure 9-2 suggests that within the selected parameter space, the optimum J_{sc} value could be achieved at a substrate temperature of 60 ˚C and a SiH_4 flow =0.5 sccm when BF_3 and deposition time are set at 4 sccm and 4 min, respectively.

Figure 9-3 is the Pareto chart for V_{oc} in this set of experiments. The V_{oc} is most sensitive to the deposition time and the first order interaction of substrate temperature and BF_3 flow. The surface response plot in Figure 9-4 also illustrates the dependence of V_{oc} on deposition time and temperature. The decrease in V_{oc} at longer deposition time beyond 3 minutes could be due to the rapid increase of real substrate temperature during the VHF deposition. The Pareto chart in Figure 9-5 is for the total peak power output P_{max} (proportional to efficiency) of the solar cells within the selected parameter space. The dependence of P_{max} on deposition time, temperature and BF_3 are mostly due to the strong dependence of V_{oc} on these parameters. Using the design of experiments, we have successfully surveyed the dependence of solar cell performance on these four crucial parameters using 18 experiments.

We have indeed found a wide parameter space that could produce solar cells with V_{oc} near or above 0.90 V, indicating μc-Si p-material deposition. Figure 9-6 is the J-V curve for a representative device with VHF p-layer after further improvement, showing a V_{oc} of 0.93 V.

9.3. Microcrystalline p-layer using a modified VHF plasma deposition

In order to further improve the performance of p-layers in the solar cells, we have investigated the application of a modified VHF plasma for the μc-Si p-layer growth, with the anticipation that the new process would further improve the solar cell performance and offer an even wider parameter space for the growth of high quality p-layers.[41]

For a comparison with conventionally made p-layers, we explored the deposition of microcrystalline p-layers at VHF (70 MHz) and RF (13.56 MHz) frequencies. Table 9-2 shows the results of solar cells whose p-layers were deposited using these different frequencies. Three types of devices are listed in the table, corresponding to the use of different plasma frequencies

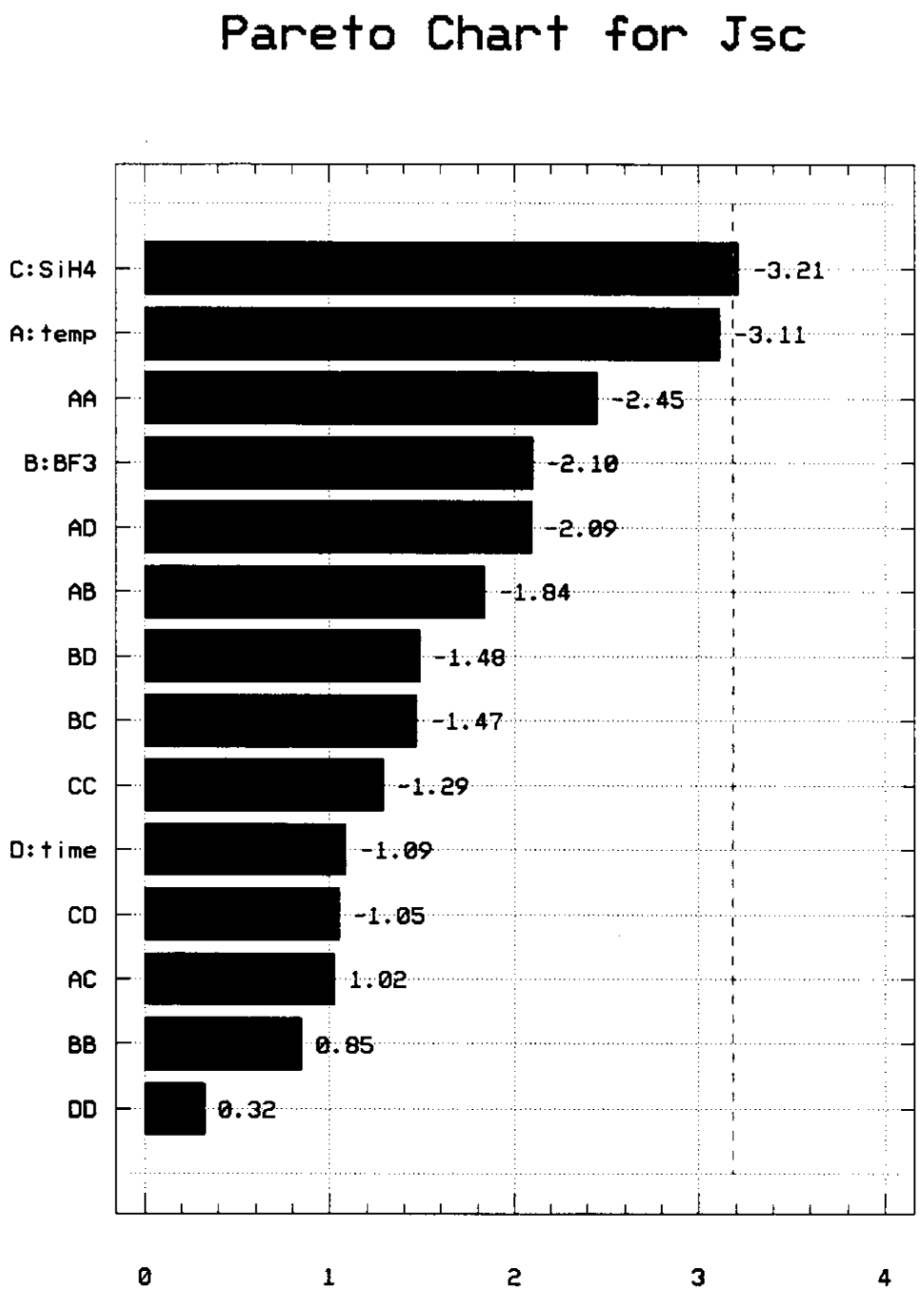

Figures 9-1 Pareto chart for J_{sc} of n-i-p solar cells with VHF μc-Si p-layer as a function of temperature, BF_3, SiH_4 and deposition time.

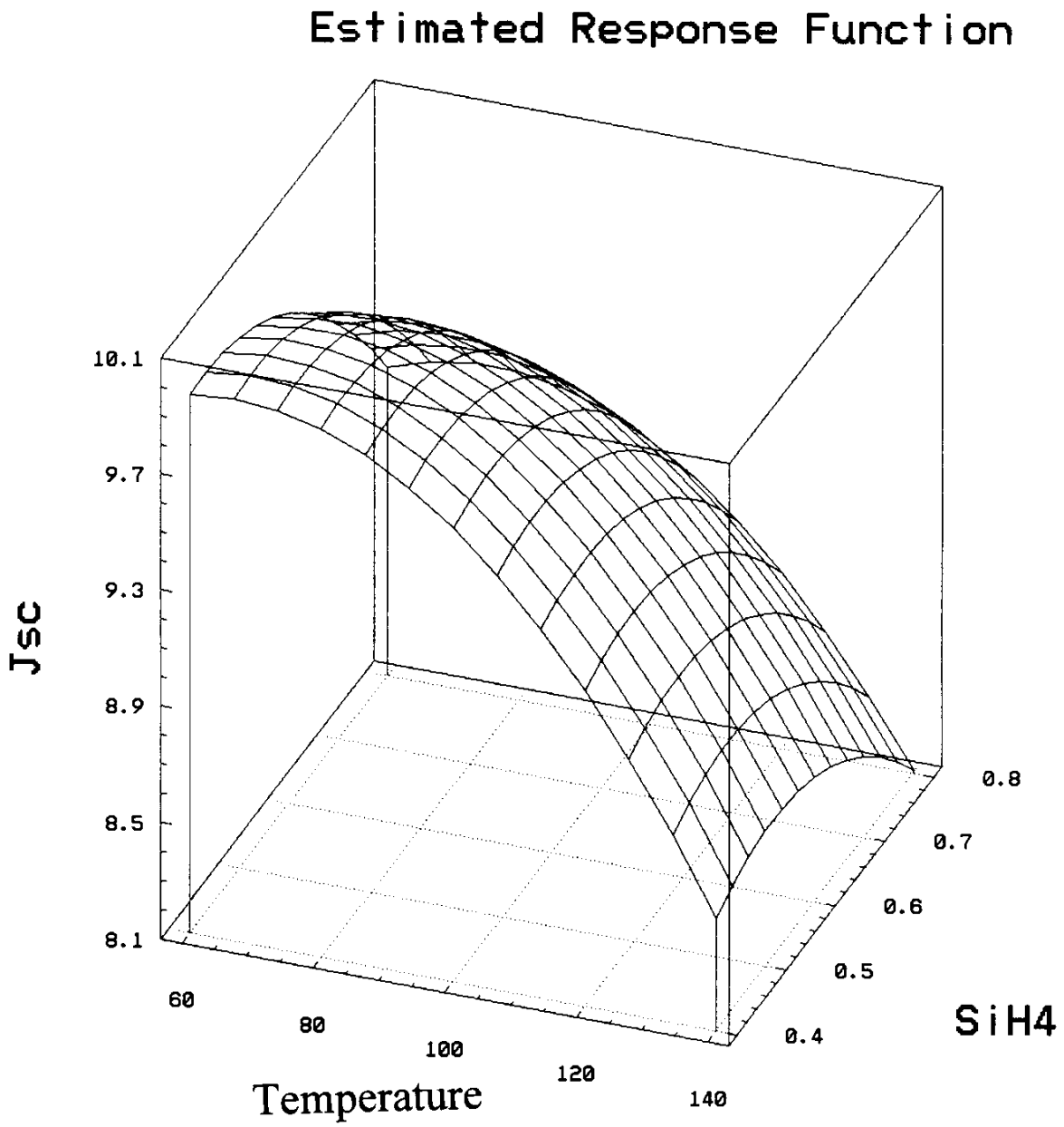

Figure 9-2 Response surface plot for J_{sc} as a function of SiH_4 and temperature while keeping the values of BF_3 and deposition time at the center values.

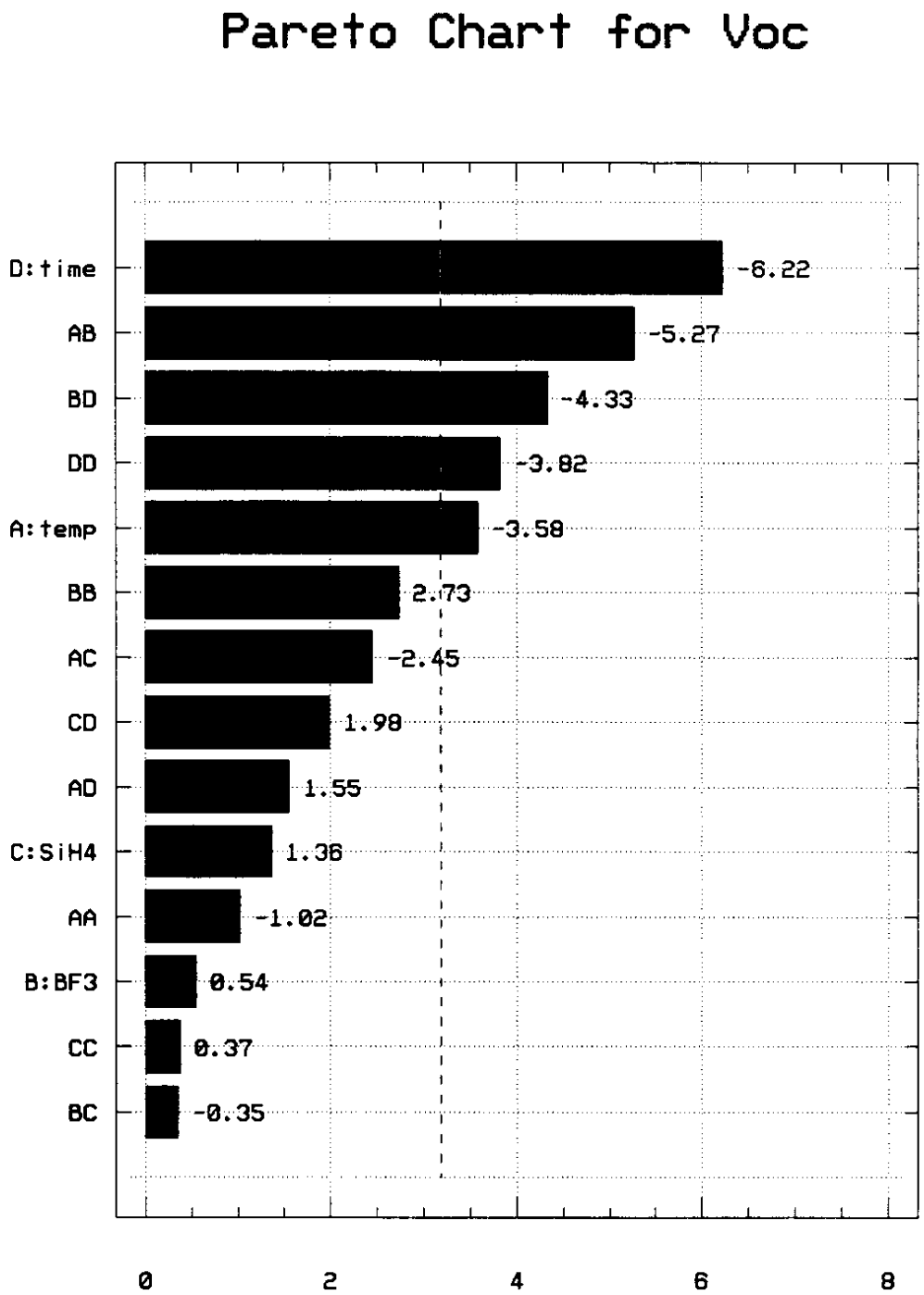

Figure 9–3 Pareto chart for V_{oc} of n-i-p solar cells with VHF μc-Si p-layer as a function of temperature, BF_3, SiH_4 and deposition time.

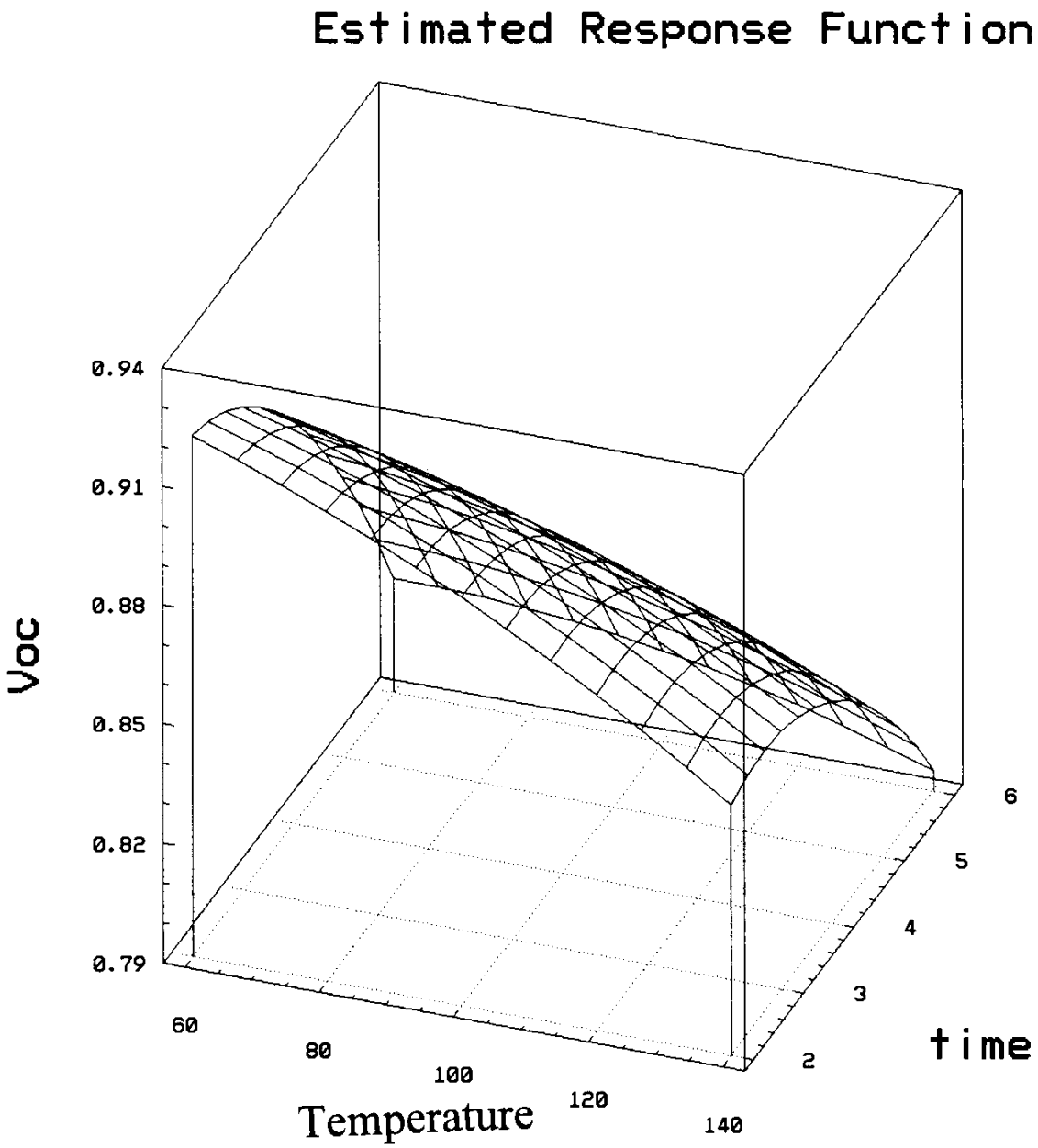

Figure 9-4 Response surface plot for V_{oc} as a function of deposition time and temperature while keeping the values of BF_3 and SiH_4 at the center values.

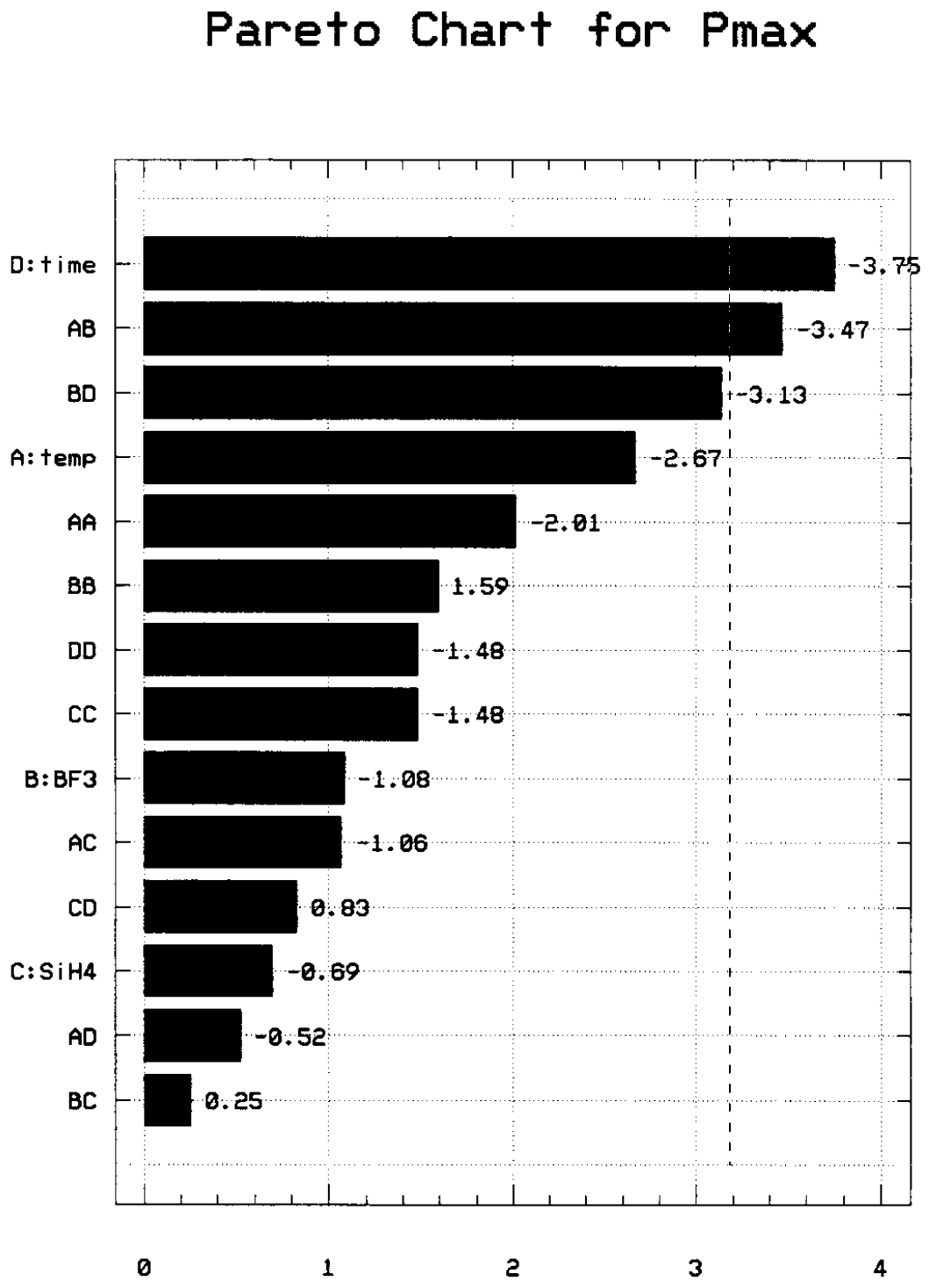

Figure 9-5 Pareto chart for P_{max} of n-i-p solar cells with VHF μc-Si p-layer as a fun of temperature, BF_3, SiH_4 and deposition time.

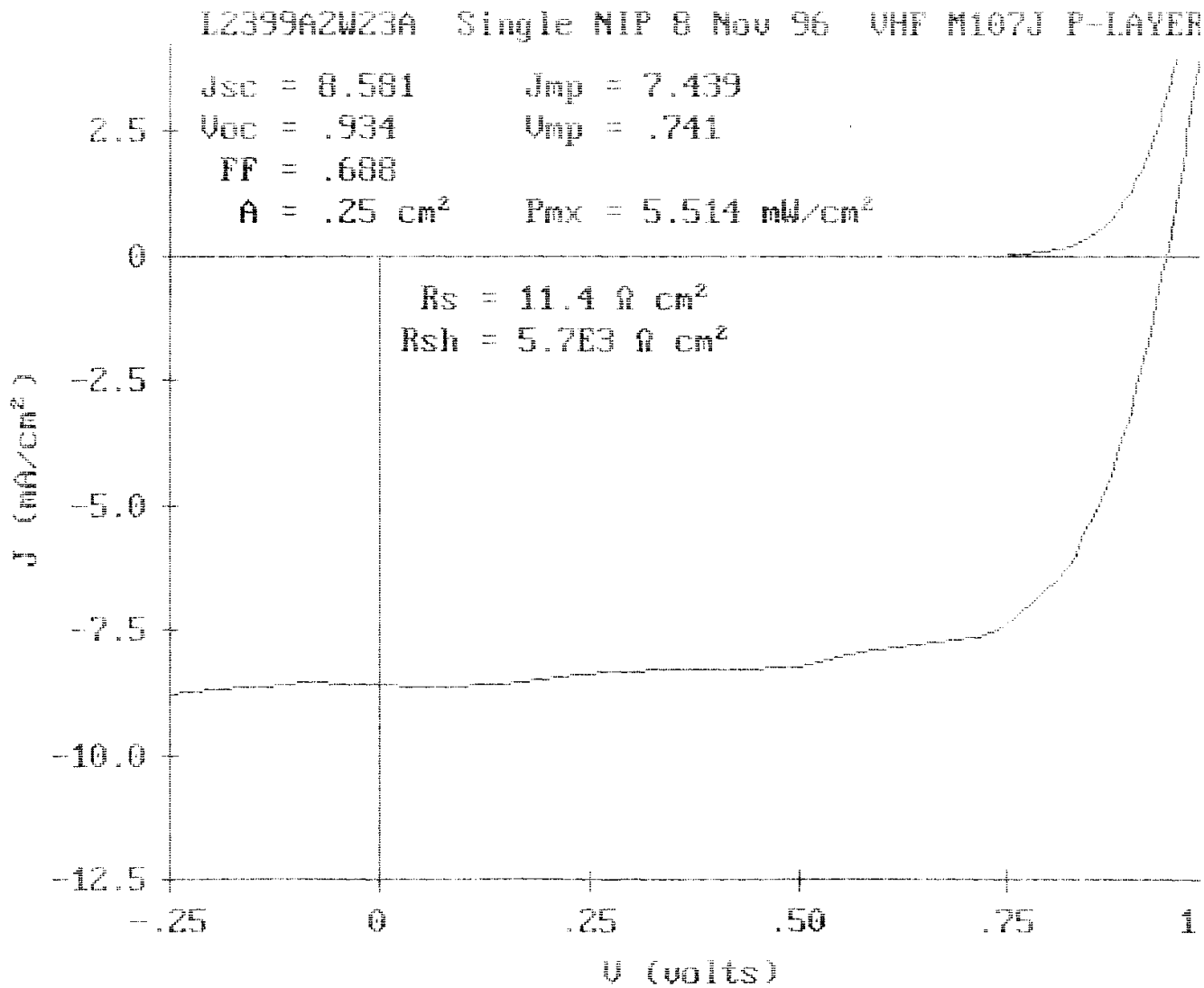

Figure 9-6 J-V curve for a representative device with VHF p-layer, showing a V_{oc} of 0.93 V.

Table 9-2 Results of solar cells whose p-layers were deposited using different processes: conventional RF, conventional VHF and a modified VHF process

p-layer	ITO	p process	Voc	Jsc	FF	Rs	Pmax	Jsc from QE	QE@400nm
Run No.	Run No.		(V)	(mA/cm2)		(Ohm,cm2)	(mW/cm2)	(mA/cm2)	(%)
L2523	4408	modified VHF	0.959	10.39	0.664	11.5	6.62	10.71	65.5
L2525	4408	conventional RF	0.948	9.82	0.63	14.8	5.86	10.09	59.1
L2526	4408	conventional VHF	0.933	8.78	0.651	12.2	5.33	10.04	56
L2527	4409	modified VHF	0.958	10.4	0.654	13.1	6.52	11.27	72.1

for the p-deposition. Each type of device is individually optimized for optimum performance. Besides the use of the same substrate, the ITO layer for these three devices are made in the same run (ITO4408) to ensure consistency. The data listed in Table 9-2 is the average of data for many small area solar cells on the same sample.

As we can see from these data, the device with p-layer deposited using the modified VHF process (Sample L2523) shows the highest performance. The V_{oc} and FF are the highest among the group. The largest amount of improvement is in J_{sc}, about 6% increase in J_{sc} compared with the conventional RF sample (L2525). To confirm the improvement in the modified VHF configuration, we repeated a modified VHF sample (L2527) with ITO coated in a separate evaporation (ITO4409). The improvement in the J_{sc} as well as V_{oc} and FF over the conventional RF sample was reproduced.

Figure 9-7 and 9-8 show the J-V curves for samples L2523 and L2525 corresponding to the modified VHF and the conventional RF p-layers. As a reminder, the results listed in Table 2-2 are averages of data for many cells on the same sample including those shown in Figure 9-7 and 9-8.

Figure 9-9 and 9-10 show the quantum efficiency curves for the modified VHF device (L2523) and the conventional RF device (L2525). The improvement in J_{sc} for the modified VHF device is mainly due to the 11% increase in the blue response. The lower absorption loss in the blue indicates that the modified VHF p-layer is more transparent to the sun light. The increased J_{sc} is indeed due to the improved transparency likely due to an increased microcrystallinity for this modified VHF p-layer.

We deposited a p-layer using the modified VHF process on a SS/Ag/ZnO/n-i structure prepared at United Solar to form a hybrid test device.[42] Figure 9-11 is the QE curve for such a device with a blue response of 83% at 400nm.

The improved microcrystallinity using VHF deposition process compared with conventional RF process is also supported by the RHEED measurement. Figure 9-12 shows a RHEED pattern of a device with VHF p-layer on the top. The sharp lines in the 220 and 311 rings and the dark background in between these rings indicate that the VHF p-layer is a microcrystalline material with high degree of microcrystallinity.

9.4 Summary

The use of the modified VHF p-layer in an a-Si solar cell increases the solar cell J_{sc}, V_{oc} and FF sizably. The increased J_{sc} and V_{oc} are most likely due to the improved microcrystalline formation in the p-layer. As an additional benefit, the new VHF process can be easily incorporated into a large scale production such as ECD's continuous roll-to-roll amorphous silicon PV production process.

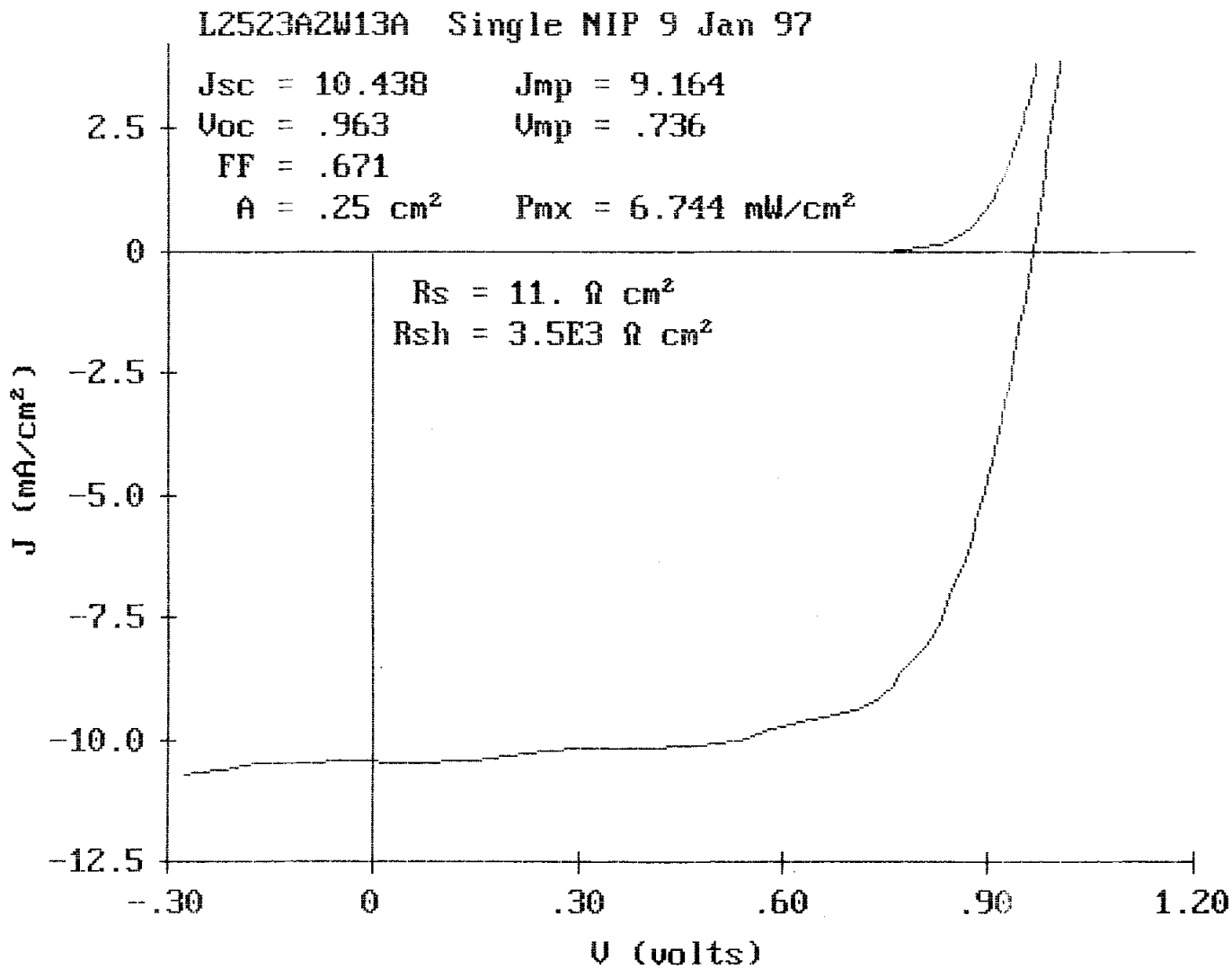

Room Voc = .764

Figure 9-7 J-V curve for an a-Si n-i-p device (Sample L2523) with p-layer deposited using the modified VHF PECVD.

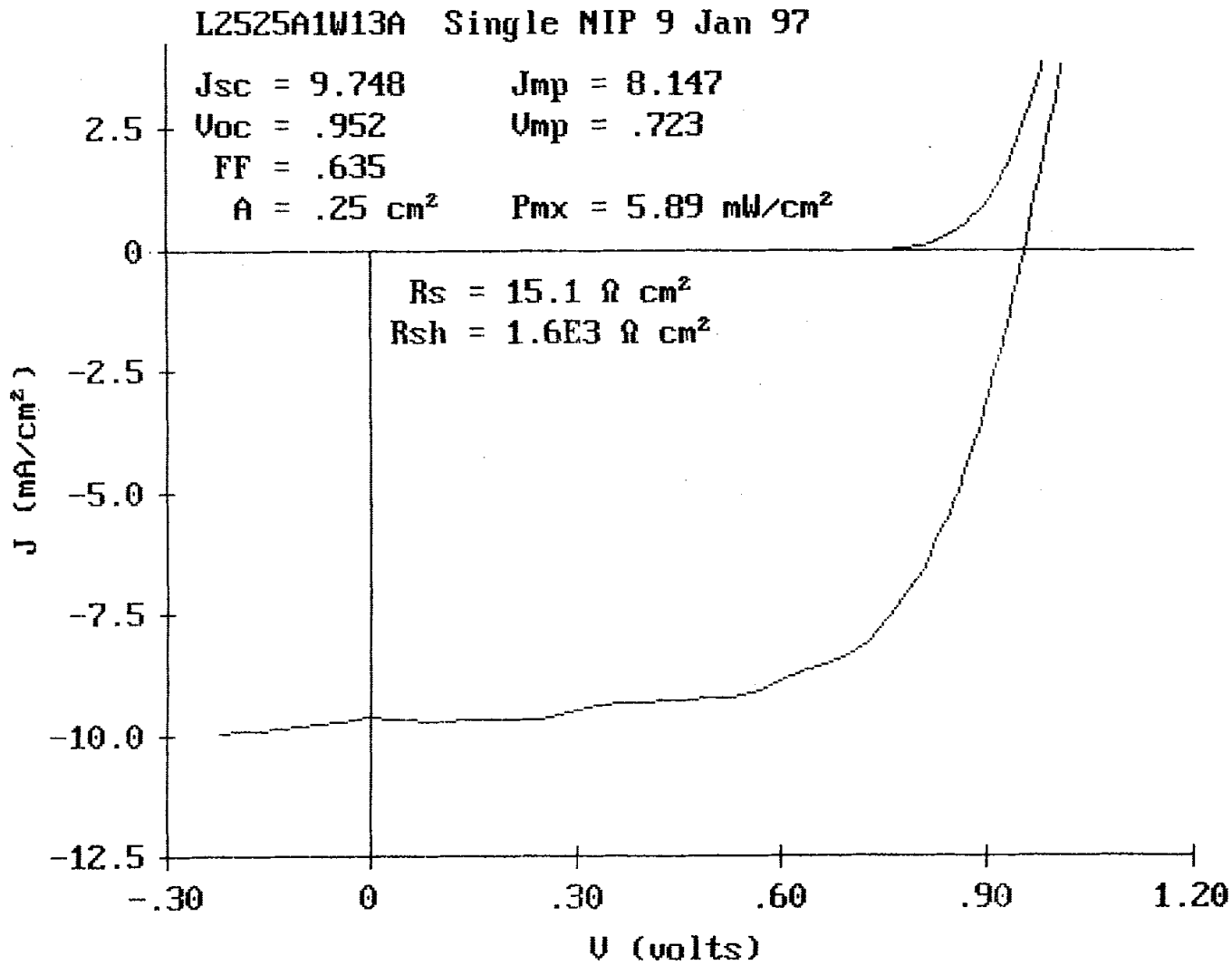

Figure 9-8 J-V curve for an a-Si n-i-p device (Sample L2525) with p-layer deposited using the conventional RF PECVD.

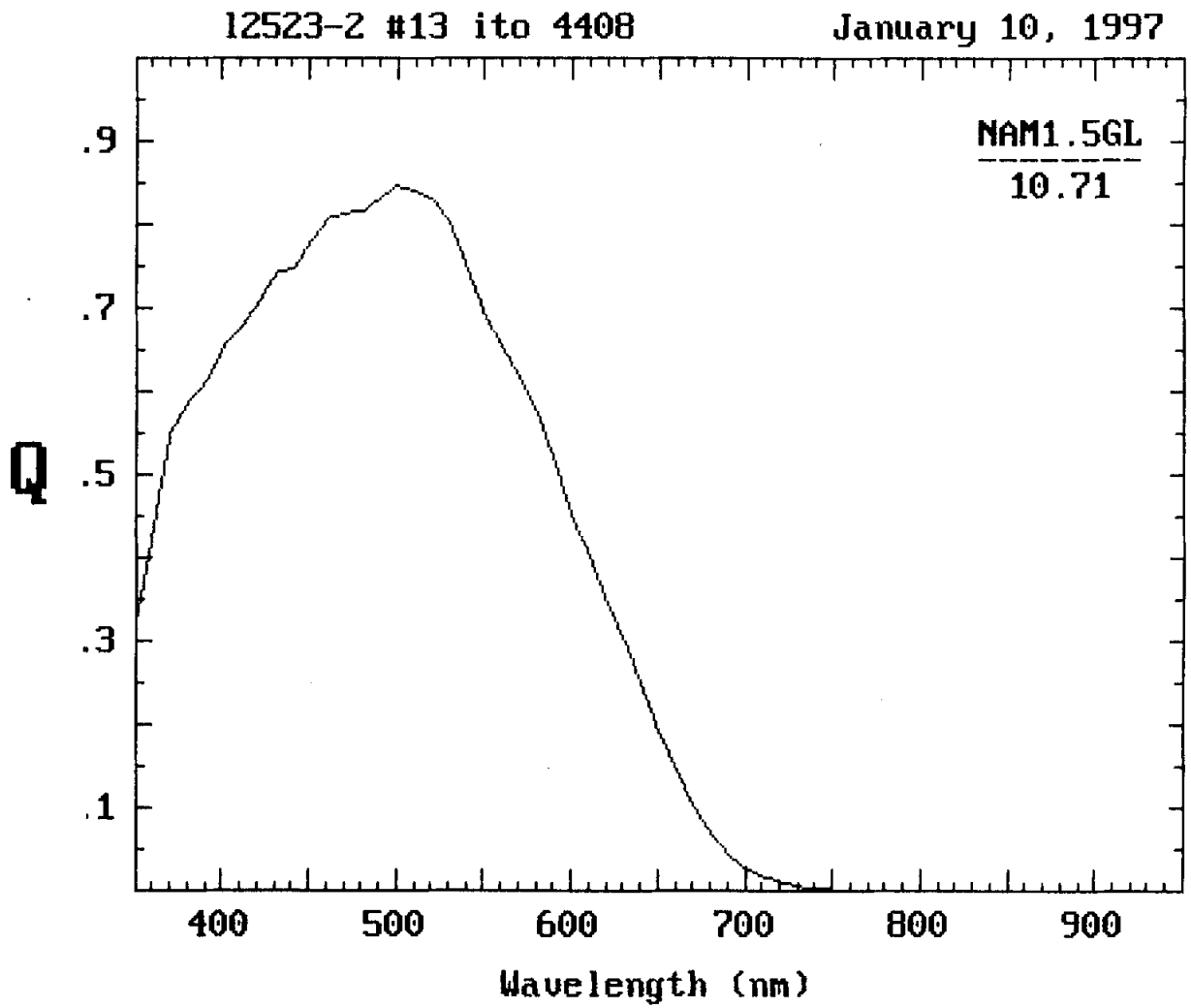

Figure 9-9 Quantum efficiency curve for an a-Si n-i-p device (Sample L2523) with p-layer deposited using the modified VHF PECVD, showing high blue response.

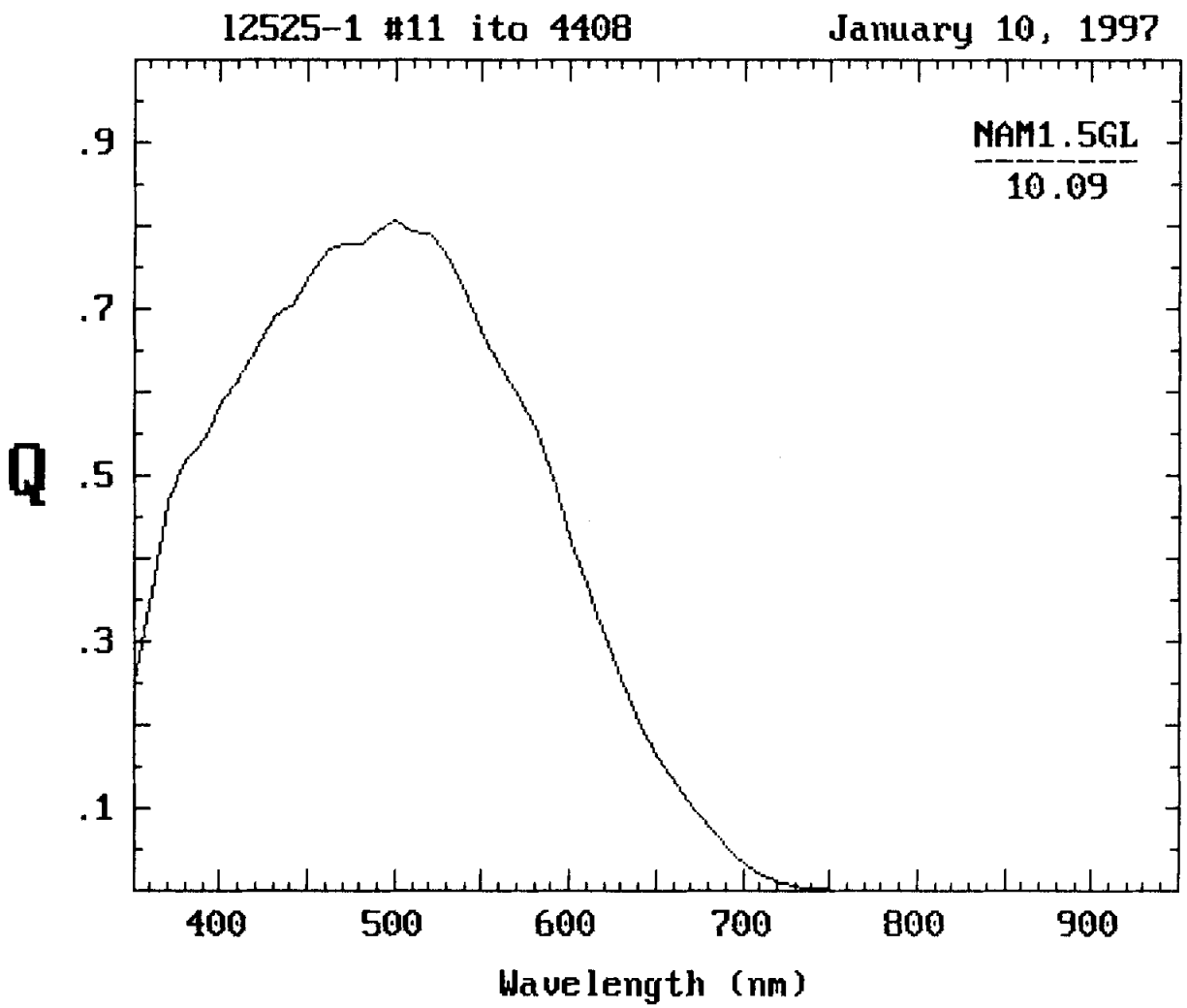

Figure 9-10 Quantum efficiency curve for an a-Si n-i-p device (Sample L2525) with p-layer deposited using the conventional RF PECVD.

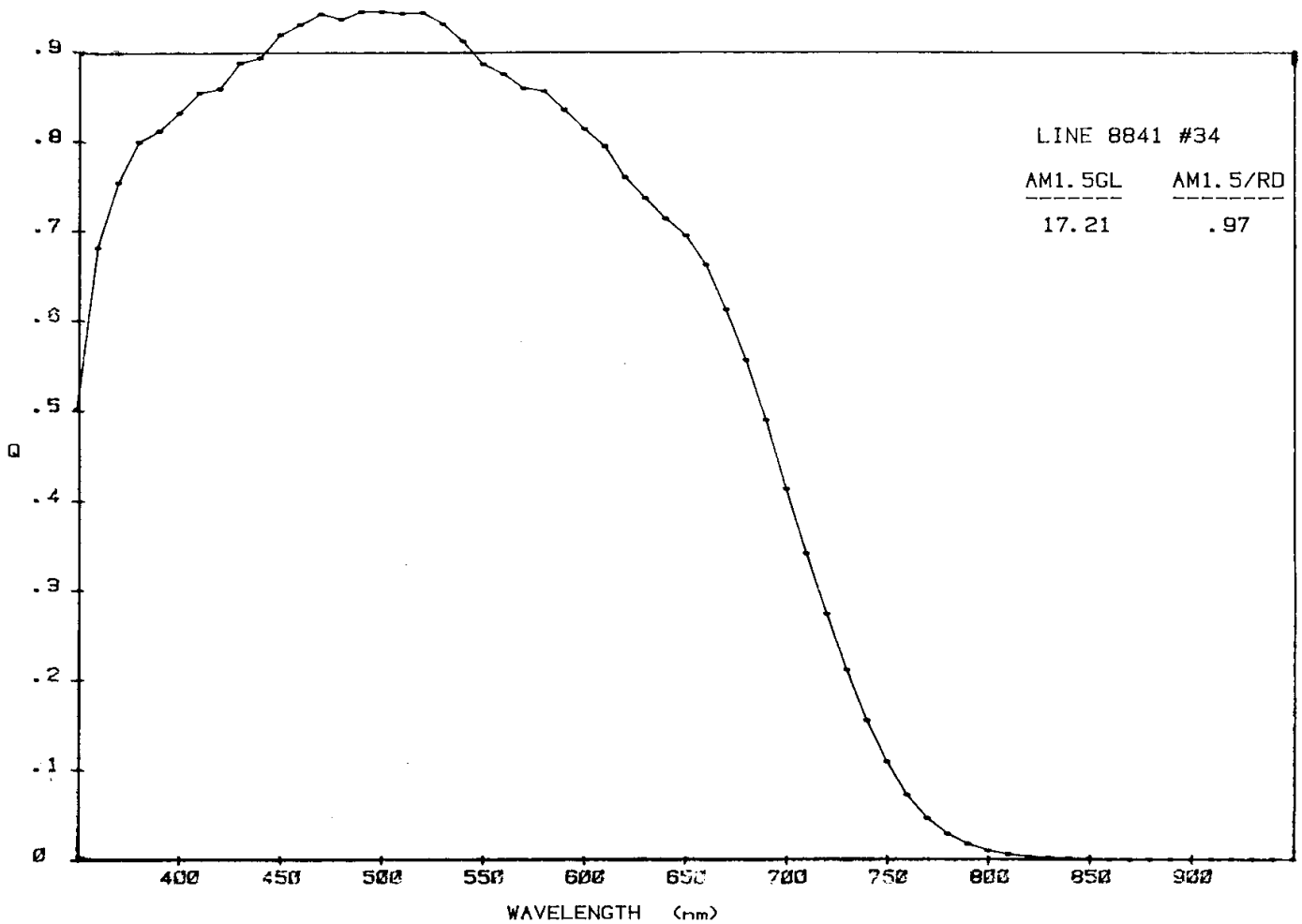

Figure 9-11 QE curve for an a-Si solar cell with ECD-deposited VHF p-layer and United Solar-deposited n-i layer on a SS/Ag/ZnO substrate, showing QE=83% at 400nm.

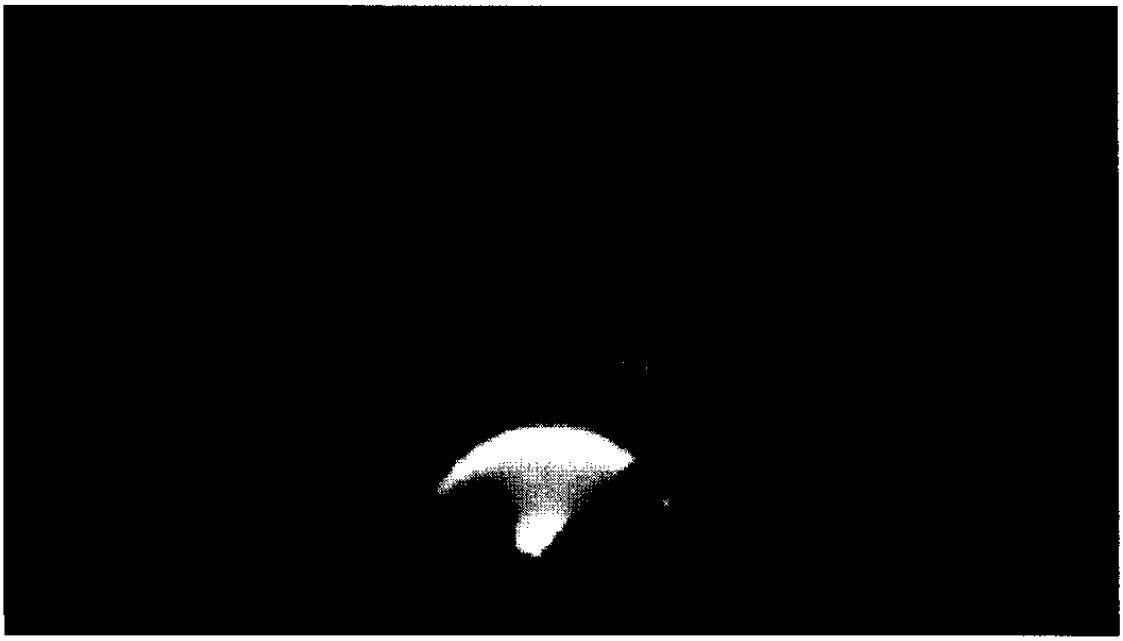

Figure 9-12 RHEED pattern for a device with a VHF p-layer as the top layer, Showing high volume fraction of microcrystalline phase in the p-layer.

Section 10
Optimization of Single-junction a-Si Solar Cell

10.1 Introduction

The optimization of single-junction a-Si n-i-p solar cell fabrication was performed in two solar cell deposition systems: LL1 and LL2. The main purpose of this optimization is to establish a good base line solar cell deposition.

10.2 Light Soaking of Single Cells with Different Thicknesses

We have produced, in the LL1 deposition system, a set of a-Si n-i-p solar cells with different i-layer thicknesses on bare SS substrate. Table 10-1 lists the J-V performance for this set of devices. After the initial measurement, this set of devices was soaked under one sun light for degradation evaluation. The temperature of these devices was measured at around 58 ^{o}C during light soaking. In Table 10-1, we also list the J-V data for all the devices after different light soaking steps. The degradation losses after 620 hours of light soaking are around 10%, 17% and 20% for devices with i-layer thicknesses of 1000Å, 3000Å, and 5000Å, respectively. The degradation occurred primarily during the first 100 hours of light soaking.

10.3 Reproducible and Consistent ITO Deposition

In our solar cell fabrication process, the top conducting electrodes (indium-tin-oxide, ITO) are deposited by evaporating an alloy of In and Sn in oxygen at elevated substrate temperature. To ensure effective a-Si solar cell research, it is extremely important to maintain the deposition of the ITO layer in an optimum and consistent condition. The crucial deposition conditions in the ITO evaporation include the substrate temperature, oxygen partial pressure, and the deposition thickness. For example, when the substrate temperature is too low, the deposited ITO film would include amorphous phase and, therefore, would not be as transparent as higher temperature deposited films. However, when the substrate temperature is too high during evaporation, an out diffusion of hydrogen would occur in the amorphous silicon semiconductor layers, which would cause a solar cell degradation. Since the ITO top electrode also serves as the anti-reflection coating for the device, the thickness of the ITO layer also needs to be carefully adjusted so that the reflection is minimized at the peak of $QE_xI_{1.5}$, where QE is the device quantum efficiency and $I_{1.5}$ is the AM1.5 global solar spectrum.

We have established a standard procedure to maintain the ITO evaporation under optimum conditions. A set of ITO runs are made routinely on a standard, uniform a-SiGe n-i-p solar cell produced in a roll-to-roll machine. Table 10-2 is a typical set of samples made for a routine check of the ITO deposition consistency, reproducibility, and optimum quality. In the table, each row represents the average of the device performance for all the cells (typical 8 to 16) in a 2” x 2” sample. The two positions represent samples placed at two sides of the substrate, therefore, indicating the uniformity within the same ITO run. Int. Q in the table is the short circuit current as calculated by integrating the QE response over AM1.5 global spectrum. Q_{400} is the QE at 400

Table 10-1. Device performance of single-junction a-Si n-i-p solar cells deposited on bare SS with different i-layer thicknesses, after different light soaking times.

Sample No.	i-layer thickness	light-soaking hours	Cell #	V_{oc}	J_{sc}	FF	Efficiency	Drop in Efficiency
	(Å)	(h)		(V)	(mA/cm^2)		(%)	(%)
1	5000	0	33	959	12.19	.524	6.13	---
		120	33	921	10.37	.527	5.04	18.0
		380	33	914	10.30	.523	4.92	20.0
		620	22	914	9.80	.520	4.68	20.0*
2	4000	0	23	939	10.70	.510	5.12	---
		120	23	919	9.40	.511	4.41	14.0
		380	23	913	9.22	.509	4.28	16.5
		620	23	.912	9.24	.506	4.27	16.6
3	3000	0	32	.951	10.86	.601	6.21	---
		120	32	.917	10.20	.553	5.17	16.8
		380	32	.916	10.29	.554	5.22	16.8
		620	31	910	10.38	.550	5.20	16.6*
4	1000	0	23		7.58	.716	5.24	---
		120	23		7.49	.685	4.74	9.5
		380	ALL	SHUNTED				

* Different cells of the same sample.

Table 10-2 Performance of reference solar cells coated with different ITO in a routine check of the ITO deposition consistency and reproducibility.

ITO run #	position	Ts	Relat. Thick	O2 pressure	Voc	Jsc	FF	Rs	Pmax	Int. Q	Q400	Qmax
		(C)	(A)	(0.1 mTorr)	(V)	(mA/cm2)			(mW/cm2)	(mA/cm2)		
4455	1	220	1400	5.1	0.653	13.88	0.627	7.9	5.68	15.41	0.618	0.869
	2	220	1400	5.1	0.657	14.44	0.63	7.5	5.98			
4477	1	235	1400	5.1	All shorted							
	2	235	1400	5.1	0.661	15.05	0.628	7.7	6.25	15.54	0.595	0.878
4478	1	235	1400	5.1	0.67	14.86	0.624	8.4	6.21	15.38	0.632	0.874
	2	235	1400	5.1	0.671	15.17	0.61	9	6.2			
4459	1	205	1400	5.1	0.65	13.51	0.635	7.8	5.57			
	2	205	1400	5.1	0.653	13.85	0.63	8	5.71	14.92	0.527	0.828
4460	1	220	1600	5.1	0.66	13.37	0.644	7.6	5.69			
	2	220	1600	5.1	0.661	13.61	0.623	8.7	5.6			
4461	1	220	1400	7.4	0.659	14.24	0.609	9.3	5.72			
	2	220	1400	7.4	0.663	14.44	0.614	9.1	5.88	15.43	0.646	0.872
4462	1	220	1400	3.5	0.654	12.66	0.638	8.2	5.29			
	2	220	1400	3.5	0.653	12.36	0.639	8.3	5.16	13.77	0.479	0.766
4468	1	220	1250	5.2	0.662	14.88	0.638	7.1	6.28	15.83	0.687	0.902
	2	220	1250	5.2	0.662	14.25	0.641	7.3	6.04			
4469	1	220	1550	5.1	0.663	14	0.647	6.7	6.01			
	2	220	1550	5.1	0.66	14.14	0.644	6.8	6.01	15	0.535	0.846
4470	1	220	1400	5.1	0.652	13.55	0.635	7.7	5.61			
	2	220	1400	5.1	0.657	14.35	0.628	7.8	5.92			
4471	1	220	1600	7.5	0.658	14.46	0.624	8.4	5.94			
	2	220	1600	7.5	0.66	14.47	0.62	8.6	5.92	15.64	0.617	0.884
4472	1	220	1200	3.5	0.656	13.11	0.625	9	5.37	13.84	0.617	0.784
	2	220	1200	3.5	0.659	13.22	0.624	8.8	5.43			

nm, indicating the blue response. Q_{max} is the maximum QE value in the spectrum, which reflects the ITO absorption and the effect of anti-reflective coating.

Sample ITO4455 was deposited under the standard condition that we previously established. The purpose of this group of samples is to see whether this deposition condition still remains optimum and how sensitive the solar cell performance depends on the variation of each deposition parameter. Sample ITO4470 was deposited under the identical condition as ITO4455. The very similar performance of these two samples demonstrates the level of reproducibility of the system.

Comparing ITO4478 and ITO4459 with ITO4455, a decrease in the deposition temperature results in a loss in J_{sc}, up to 3.4%. This is because at 205˚C, there is an increase in the fraction of amorphous phase in the ITO and, therefore, the absorption is increased.

In terms of the ITO thickness, a 10% variation on both sides does not show a significant change in the P_{max}. Comparing ITO4469 with ITO4468, the thicker ITO caused a small loss in J_{sc} and a small gain in FF due to the reduced sheet resistance, resulting in no significant changes in P_{max}.

Comparing samples ITO4461 (with higher oxygen pressure) and ITO4462 (with lower oxygen pressure) with the standard sample ITO4455, higher oxygen pressure increases J_{sc}. This is mainly due to a higher oxygen incorporation in the alloy which reduces the oxygen deficiency and, hence, the free carrier absorption. However, when the amount of free carriers is reduced, the resistivity of the ITO increases, as we see from the increase in series resistance and the decrease in fill factor in Sample ITO4461. Also, with the increase in the oxygen pressure, the ITO thickness could decrease. This could be a real change in the ITO thickness or a change in the calibration factor for the thickness monitor. The overall power output P_{max} of the test cell is reduced for higher oxygen pressure due to the relatively larger loss in FF and smaller gain in J_{sc}, compared with the standard sample. When the oxygen pressure is reduced from the standard value during the evaporation, as we see for sample ITO4462, there is a sizable loss in J_{sc} as expected, yet no gain was observed in the FF, resulting a net loss in the P_{max}. Figures 10-1 and 10-2 show the QE curves of ITO4461 and ITO4462 with different oxygen pressures during evaporation. Sample ITO4461 shows much higher ITO transmission, suggesting a reduced oxygen deficiency in the oxide.

The loss in P_{max} for difference oxygen pressure can be somewhat compensated with a thickness adjustment, as can be seen by comparing data for Samples ITO4471 and ITO4472 with those for Samples ITO4461 and ITO4462. For the ITO deposition at higher oxygen pressure, increased thickness compensates the loss in FF (See ITO4471). However, for the sample deposited with low oxygen pressure, reduced thickness does not fully recover the loss in J_{sc} (See ITO4472).

This set of test samples with various ITO evaporation conditions ensures that the ITO is deposited under optimum conditions. The consistent and reproducible ITO deposition is extremely important to the solar cell device research.

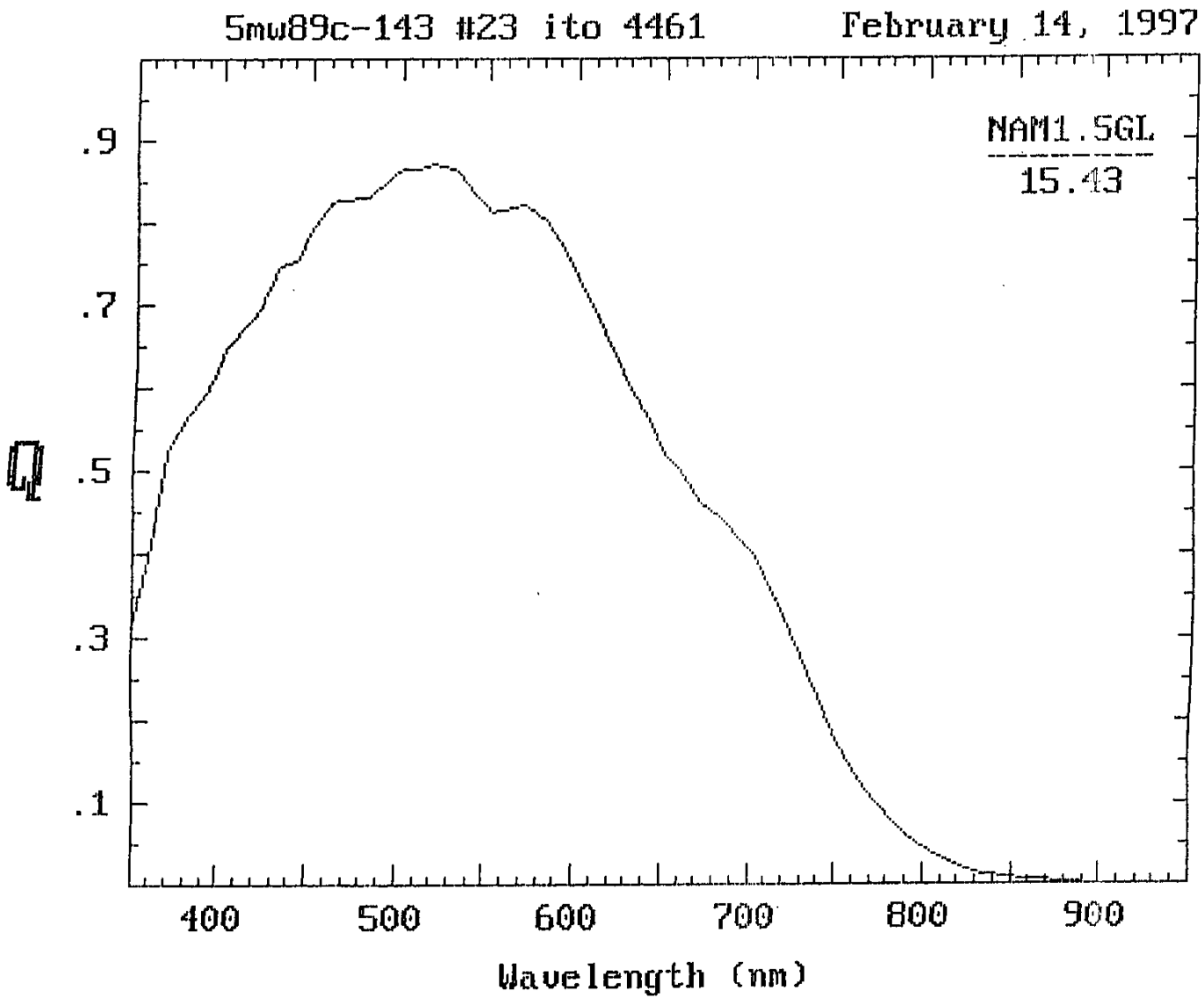

Figure 10-1 Quantum efficiency spectrum for cell whose ITO was made using a high oxygen pressure.

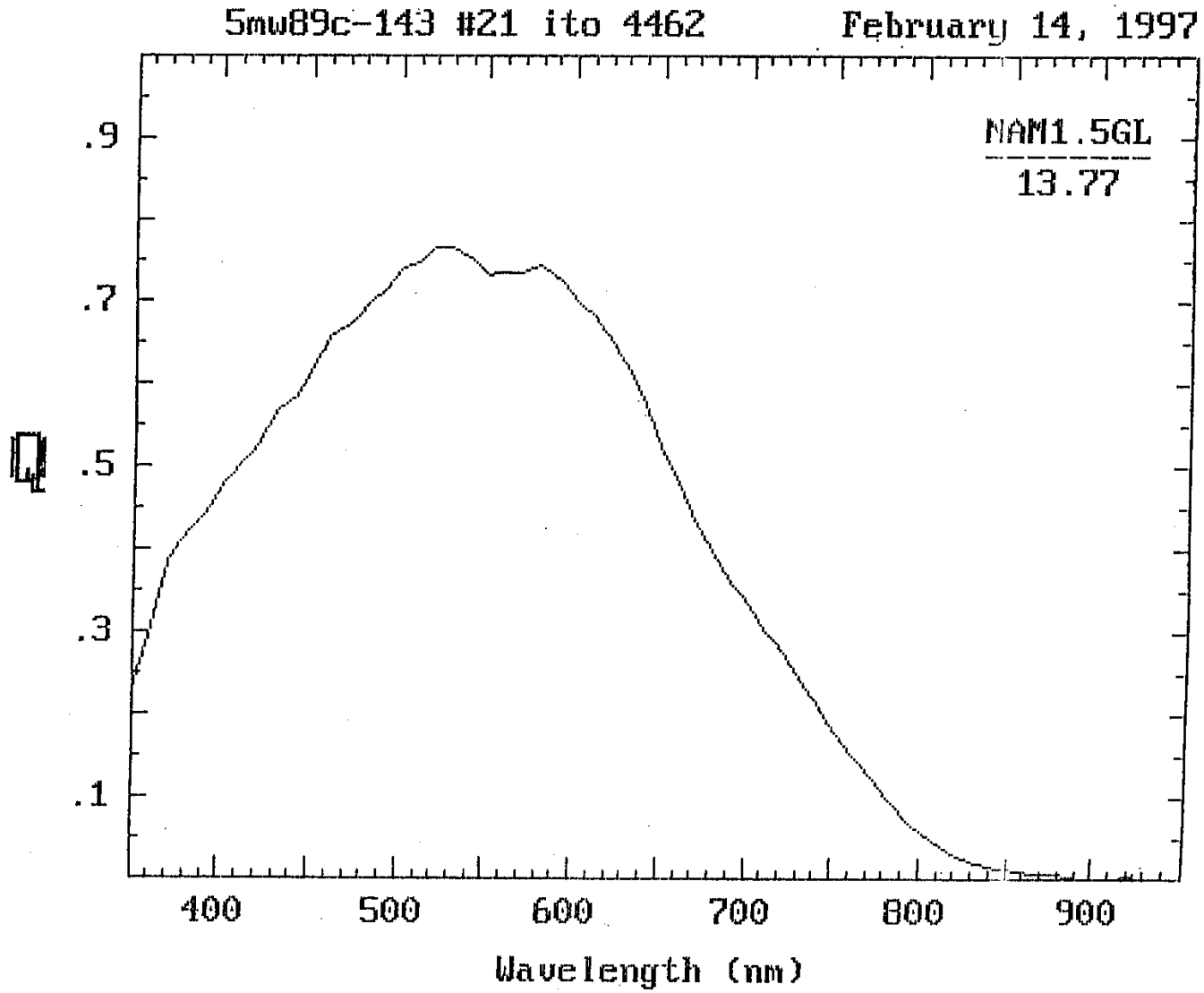

Figure 10-2 Quantum efficiency spectrum for cell whose ITO was made using a low oxygen pressure.

10.4 Optimizing Single Cell Efficiency and Baseline Performance

Single junction n-i-p solar cells were produced in our deposition systems. We maintain a baseline for fabrication of single-junction solar cells with 10.6% initial efficiency. Figure 10-3 shows the J-V characteristics with a V_{oc} of 0.944 V, J_{sc} of 16.4 mA/cm^2 and FF of 0.687. Figure 10-4 shows the J-V curves measured under weak blue and red light.

10.5 Summary

The deposition of single-junction a-Si solar cells have been optimized in both small area solar cell deposition systems at ECD. Solar cells with different i-layer thicknesses were studied and their light soaking degradation have been tested. We have improved the deposition of a-Si n-i-p solar cells and obtained baseline single-junction a-Si solar cell with 10.6% initial efficiency. The deposition of high performance single cells in this system has been demonstrated to be reproducible and consistent after process optimization.

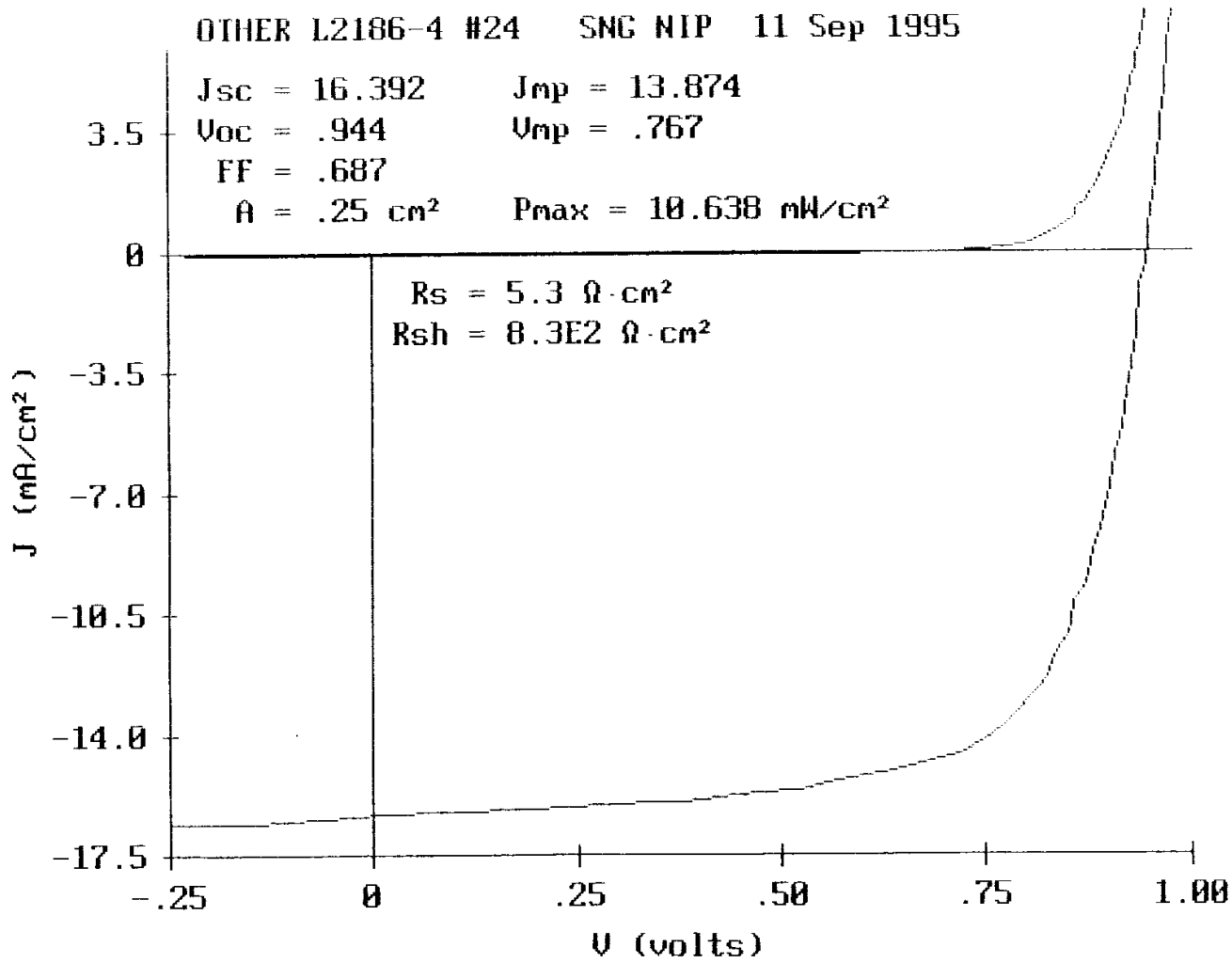

Figure 10-3 J-V curve of an optimized single-junction a-Si solar cell, showing 10.6% initial efficiency.

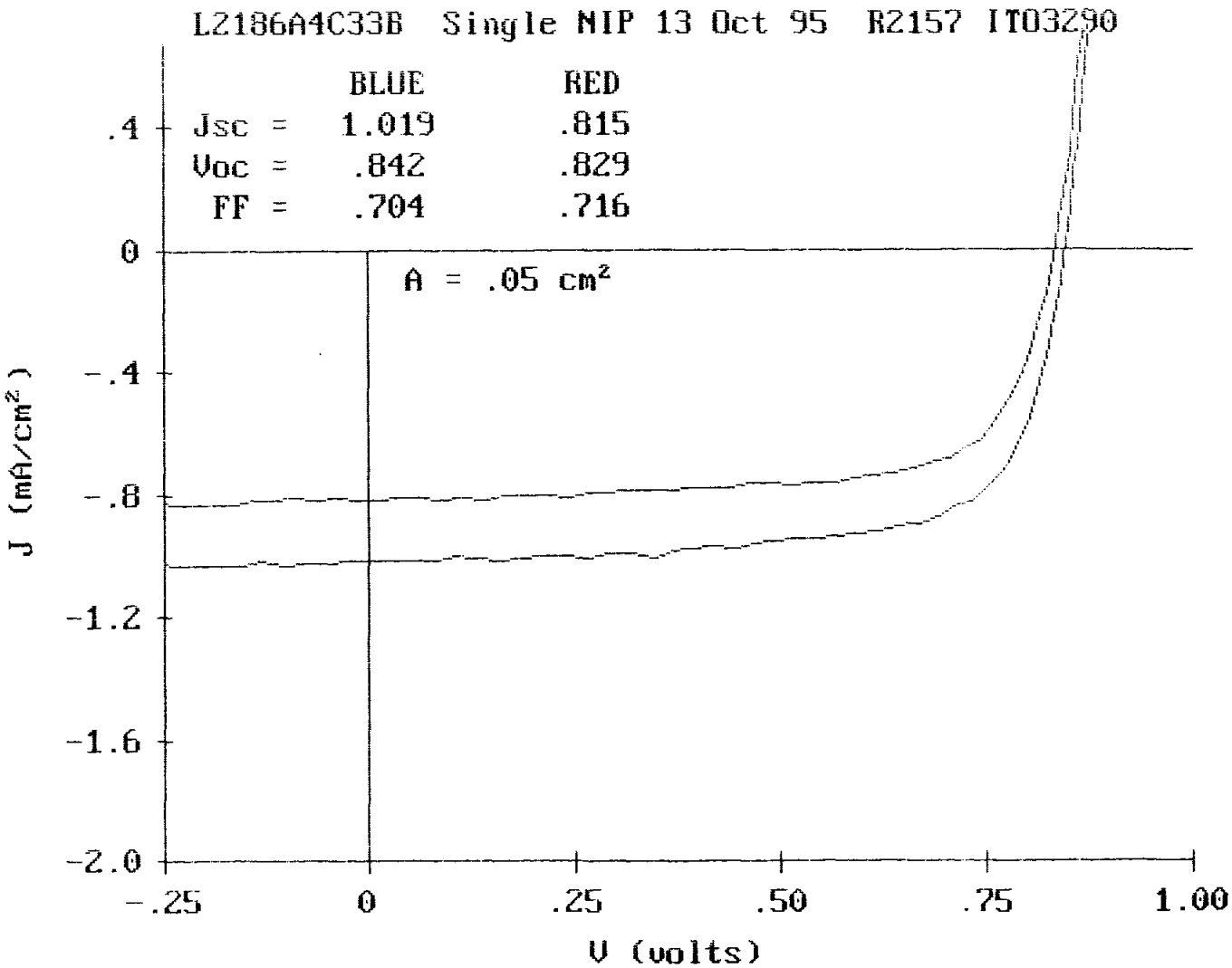

Figure 10-4 J-V curve of an optimized single-junction a-Si solar cell measured under weak blue and red lights.

Section 11
Optimization of Tunnel Junction

11.1 Introduction

In the triple-junction a-Si alloy solar cell structure, there are two tunnel junctions: one between the p-layer of the bottom cell and the n-layer of the middle cell, and the other between the p-layer of the middle cell and the n-layer of the top cell. The high density of defect states induced from heavy doping in the tunnel-junction doped layers results in heavy recombination of the collected carriers from both nearby component cells. In this way, no reverse voltage will be formed and the resistance from the tunnel junction can be minimized.

ECD uses a proprietary microcrystalline p-layer in the a-Si n-i-p solar cell device. This p-layer provides high V_{oc} due to the wider bandgap, provides low activation energy, high transmission due to the wider bandgap, and provides better fill factor due to the low resistivity and a high built-in field.

In ECD's solar cell design, the tunnel junction is formed between μc-Si p^+ layer and the a-Si n^+ layer. The μc-Si p^+ layer offers advantages over its amorphous counterpart as the tunnel-junction p-layer due to its higher density of recombination states near the grain boundary. We have performed a study to optimize and improve the tunnel-junction performance.

11.2 Optimization of Tunnel Junctions

The series resistances of the triple-junction cells deposited in the LL2 system installed during Phase I were initially high, which was mainly due to the poor tunnel junctions between component cells. Efforts were made to improve the tunnel junctions are described below.

The p-layer deposition condition plays a crucial role in determining the tunnel-junction performance. Figure 11-1a though 11-1d show the J-V curves for four n-i-p-n solar cells (L2157 through L2160) with the p-layer deposited at different temperatures. From this group of samples, we find that the p-layer deposited at 120 ^oC is most suitable for the tunnel-junction p-layer since it provides the lowest R_s and highest V_{oc}. We then studied the dependence of tunnel-junction performance on the p-layer thickness. Figure 11-2 is the J-V curve for an n-i-p-n device with a p-layer deposited for 4 min, which is half of the time for the other four samples. The V_{oc} was improved to 0.88 V and the R_s was reduced to 15 Ωcm^2 by thinning the p-layer. By reducing the n-layer thickness to half, we have further reduced R_s down to 10 Ωcm^2 and improved the V_{oc} up to 0.89 V, as is shown in Figure 11-3. Table 11-1 summarizes the deposition conditions and V_{oc} and R_s for these six n-i-p-n samples.

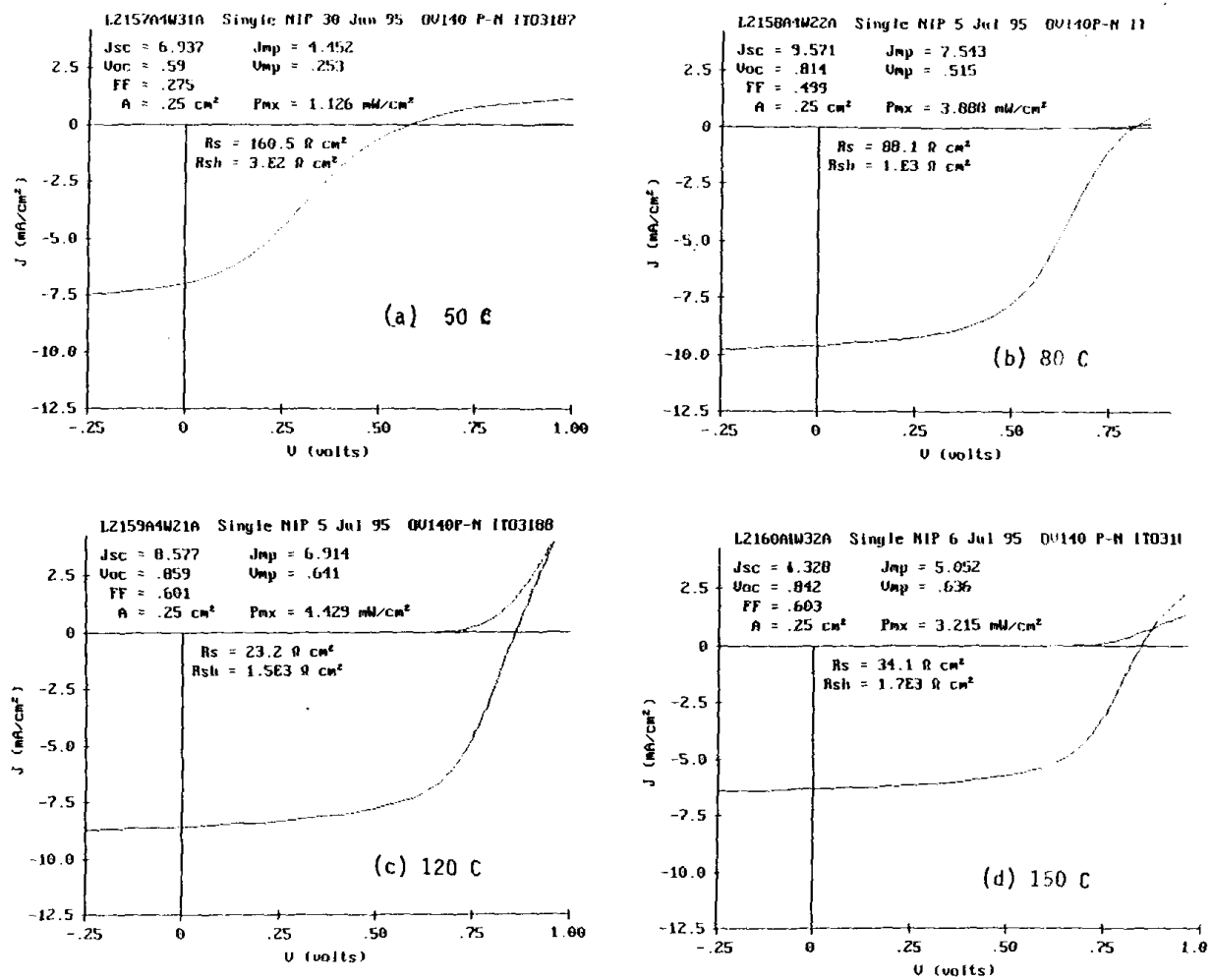

Figure 11-1 J-V curve of a-Si n-i-p-n tunnel-junction test device with p-layer deposited at different temperatures: (a) 50 °C; (b) 80 °C; (c) 120 °C; and (d) 150 °C.

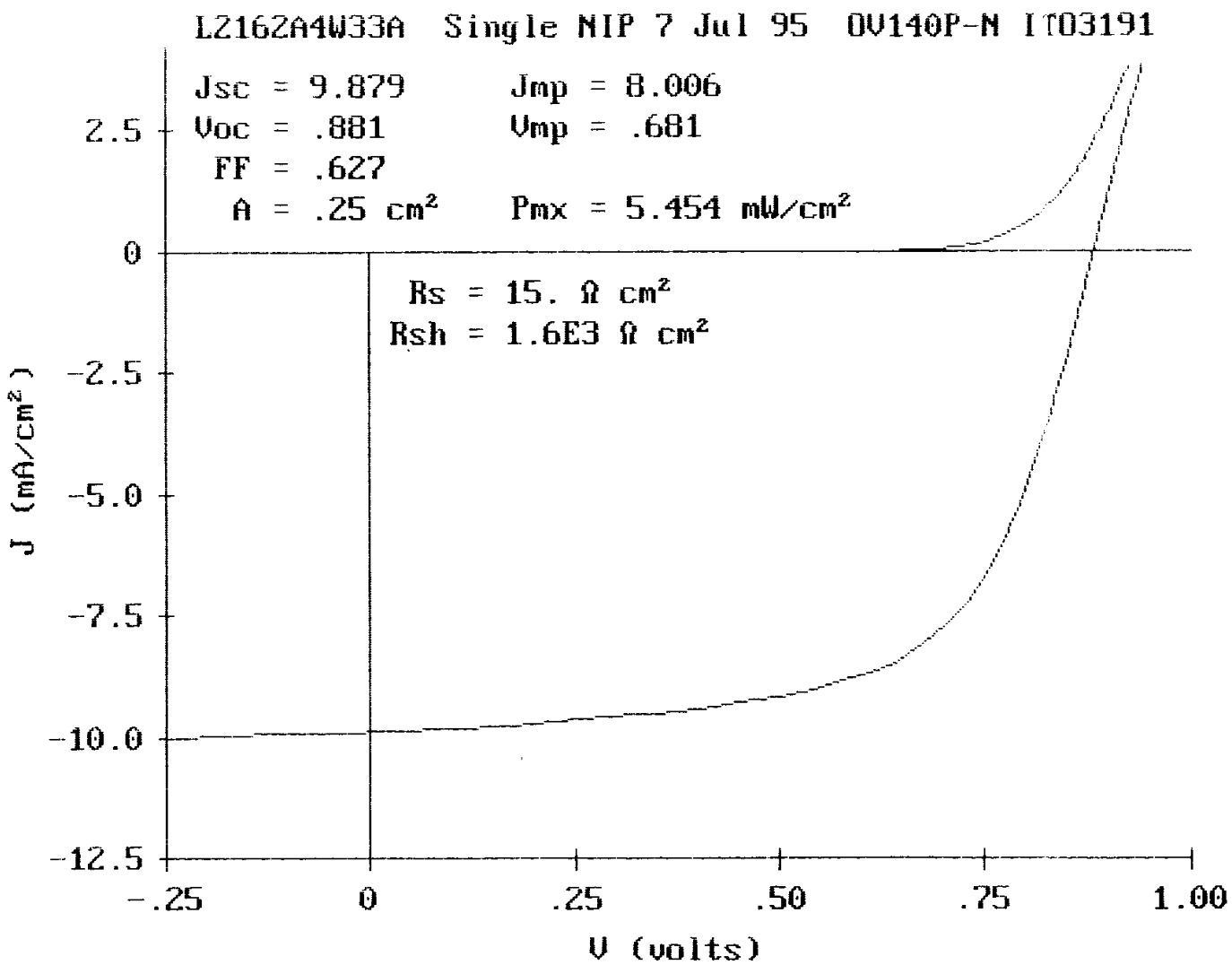

Figure 11-2 J-V curve of a-Si n-i-p-n device with thinner p-layer compared to that shown in Figure 11-1.

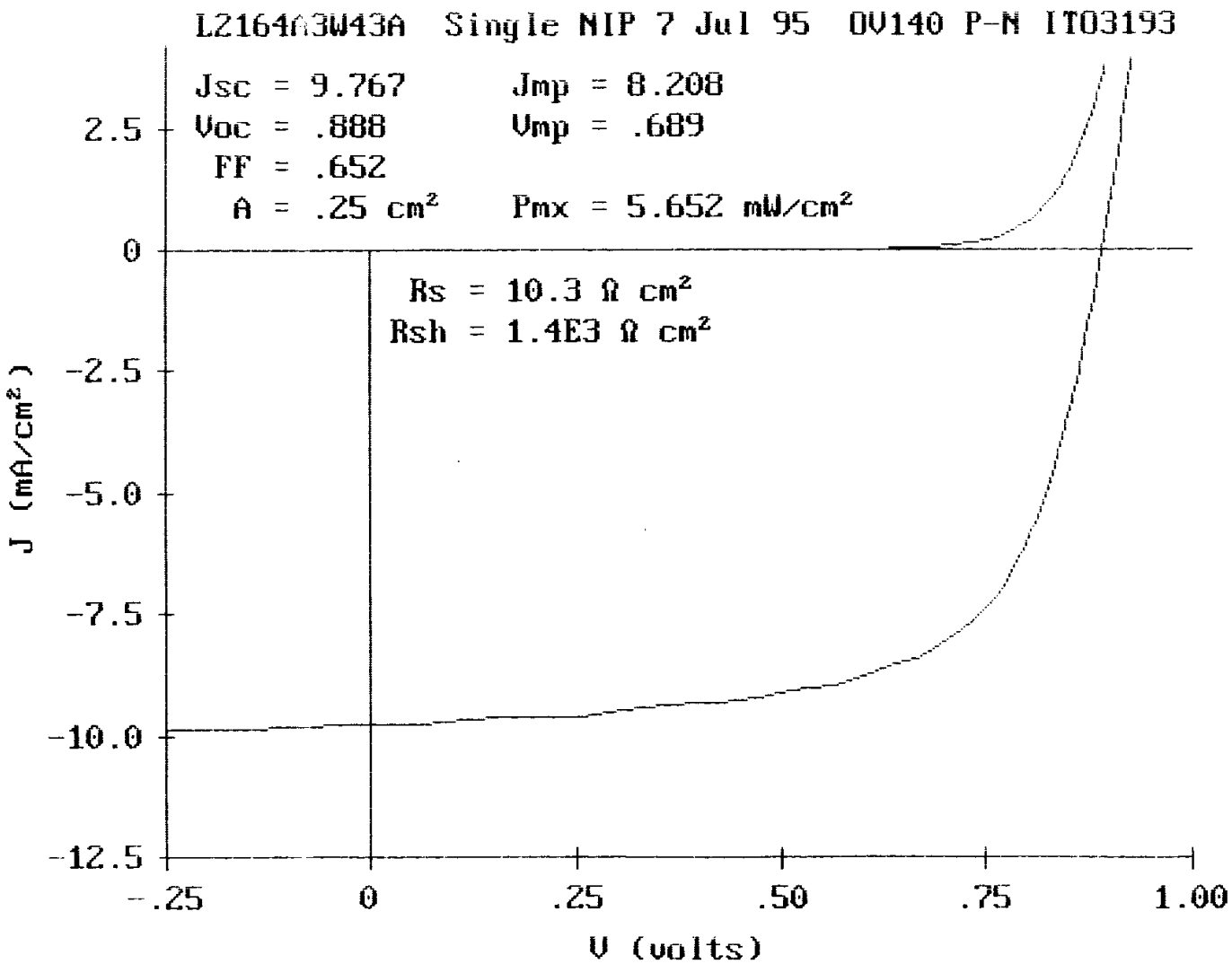

Figure 11-3 J-V curve of a-Si n-i-p-n device with thinner n-layer compared to that shown in Figure 11-2.

Table 11-1 Performance of n-i-p-n devices with different p- and n-layer deposition temperatures and thicknesses.

Device No.	Temp (p) (^oC)	Time (p) (min)	Temp (n) (^oC)	Time (n) (min)	V_{oc} (V)	R_s (Ωcm^2)
L2157	50	8	250	2	0.59	160
L2158	80	8	250	2	0.81	88
L2159	120	8	250	2	0.86	23
L2160	150	8	250	2	0.84	34
L2162	120	4	250	2	0.88	15
L2164	120	4	250	1	0.89	10

We then incorporated the improved tunnel junction into the triple-junction solar cell. Four triple-junction cells were deposited under identical conditions except for the n-layer thickness. Table 11-2 summarizes the n-layer deposition times and the triple-junction device performance. The 1 min n-layer deposition did result in a lower R_s as in L2164. However, the V_{oc} dropped from 2.20 V to 1.96 V when the n-layer deposition time was reduced from 2.0 min to 1.0 min. The thin n-layer deposited in 1 min is not sufficient to provide a high V_{oc} for the n-i-p junction. The test device n-i-p-n is not effective to reveal this shortcoming. From Table 11-2, we find that a 1.5 min deposition time for the tunnel-junction n-layers (n2 and n3) provides both a reasonably high V_{oc} (2.20 V) and a low R_s (49 Ωcm^2).

Table 11-2 Device performance of triple-junction a-Si/a-SiGe/a-SiGe solar cells with different tunnel-junction n-layer thicknesses.

Run#	n_1-layer dep. time (min)	n_2-layer dep. time (min)	n_3-layer dep. Time (min)	Voc (V)	J_{sc} (mA/cm^2)	FF	R_s (Ωcm^2)	Eff
L2166	2.0	1.5	1.5	2.203	6.55	0.623	49.4	9.00
L2167	1.0	1.0	1.0	1.959	6.35	0.641	44.1	7.97
L2168	2.0	1.5	2.0	2.172	6.59	0.637	52.8	9.12
L2169	2.0	2.0	2.0	2.174	6.17	0.682	95.4	9.14

To check the performance of the tunnel junction with a 1.5-min thick n-layer, we have deposited an a-Si/a-Si tandem device using the optimized tunnel-junction deposition condition, with the J-V data shown in Figure 11-4. This tandem-junction cell (L2200) shows high V_{oc} , low R_s and high FF.

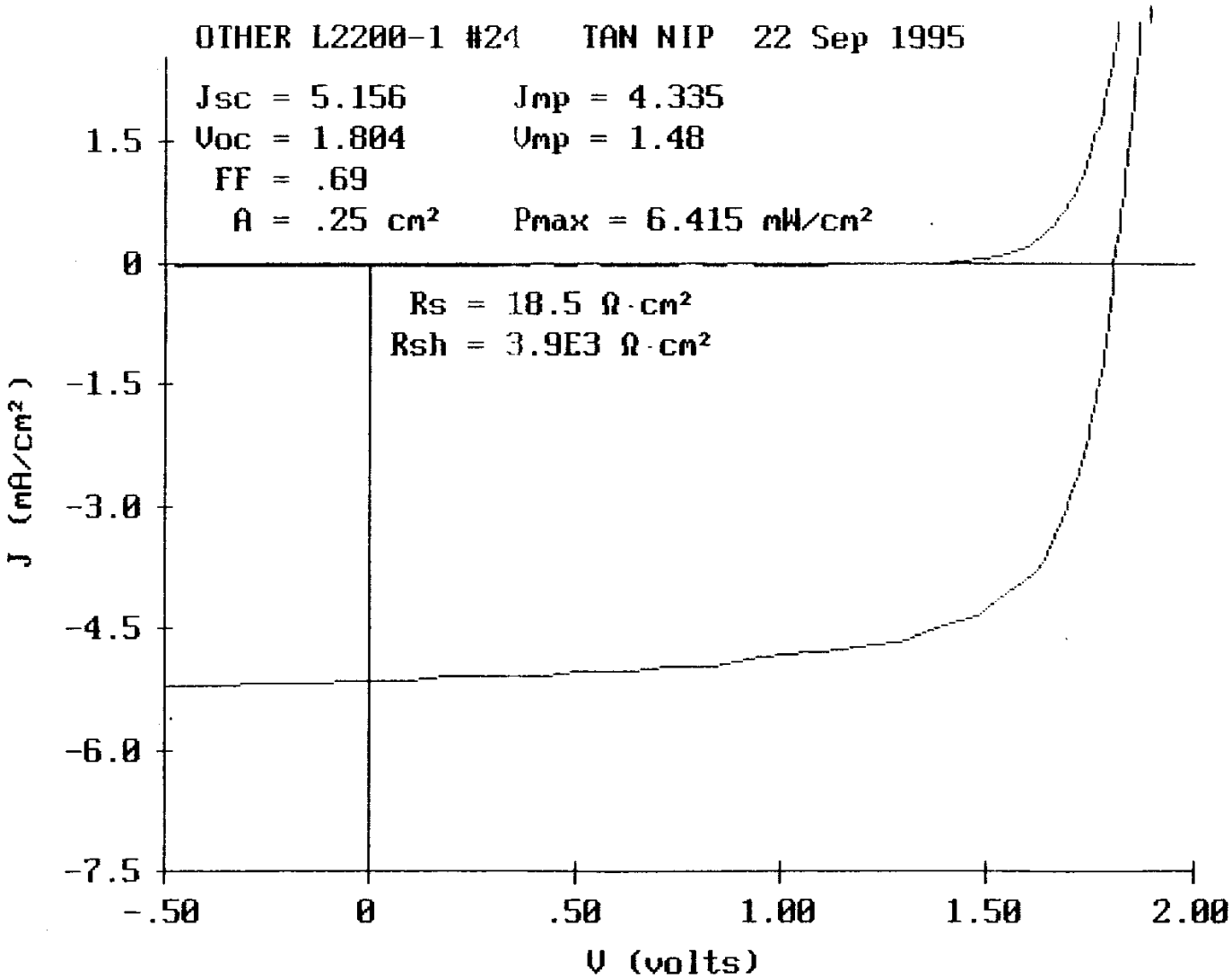

Figure 11-4 J-V curve of an a-Si/a-Si tandem-junction solar cell having an optimized tunnel junction.

11.3 Improved Tunnel Junction Using Doping Graded p-layer

When multiple n-i-p solar cells are stacked on top of each other to form a multiple-junction solar cell, a tunnel junction is formed between the p-layer of the first n-i-p and the n-layer of the second n-i-p. In order to promote strong recombination at the tunnel junction, a relatively more heavily doped p-layer is used to form a good tunnel junction. The more heavily doped p-layer gives more electronic defects for the enhanced recombination, and lower resistivity for the better tunnel junction.

However, when the more heavily doped p-layer is used at the tunnel junction to achieve lower series resistance (better fill factor), the V_{oc} of the n-i-p cell is slightly reduced. This is due to the reduced bandgap when the p-layer is more heavily doped. In order to obtain a low series resistance tunnel junction without the V_{oc} loss, we utilized a new p-layer in which the doping concentration in the p-layer is graded. We believe that the V_{oc} is mostly governed by the boron doping concentration near the p-i interface, while the tunnel-junction performance is mostly governed by the boron doping concentration near the p-n interface. By using relatively more doping near the p-n tunnel junction and relatively less doping near the p-i interface, we can achieve a high V_{oc} and low series resistance tunnel junction.

The first approach in fabricating the dopant graded p-layer was to use two boron doped sublayers with different doping levels as the p-layer. We use an n-i-p-n structure to evaluate the performance of the p-n tunnel junction in terms of V_{oc} loss, junction series resistance and J-V cross-over between the dark and light J-V curves under forward bias. In Table 11-3, we list several representative samples with n-i-p and n-i-p-n structures and with different p-layers, deposited on bare SS substrates.

The data for a standard n-i-p sample (LL866) is displayed in Table 11-3 and shows a V_{oc} of 0.961 V and an R_s of 10.9 Ωcm^2. When an n-layer is deposited over the p-layer, the R_s increases and the J-V curve shows a cross-over. A heavier boron doping in the p-layer is therefore used to reduce R_s. Sample LL809 is a typical n-i-p-n cell in which a p-layer has been deposited with heavier doping, which is optimized for the p-layer at the tunnel junction of multiple-junction solar cell. Due to the use of more doping (7 sccm BF_3 during deposition), the R_s is kept low. However, the V_{oc} has dropped sizably, from 0.961 V to 0.906 V.

Sample LL860 was deposited with a p-layer consisting of two sublayers with different doping, each with approximately half of the thickness of the original p-layer. The R_s is still low, at 13.8 Ωcm^2, and V_{oc} has increased from 0.906 (for LL809) to 0.920 V. Figure 11-5 shows the J-V curves for this device under AM1.5 light. In order to further increase the V_{oc} of the n-i-p-n structure, we increased the thickness of the less doped sublayer, as is shown in the table for

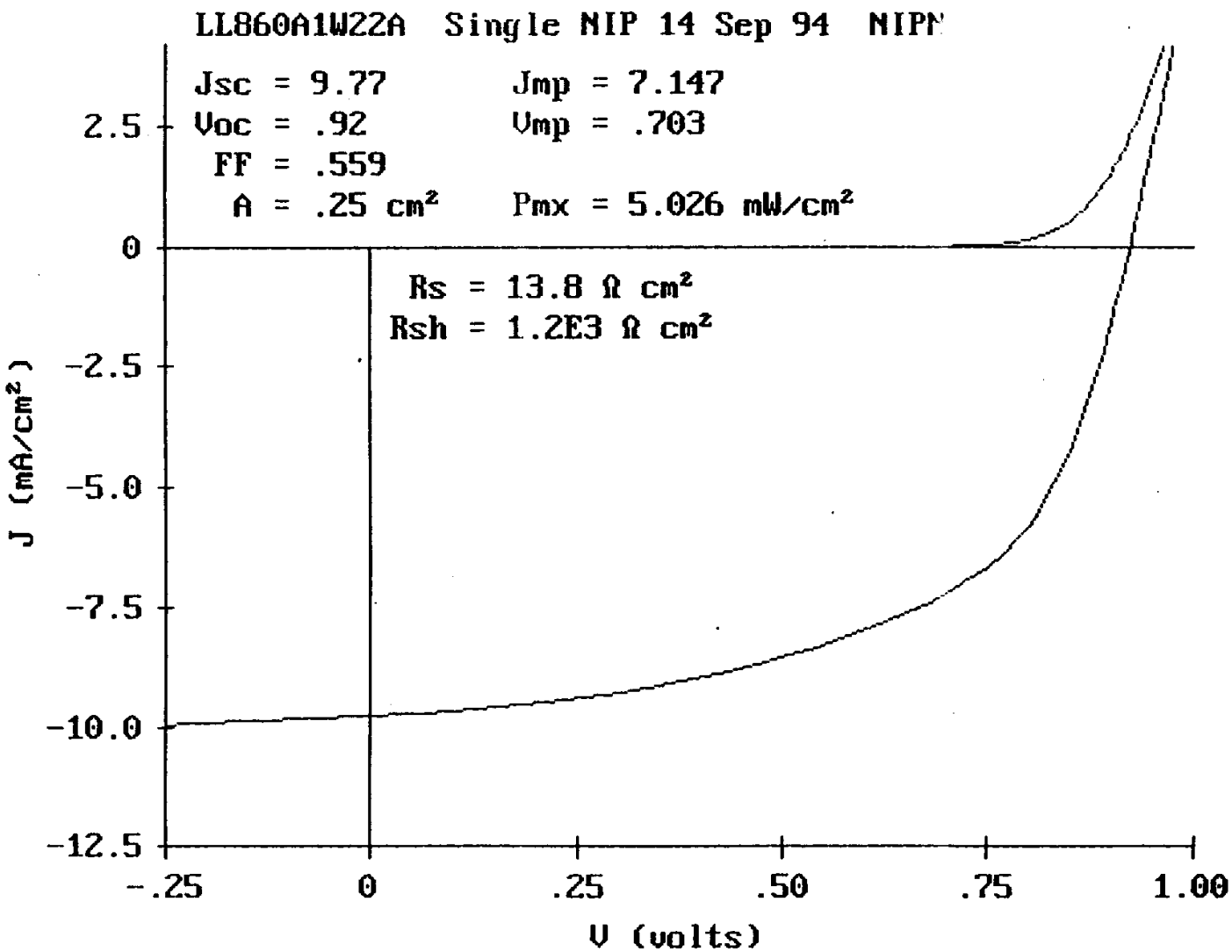

Figure 11-5 J-V curve of an n-i-p device with tunnel-junction p-layer having a graded doping profile.

sample LL871 and in Figure 11-6. The R_s did not increase, however the V_{oc} did increase from 0.92 V to 0.938 V compared to LL860. The high V_{oc} is due to the p-sublayer with relatively lighter doping near the p-i interface. The low R_s is due to the p-sublayer with relatively heavier doping near the p-n interface.

One may also notice that the J_{sc} has decreased for LL871 due to the thicker p-layer. In a real tandem or triple-junction device, the light from the sun will have to travel through the top n-i-p layers before it reaches this tunnel-junction p-layer The effect on the J_{sc} will be negligible unlike in the n-i-p-n test device. Therefore, when LL871 is used in a multiple-junction device, a 32 mV gain in V_{oc} will be achieved without any significant loss in FF or J_{sc}. When the doping profile in the tunnel-junction p-layer is further optimized, further improvement in multiple-junction device is expected. In addition, a graded phosphorus doping in the tunnel-junction n-layer may also lead to improved performance of the tunnel-junction due to the same reason.

11.4 Summary

The tunnel-junction deposition has been systematically investigated and optimized. The optimized tunnel junction results in a much reduced R_s in the triple-junction solar cells.

We investigated a new tunnel-junction design, in which a doping graded p-layer is used. We have demonstrated that a p-layer having higher boron doping near the p-n interface and lower doping near p-i interface results in a higher V_{oc} and a lower R_s for the solar cell compared with ungraded tunnel-junction p-layer.

Table 11-3 The solar cell V_{oc}, FF_r and R_s for n-i-p and n-i-p-n devices with different p-layers.

Sample	Structure	P-layer	V_{oc} (V)	FF	FF_r	R_s (Ωcm^2)	Jsc (mA/cm^2)
LL866	n-i-p	Single 55 sec, 3 sccm BF_3	0.961	0.589	--	10.9	11.8
LL809	n-i-p-n	Single 55 sec, 7 sccm BF_3	0.906	0.560	--	12.1	10.8
LL860	n-i-p-n	Double 30 sec, 3 sccm BF_3 near p-i 30 sec, 7 sccm BF_3 near p-n	0.920	0.559	0.507	13.8	9.77
LL871	n-i-p-n	Double 55 sec, 3 sccm BF_3 near p-I 30 sec, 7 sccm BF_3 near p-n	0.938	0.571	0.503	13.0	9.36

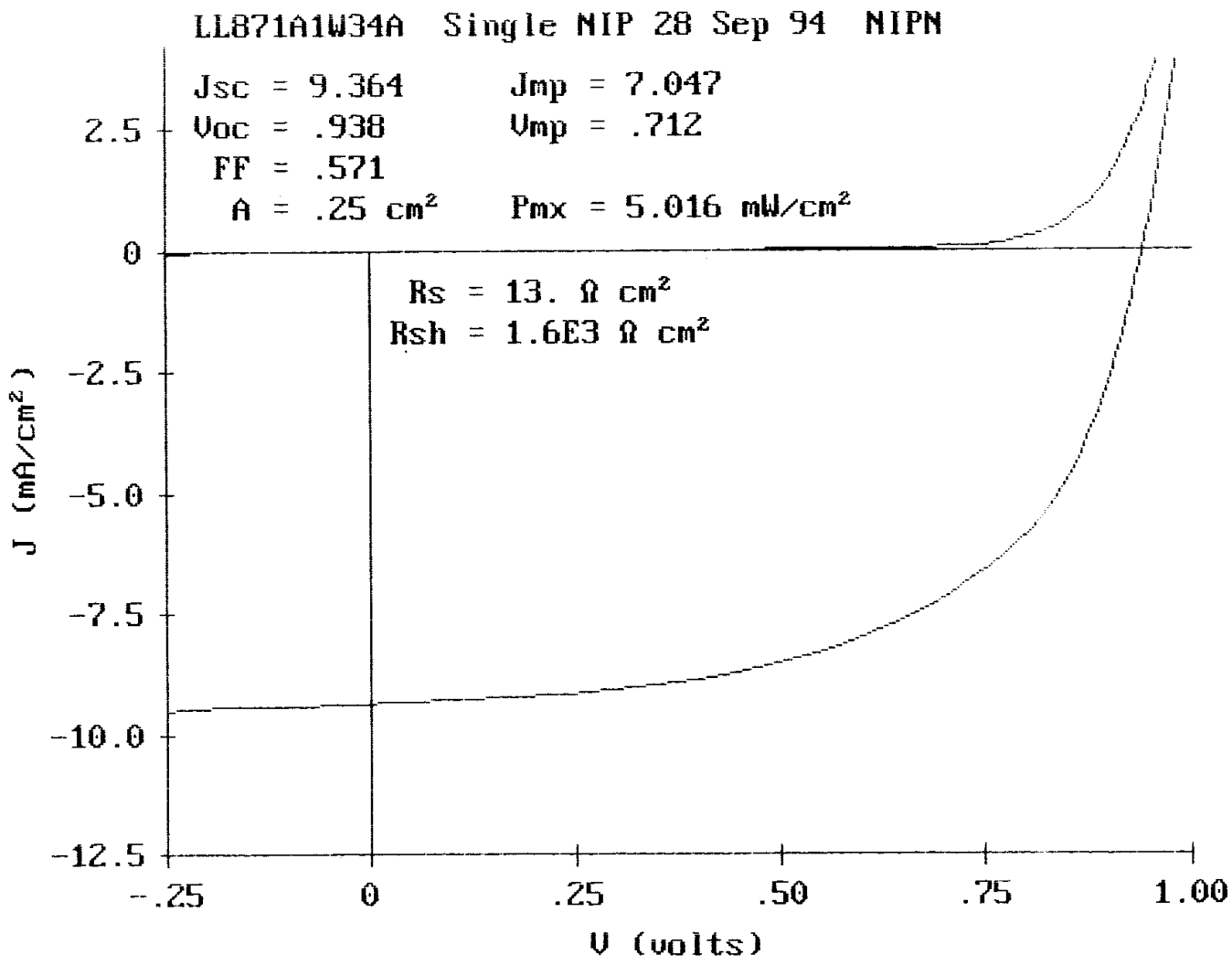

Figure 11-6 J-V curve of an n-i-p-n device with tunnel-junction p-layer having relatively thicker sublayer with less doping.

Section 12
Optimization of Triple-junction a-Si Alloy Solar Cell

12.1 Introduction

A significant portion of the research effort in the development of high stable efficiency triple-junction solar cells is in the optimization of component cells and the tunnel junction, as we described in previous sections. In this section, we emphasize our research efforts on the deposition of triple-junction solar cells. Our triple-junction devices are deposited on SS substrates coated with textured Ag/ZnO back-reflector. After the deposition of n-i-p-n-i-p-n-i-p layers using PECVD, ITO is deposited as the top electrode and an anti-reflection coating, using reactive evaporation in oxygen. An Ag grid is then deposited to complete the cell structure.

12.2 Triple Junction Cell Optimization

In order to improve the triple-junction cell efficiency, we have optimized the following triple-junction cell components: 1) tunnel junction, as described in Section 11-2; 2) a-SiGe bottom cell, as described in Section 3-3; 3) a-SiGe middle cell, as described in Section 3-4; 4) quality of intrinsic a-Si layer for the top cell i-layer, as described in Sections 4 and 10; and 5) component cell current matching.

After these improvements, we have deposited triple-junction a-Si solar cells with 11.2% initial efficiencies. Figure 12-1 is the J-V curve for one of these 11.2% triple-junction cells. The 11.2% triple-junction devices are expected to have around 9.5-10% stabilized efficiency. Figure 12-2 is the QE curve for this improved triple-junction cell device, showing high spectral response in all regions and a desirable current matching among the component cells.

12.4 Summary

Triple-junction a-Si alloy solar cells were deposited and optimized in LL2 deposition systems. Incorporation of the optimized fabrication steps for each component of the triple-junction cell structure has lead to solar cells with an 11.2% initial cell efficiency.

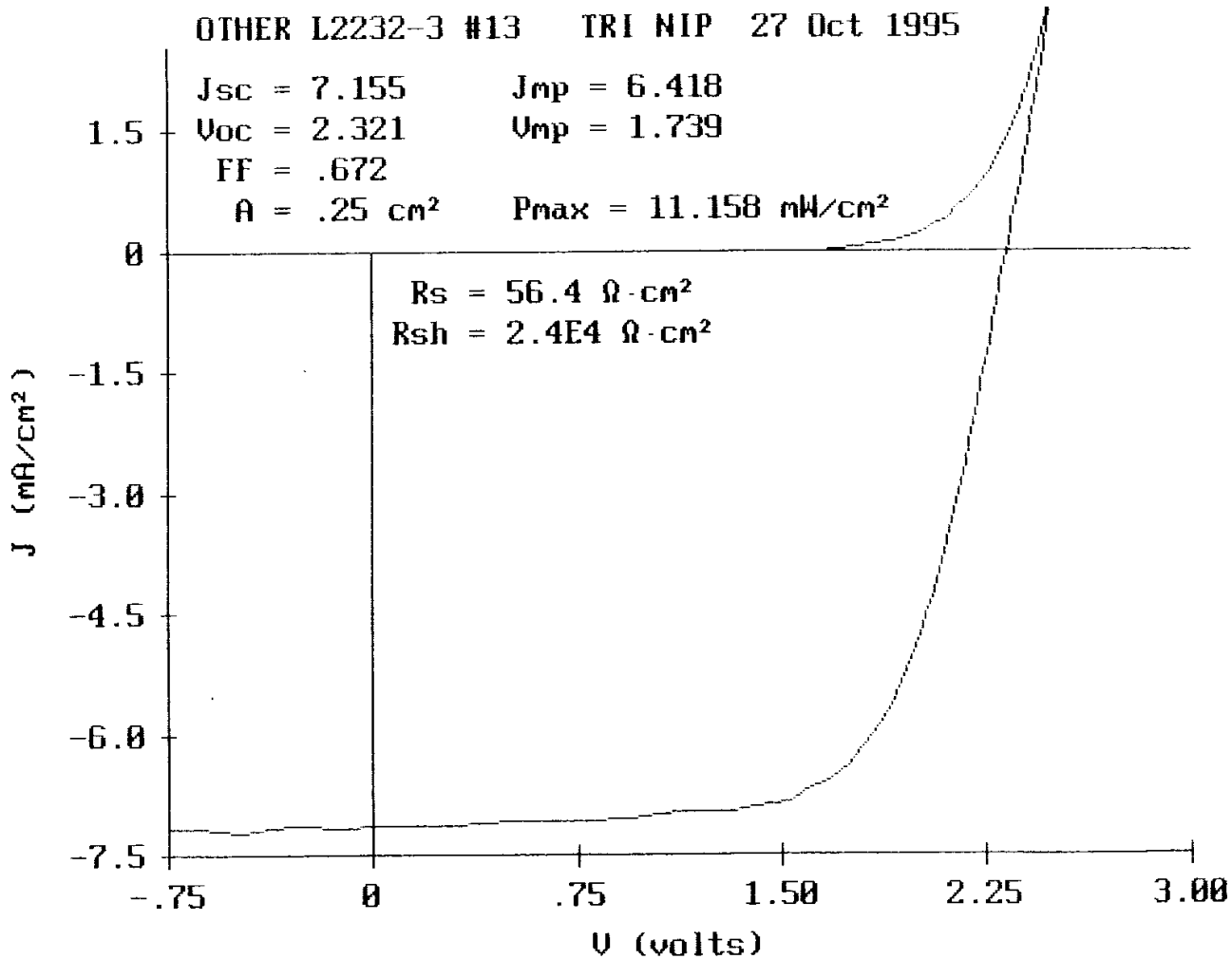

Figure 12-1 J-V curve of a triple-junction cell after preliminary optimization, showing 11.2% initial efficiency.

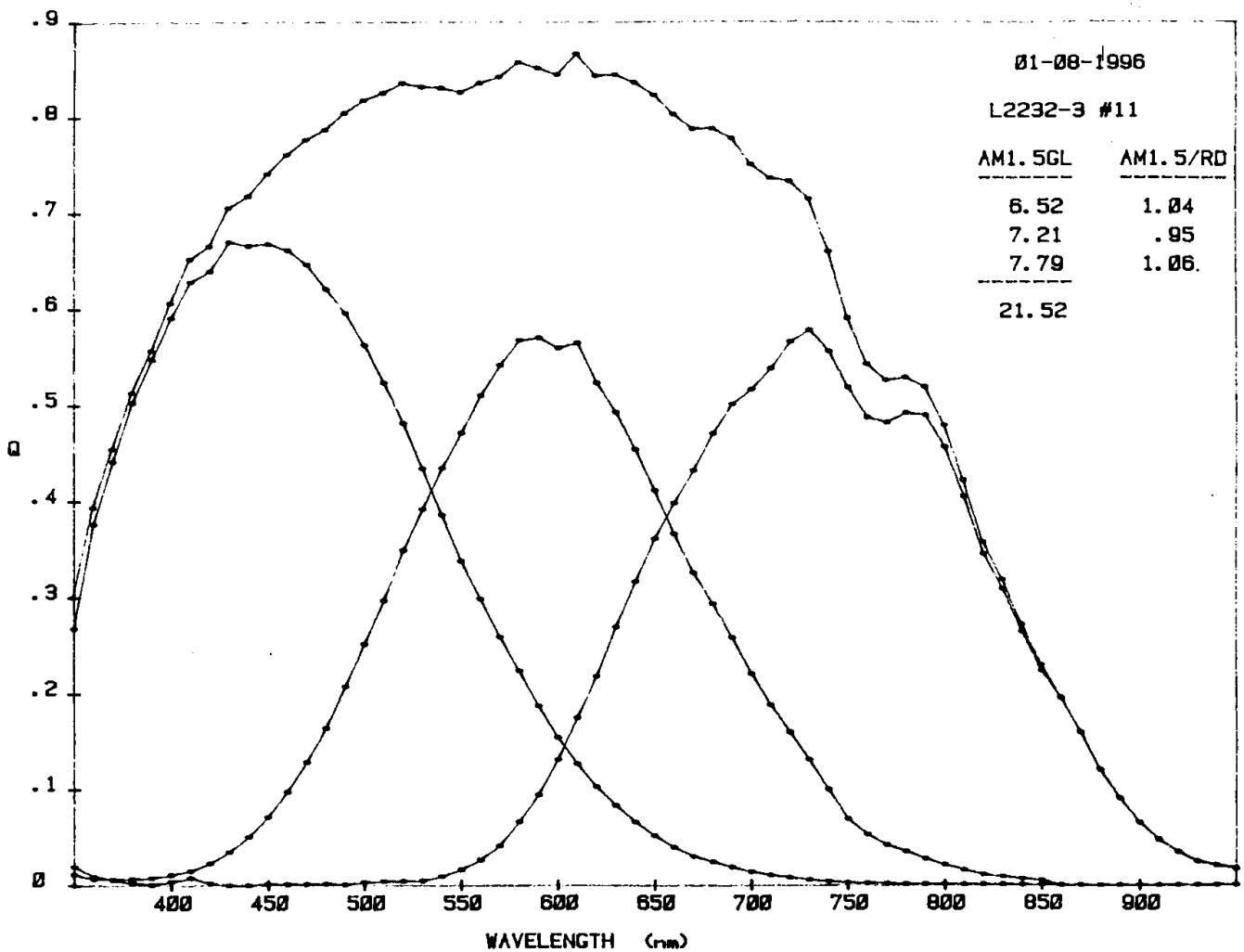

Figure 12- 2 QE curve of the triple-junction cell showing 11.2% initial efficiency.

Section 13
Optimization of Large Area Deposition of a-Si Films and Solar Cell

13.1 Introduction

ECD pioneered the development of multi-junction a-Si alloy solar cells, and the company is now aggressively commercializing the technology through United Solar. Recently, ECD has designed and constructed a 5MW production facility, as shown in Figure 13-1, for United Solar to produce a-Si thin film photovoltaic products at higher volume, higher efficiency, and lower cost. The 5MW machines were used for this research program to gain an understanding of large area related deposition processes and consequently improve efficiency of large-area triple junction solar cells. These areas of research are critical to the success of the ECD's commercialization effort and to the achievement of DOE/NREL mid-term goal for thin film photovoltaics.

Continuous roll-to-roll manufacturing technology utilizing a thin, flexible stainless steel substrate developed by ECD offers a number of advantages in a fully automated, high-throughput PV module production plant. The stainless steel substrate is rugged which improves production yield by eliminating substrate breakage - a significant problem in many glass substrate a-Si alloy PV module manufacturing plants. The transport mechanism for a thin, flexible stainless steel substrate is also mechanically simpler and significantly less expensive than the transport mechanism for conventional glass substrates. Heating and cooling of the substrate during solar cell deposition can also be accomplished quickly, compared to glass substrate manufacturing. As a result, the capital equipment cost for a large-volume plant utilizing continuous roll-to-roll technology will be relatively low.

Previously, ECD designed and built a 2MW a-Si PV manufacturing line for its Russian joint venture, Sovlux. Like the 5 MW, this 2MW production line consists of a continuous roll-to-roll substrate washing machine, a continuous roll-to-roll back-reflector deposition machine, a continuous roll-to-roll a-Si alloy deposition machine, a continuous roll-to-roll top clear conductor deposition machine, and a continuous step and repeat cell cutting machine. This production line produces triple-junction two-bandgap a-Si alloy solar cells consisting of a Si/Si/Si-Ge structure on a 5 mil. thick, 14 in. wide, 2500 ft. stainless steel roll at a speed of 1 ft/min. PV modules with 4 ft^2 areas and 9.5% initial and 8% stable efficiencies were demonstrated from this production line.[7]

<u>ECD/United Solar's 5MW a-Si PV Processor</u>

The state-of-the-art 5MW production equipment incorporates major advances in solar cell design and manufacturing processes achieved by United Solar and ECD, with support from DOE/NREL.[15] The advanced continuous roll-to-roll triple-junction a-Si module production technologies will reduce the module production costs, increase the stabilized module efficiency, and expand the commercial production capacity.

Figure 13-1 5 MW continuous roll-to-roll a-Si alloy solar cell processor.

The 5 MW continuous roll-to-roll a-Si alloy solar cell processor, shown in Figure 13-1, is designed to produce triple-junction, triple-bandgap a-Si/a-SiGe/a-SiGe solar cells in a single pass in a continuous roll-to-roll process. The solar cell structure was shown in Figure 1-1. United Solar recently achieved a new world record efficiency of 14.6% initial efficiency utilizing a similar solar cell structure. The 5 MW production line is now in full production mode.

The input to the process is a roll of back-reflector coated stainless steel. Web rolls are approximately 2,500 feet in length, 14 inches in width, and weigh up to 1,000 pounds. The beginning of the input roll will be welded to the end of the preceding roll in situ. Web transport through the system is single pass at a rate of 2 ft/min.

The triple-junction cell structure consists of doped and undoped thin films of a-Si alloy semiconductor deposited sequentially and simultaneously in proper order as the web is transported through each successive chamber section (See Figure 1-2). Deposition is achieved by low-pressure RF plasma chemical vapor deposition.

The multi-section a-Si alloy deposition machine consists of a pay-off chamber section, nine process sections for depositing the triple-junction cell and terminating with a take-up chamber (See Figure 1-2). Each section is separated by a "gas gate." The gas gates are designed so that the migration of dopants and other process gases between chambers is eliminated. The position, tension and speed of the web through the processing chambers are computer-controlled. Web passage through the process chambers is such that deposition takes place on the underside, and front facing in the web transport system is not allowed. Pay-off and take-up chambers contain all of the necessary web-drive components, auxiliary rolls, tension sensors and steering mechanisms. Pumping for these chamber sections is done by a Roots blower and mechanical displacement-type vacuum pumps.

In each of the process chambers, transport of reactant and dilutent gases to the reaction zone is from mixing manifolds designed to provide the specified mixture to be appropriately distributed in each individual reaction zone. Reaction zone pressures are controlled by a gas-pumping system using variable conductance valves, flow controllers, and pressure transducers used together in a closed-loop computer-controlled feedback system for reach process section. Heat is provided to maintain the web at the specified temperature by an array of quartz-type lamps located above the web, and radiating downward controlled by thermocouples in individual closed-loop circuits.

In this advanced solar cell processing machine, several important new features were incorporated:

- The machine was designed to minimize incorporation of contaminants into deposited material. The machine has been fabricated, constructed and assembled under a strict procedure to minimize contaminants.
- The machine operation is computer-controlled. With improved software developed by ECD which enables an operator, monitoring interactive CRT displays, to start, operate, and shut-down the machine using computer keyboards that control all the machine

functions including pumping, gas recipes, flow meters, heaters, supplies, valves, and web drive systems. The computerized system incorporates automatic sequence of operations with many safety interlocks, and other special design features that make the production operation safe and reliable. The computer system also provides a historical data acquisition system which monitors and stores all the processing data in computer discs.

- The machine is equipped with a maintenance-free effluent scrubbing exhaust system consisting of a burn-box and scrubber.
- The web transport system is improved, and the web pass line is horizontal and flat, as seen in Figure 13-1. Previously built machines utilized a catenary web pass line.
- The gas-feed and cathode systems for depositing bottom and middle intrinsic layers incorporate diffusion-controlled gas-feed/deposition mechanism which allows adjustment of profile of Ge and Si in the layers.
- The cathode configuration and deposition conditions have been optimized to deposit microcrystalline p-layers.
- Improved mechanical parts design for internal components of the process chambers has significantly reduced component heat distortion during processing.
- Serviceability and accessibility have been improved with new non-catenary design. Using powered lid lifts for all chambers, all internal chamber components are accessible for servicing at waist-high levels. The use of separate above-the-ground troughs for wiring and piping has improved the appearance as well as the accessibility of the external machine components.

During the program period, this advanced 5MW system was under process optimization. Members of ECD's and United Solar's research staffs have participated in a joint effort to optimize the this 5MW production line. In particular, scientists involved with this NREL high efficiency, triple-junction solar cell program have made extensive contributions to the optimization effort participating in the experimental design, processing of the web, preparation of top contacts and characterization of small area cells. Presently, the 5MW program is in full scale production. Below we describe some of the results from the optimization program.

Optimization of Large Area Deposition of a-Si Alloy Solar Cells

In terms of a-Si:H films and devices, we have focused our efforts on optimizing the component layers of the top cells for the triple-junction devices. As is usually observed for a-Si:H devices, the best cells have been made using high H_2 dilution and moderate substrate temperatures. Tables 13-1 and 13-2 display properties of top component cells (0.25 cm^2 size test cell) made on bare stainless steel (without back reflector) with i-layers made under different hydrogen flows and substrate temperatures. The thickness of these devices were measured by the capacitance technique and found to be approximately the same within experimental error. The cell with the i-layer prepared at twice the H_2 flow has a significantly higher FF and a slightly higher V_{oc}, showing the importance of high hydrogen dilution to the quality of the top cell i-layer. From table 13-2, the FF improves by roughly 0.015 when the i-layer substrate temperature is increased by 50°C. Both of these trends were expected due to the well documented improvements in a-Si:H quality with higher hydrogen dilution and moderate substrate temperatures due to higher

adatom surface mobilities or enhanced etching of weakly bonded material on the growing film surface which lead to denser, more homogeneous films.

Table 13-1 Performance of top component cell as a function of hydrogen dilution, showing an improvement in V_{oc} and FF with increasing H_2 flow. The other deposition conditions such as substrate temperature and RF power are kept constant for these devices.

H_2 Flow (sccm)	J_{sc} (mA/cm^2)	V_{oc} (V)	FF	P_{max} (mW/cm^2)	R_s (Ωcm^2)
standard	6.2	0.954	0.692	4.1	9.6
standard	6.1	0.969	0.694	4.1	8.1
2 x standard	6.0	0.977	0.721	4.2	8.3

Table 13-2 Performance of top component cell as a function of top i-layer web temperature during deposition, showing an improvement in FF and J_{sc} with higher substrate temperature. The other deposition conditions such as hydrogen flow and RF power are kept constant for these devices.

Substrate Temperature (°C)	J_{sc} (mA/cm^2)	V_{oc} (V)	FF	P_{max} (mW/cm^2)	R_s (Ωcm^2)
Standard	7.0	0.977	0.707	4.8	7.3
50°C higher	7.4	0.972	0.724	5.2	6.8

In contrast, the behavior of the cell properties with varying applied power was contrary to the commonly observed improvement in a-Si:H quality with lower powers and the accompanying lower deposition rates. As can be seen from Table 13-3, with increasing power up to 200W higher than the standard power, the FF was found to improve even when the i-layer thickness of the cells increased with the higher powers. Increasing the power further, the thickness changes very little however there is still an improvement in the FF showing that our best material is made at the highest powers, which are presently limited by the machine hardware. Along with the improvement in FF, the cells prepared at the higher powers also have slightly higher V_{oc}. The improvement in cell properties with increased power is the subject for further studies.

Table 13-3 Performance of top component cell as a function of RF power, showing an improvement in V_{oc} and FF with increasing RF power.

Applied RF Power (W)	J_{sc} (mA/cm^2)	V_{oc} (V)	FF	P_{max} (mW/cm^2)	R_s (Ωcm^2)
standard	6.1	0.969	0.694	4.1	8.1
200W higher	7.0	0.969	0.705	4.8	6.5
400W higher	6.9	0.975	0.719	4.8	8.1

Incorporating the best conditions for n-, i- and p-layer preparation, preliminary optimized top cells have the following typical device performance: J_{sc}=7.5-8.0 mA/cm^2, V_{oc} = 0.97-0.98V, FF=0.72-0.73. Figure 13-2 shows a J-V curve for a typical top cell. Under different conditions, we have obtained cells with V_{oc} as high as 1.00 V, as shown in Figure 13-3.

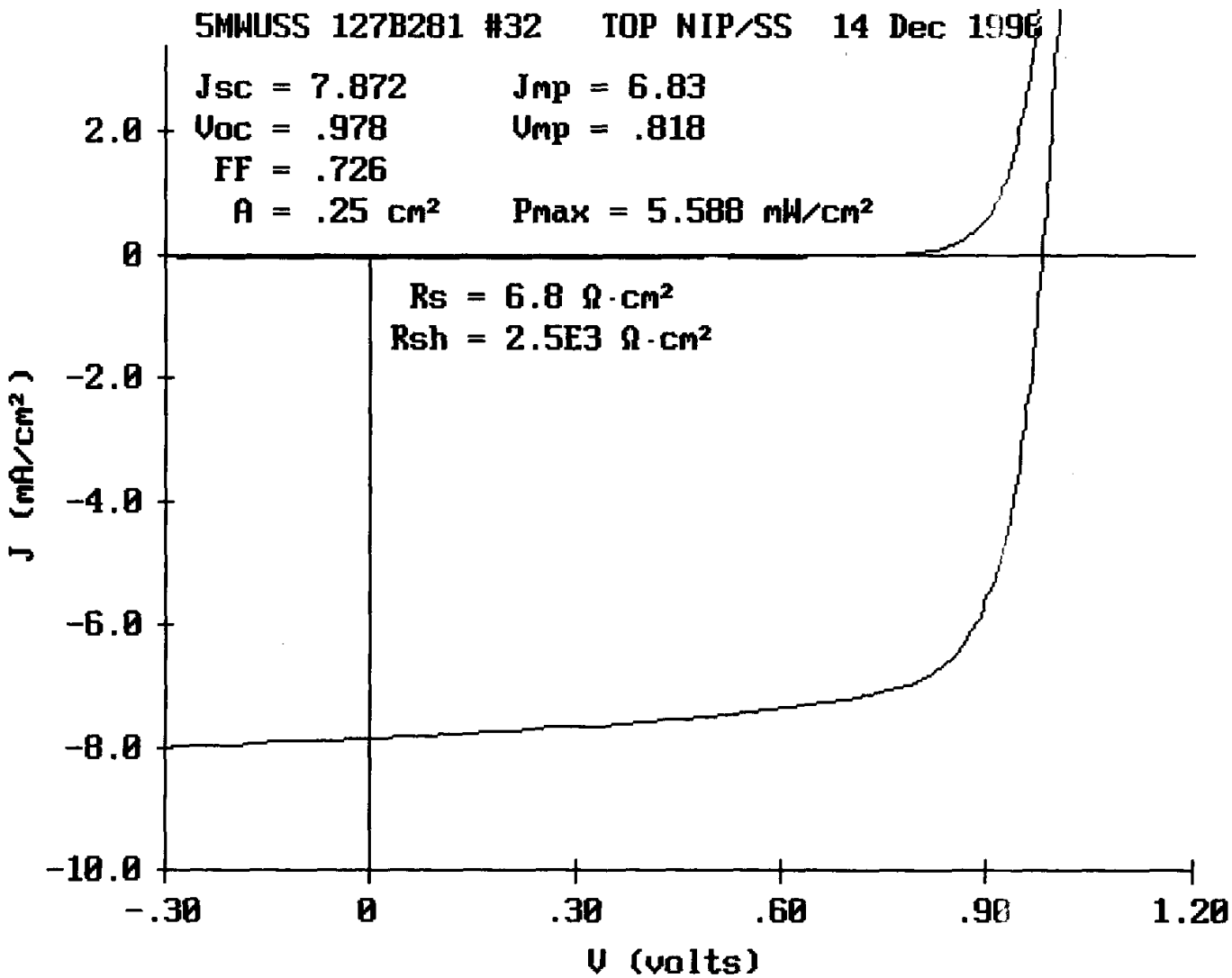

Figure 13-2 J-V curve for a typical top cell produced in large area in the 5MW a-Si solar cell processor.

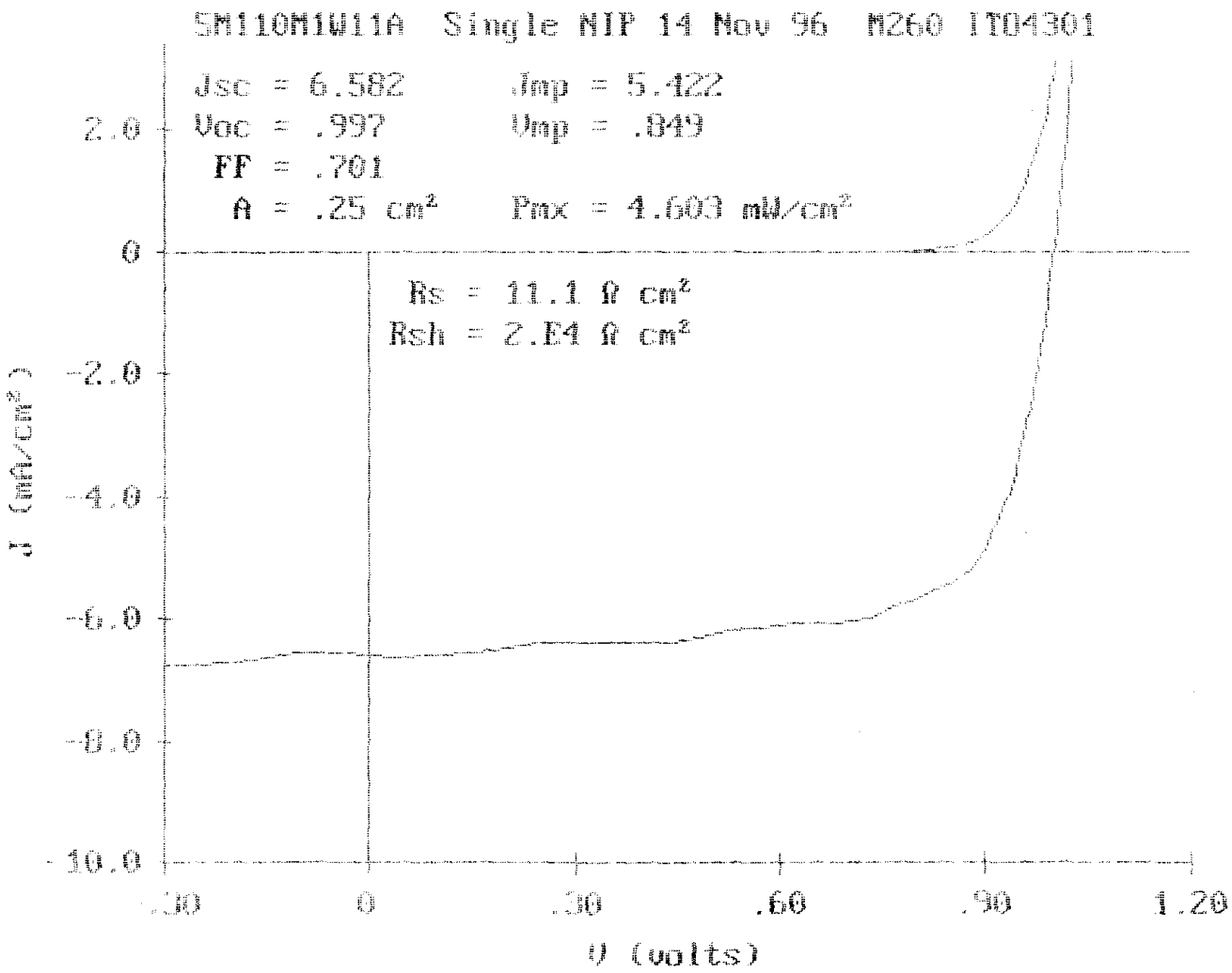

Figure 13-3 J-V curve of a top cell produced in the 5 MW machine, showing a V_{oc} of 1.00 V.

Section 14
Optimization of Large Area Deposition of a-SiGe films and solar cells

Optimization of deposition uniformity

For optimization of the bottom and middle a-SiGe cells, one important issue is to find process conditions which allow for the uniform deposition across the entire width and length of the cathodes. This is obviously important in the roll-to-roll manufacturing process because nearly all of the cathode area is utilized for the large area solar module production. In addition, these uniformity issues have become more important in this generation of ECD's production lines because larger cathodes are used in the 5MW line.

Figure 14-1 depicts one of the uniformity problems encountered for a-SiGe thin film solar cell deposition over large area. The figure displays data for small area (0.25 cm^2) single junction a-SiGe n-i-p solar cell test devices whose doped layers were prepared with the web in motion and the i-layers made with the web in the static condition (a static burn). These special types of cells are produced to study the deposition uniformity in the roll-to-roll machine for a particular layer, which, in this case, is the a-SiGe i-layer. Following this procedure, static burns are made for each of the cathodes associated with i-layer depositions. Cells can be made from any section of these burns allowing for characterization of uniformity across the burns and thus across the cathodes. To test the uniformity of cell properties across the length of the cathode and the gas flow direction, solar cells were made from different parts of the static i-layer depositions as is shown for one such static deposition in Figure 14-1. The cells, for which data is shown in this figure, were made under unoptimized conditions and without the benefit of an Ag/ZnO back reflector. The J-V measurements for cell characterization were made using 530 nm cutoff filtered AM1.5 light. When cells were made from the exhaust side, the center and the gas inlet side of the cathode burn, it was found that for the bottom cell preparation, the Ge content (as measured with Energy Dispersive Spectroscopy) increased on average by 11-12% as one scanned from the exhaust to the inlet side of the cathode. As can be seen from the data in the figure, this increase in Ge content led to the expected decreases in V_{oc} and FF and an increase in J_{sc} when the properties were scanned across the cathode length. Along with this increase in Ge concentration, an increase in the i-layer thickness was also found as can be seen from the data in Figure 14-1.

This uniformity problem leads to fluctuations in the cell properties through the thickness of the solar cell i-layers prepared with the web moving. The variations in cell properties across all of the 10 cathodes used to make the bottom cell a-SiGe layer are shown in Figure 14-2. In the figure, each cathode is 4 units long on the horizontal scale. The cells used to obtain the data for this figure were again made from different parts of i-layer burns as they were to obtain the data from Figure 14-1. The oscillations in each of the cell properties are clearly apparent. The fluctuations in the Ge content were also observed in SIMS profile for a cell made under standard conditions (all layers made with the web in motion) in the form of a near zigzag profile of the Ge concentration. Such fluctuations in the Ge content led to variations in the bandgap and mobility edges across the i-layer which could hinder carrier collection.

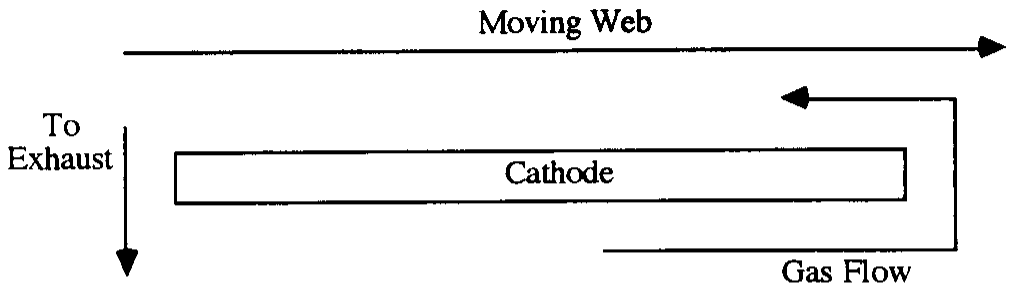

Voc (V)	0.67	0.61	0.57
Jsc (mA/cm2)	8.6	9.7	10.4
FF	0.63	0.55	0.46
Pmax (mW/cm2)	3.6	3.3	2.7
Relative thickness	18% thinner than Std	Std	42% thicker than Std

Figure 14-1 Performance of a-SiGe solar cells with i-layers deposited in a static mode near the exhaust side, the center and the gas inlet side of the cathode burn, showing the unoptimized deposition uniformity with a large-area cathode.

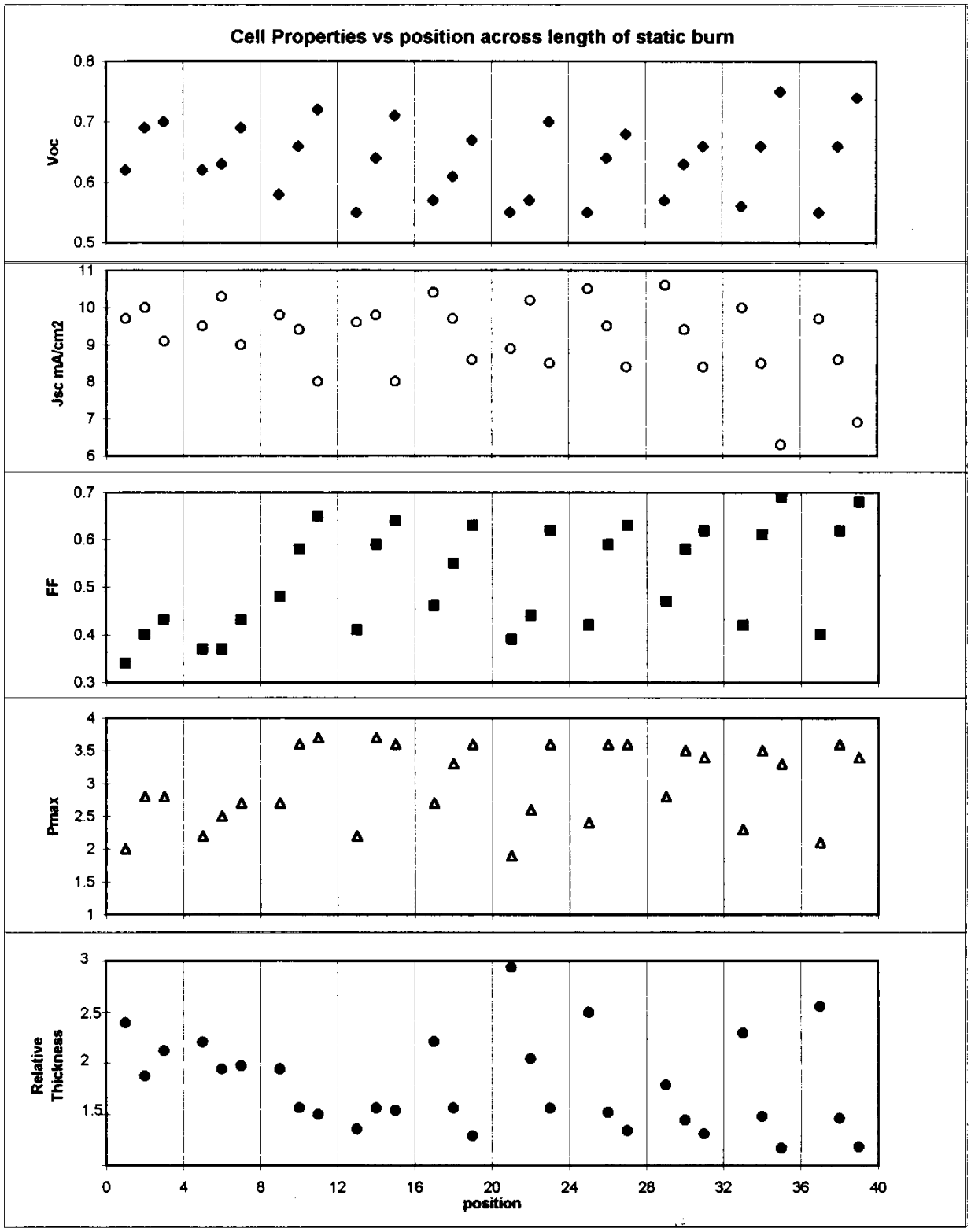

Figure 14-2 Deposition uniformity for a-SiGe solar cell before optimization for all of the 10 cathodes used to make the bottom cell a-SiGe layer.

Figure 14-3 shows that this uniformity problem is strongly related to the film deposition rate. In the figure, the ratio of thickness of films taken from the inlet side of an i-layer burn to the thickness of films taken from the outlet side of the same burn is plotted as a function of deposition rate for several cathodes with the burns prepared under a variety of deposition conditions. As can be seen from the figure, the inlet/outlet ratio used to judge the film uniformity increases from the uniform value of 1 as the deposition rate increases. Since a significant amount of deposition is observed at the exhaust side of the cathode, this effect is likely not related to gas depletion.

In order to minimize this uniformity problem, we have studied the dependence of the film uniformity on a number of deposition conditions and found that by carefully selecting a combination of deposition parameters including, for example, the RF power and the deposition temperature, we can obtain uniform depositions at relatively high deposition rates. Figure 14-4 displays how the film thickness can be made more uniform across one cathode, as an example, when the power is lowered. At the higher powers, the non-uniformity likely represents the depletion of gas species as the gas moves towards the pumping exhaust port with the higher Ge contents at the inlet side related to an enhanced depletion of GeH_4. While the use of the lower powers improved the uniformity, they also led to a low deposition rate not compatible with the rated 2 ft/min line speed, i.e., 5MW/yr production throughput.

By lowering the temperatures in certain critical areas of the process chamber during deposition, the uniformity of the a-SiGe films can be significantly improved without a loss in the deposition rate. As is shown in Figure 14-5, the inlet/outlet ratio of film thickness approaches unity in the desirable range of deposition rates (relative rate=1) when the temperatures in the critical areas are lowered, as indicated with the diamond point in the figure in the lower right side of the curve. This improvement in the uniformity with decreased temperatures is likely not related to a decrease of CVD decomposition of process gases, but is probably related to the decrease of some type of excitement of the gas species by the high temperatures which allows for easier decomposition of the gas species at the moment the gas reaches the RF plasma at the inlet side of the cathode.

With the combination of the lower temperatures and slightly lower powers, we were able to obtain reasonably thick i-layers and uniform depositions across the cathode as is displayed in Figure 14-6. The figure displays data for one of the cathodes, as an example, before the improvements and after the improvements. The cells were again made with static i-layers and dynamic doped layers (the same method as described for the data in Figure 14-1). There is no bandgap profiles for these a-SiGe cells due to the static i-layer deposition. One can see that the uniformity in terms of Ge content and cell properties is dramatically improved under these conditions allowing for the production of uniform i-layers when the web is in motion.

Optimization of middle cell a-SiGe deposition using Design of Experiments

Besides the uniformity issue, another important aspect of a-SiGe deposition is the film quality. We have optimized the deposition to improve the film quality using a Design of Experiments

approach.[17] A 5-factor Draper-Lin small composite design with face-centered design characteristic is used with the deposition conditions covering applied RF power, disilane

flow (Si_2H_6), hydrogen dilution (H_2), germane to silicon ratio (Ge/Si), and bandgap grading (PI). Due to the proprietary nature of the parameters, the detailed value of these conditions are not disclosed in this report. Table 14-1 list the design parameters and the solar cell results for the experiments.

All other deposition conditions not included in the table were previously optimized. For this study, the cells were deposited on bare stainless steel without a back reflector. It was later proved that the conditions that were found optimum for the cells on bare stainless steel were also optimum for cells deposited on back reflector material. All cell data to be discussed here were obtained using 530 nm cutoff long-pass filtered light. For the middle cell, a cell on bare stainless steel needs to have a J_{sc} value of at least 7.0 mA/cm^2 with the 530 nm filtered light. Thus, we were looking for conditions which would make the best cell with 7.0 mA/cm^2 and V_{oc} around 0.70 V.

Figure 14-7 and 14-8 display the Pareto charts for the J_{sc} and cell efficiency measured under the 530 nm filtered light (power output under filtered red light). In Figure 14-7, the expected strong dependence of J_{sc} on the Ge/Si ratio is observed due to the increase in current with increasing Ge content. The strong dependence with power is likely related to the increase in i-layer thickness with increased power leading to more light absorption and higher currents. The influence the cross term between the Si_2H_6 and the H_2 flow has on J_{sc} is again likely related to the i-layer thickness since the thickness usually decreases with increasing H_2 dilution.

From Figure 14-8, the cell efficiency is strongly influenced by the applied power. In Figure 14-9, a contour plot of the efficiency is shown with the x and y axes being the applied power and Si_2H_6 flow, respectively. This plot was obtained by fixing the H_2 flow, GeH_4/Si_2H_6 ratio and the steepness of the Ge/Si profile across the i-layer at center values. Overlapping parts of the efficiency contour lines are darker contour lines which represent different J_{sc} values. As was mentioned earlier, we are searching for cells with J_{sc} values around 7.0 mA/cm^2. Following the 7.0 mA/cm^2 contour line, one can see that the highest P_{max}, around 3.64 mW/cm^2, is obtained at a high power and mid Si_2H_6 flow values as marked by a cross in the figure. We later proved that there was no benefit in using higher powers. Figure 14-10 is a plot similar to the one shown in Figure 14-9 except here the GeH_4/Si_2H_6 flow is at a higher value. Here again for J_{sc}=7.0 mA/cm^2 the optimum power seems to be near high power, however the optimum Si_2H_6 flow is near the low value. However under these high GeH_4/Si_2H_6 conditions, the highest P_{max} for J_{sc}=7.0 mA/cm^2 is between 3.4 and 3.5 mW/cm^2 while under the moderate GeH_4/Si_2H_6 ratio the highest P_{max} is between 3.6-3.7 mW/cm^2. Thus, using the lower GeH_4/Si_2H_6 conditions will give higher performance cells. The data also showed that there is no benefit in using even lower GeH_4/Si_2H_6 ratios.

Other contour plots for the efficiency are shown in Figures 14-11 and 14-12 where this time the x and y axes are the Si_2H_6 flow and GeH_4/Si_2H_6 ratio, respectively. In both figures, moderate H_2 11 and a moderate power (mid value) assumed in Figure 14-12. One can see from Figure 14-11

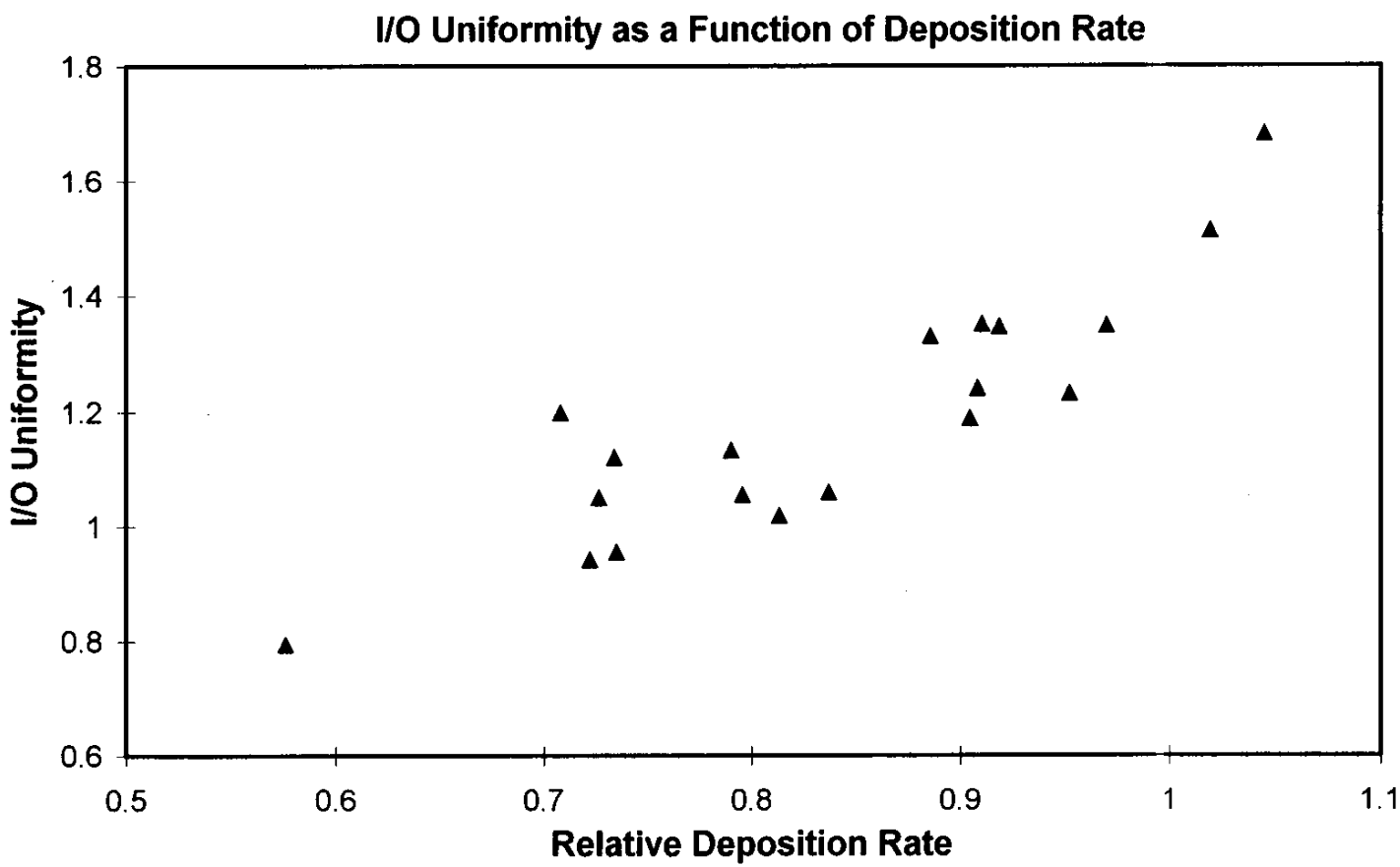

Figure 14-3 Ratio of thickness of films taken from the inlet side of an i-layer burn to the thickness of films taken from the outlet side of the same burn is plotted as a function of deposition rate for several cathodes with the static burns prepared under a variety of deposition conditions, showing that this uniformity problem is strongly related to film deposition rate.

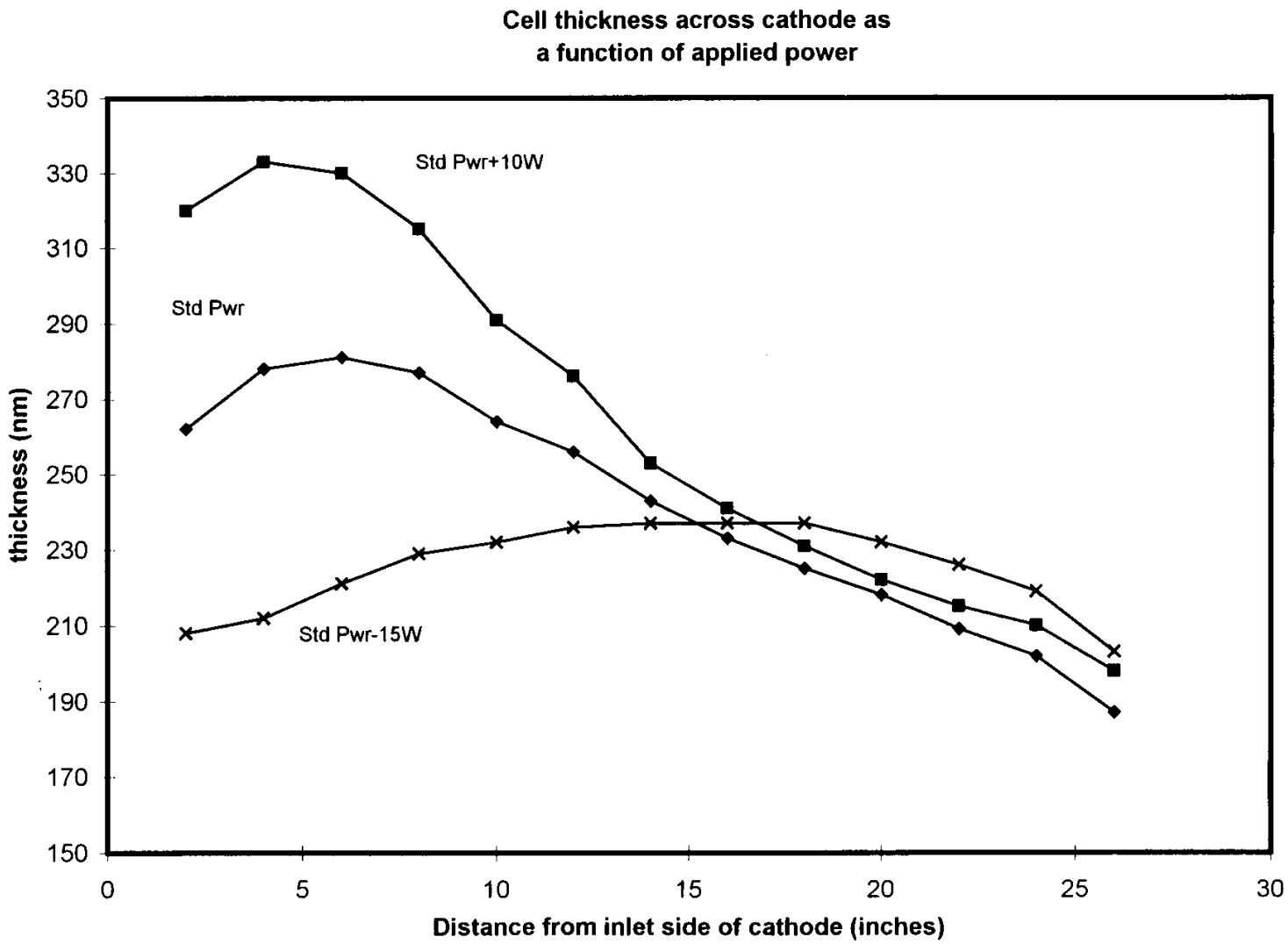

Figure 14-4 Deposition thickness uniformity over large area cathode with different RF power, showing improved uniformity at lower power.

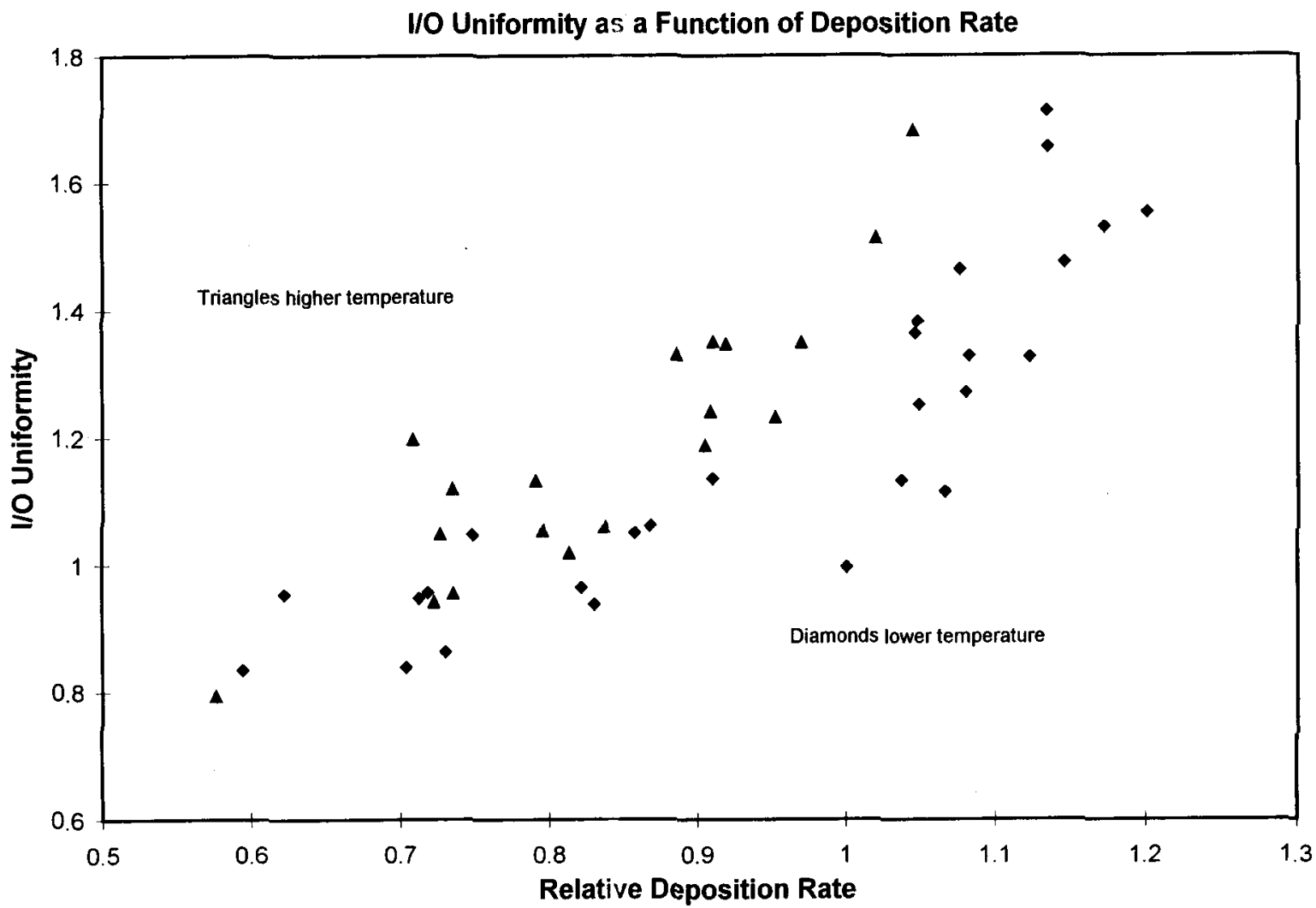

Figure 14-5 Deposition thickness uniformity over large-area cathode with different deposition rate, showing high uniformity (I/O uniformity=1) at a desirable deposition rate (Relative deposition rate=1) as required by the machine line speed.

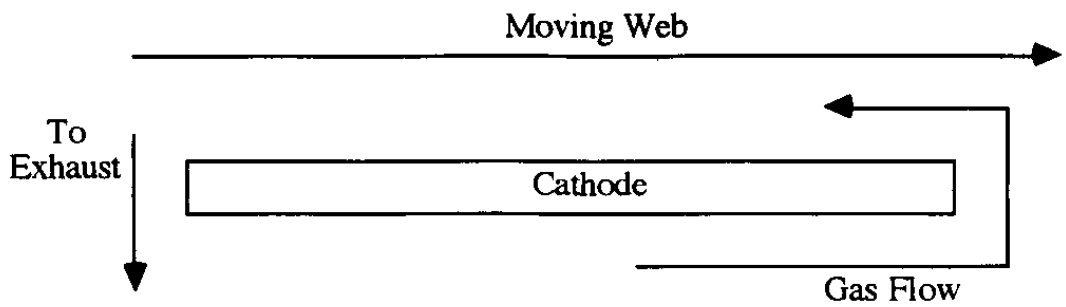

Before Improvements

Voc (V)	0.67	0.61	0.57
Jsc (mA/cm2)	8.6	9.7	10.4
FF	0.63	0.55	0.46
Pmax (mW/cm2)	3.6	3.3	2.7
Relative Thickness	18% thinner than Std	Std	42% thicker than Std

After Improvements

Voc (V)	0.65	0.65	0.66
Jsc (mA/cm2)	8.7	8.7	8.8
FF	0.57	0.58	0.57
Pmax (mW/cm2)	3.3	3.2	3.3
Relative Thickness	3% thinner than Std	Std	4% thicker than Std

Figure 14-6 Performance of a-SiGe solar cells with i-layers deposited in a static mode near the exhaust side, the center and the gas inlet side of the cathode burn, before and after uniformity optimization.

that at high power, the highest P_{max} is 3.63 mW/cm^2, and from Figure 14-12 that at mid power, the highest P_{max} is 3.56 mW/cm^2. Comparing these two cases, the optimum power is near the high power. After the optimization of the middle cell, high performance a-SiGe middle cell was achieved. Figure 14-13 shows a J-V curve of a typical a-SiGe middle cell for use in a triple junction solar cell.

Table 14-1 Five-factor Draper-Lin design for the optimization of middle cell a-SiGe i-layer quality.

RUN	Power (W)	Si2H6 (sccm)	H2 (sccm)	Ge/Si ratio	Bandgap grading	Pmax(red) (mW/cm2)	Voc (V)	Jsc (mA/cm2)	FF	Integ.Q (mA/cm2)
1	High	High	Low	High	High	3.72	0.728	7.92	0.645	13.9
2	High	Low	High	High	High	2.89	0.716	5.71	0.707	12.4
3	Low	High	High	High	Low	2.84	0.694	6.12	0.667	12.34
4	High	High	High	Low	Low	3.54	0.804	6.67	0.661	12.98
5	High	High	Low	Low	Low	3.51	0.824	6.38	0.668	12.82
6	High	Low	Low	Low	High	2.73	0.846	4.39	0.734	10.37
7	Low	Low	Low	High	Low	2.63	0.751	4.88	0.717	11.41
8	Low	Low	High	Low	High	2.13	0.8	3.65	0.729	9.76
9	Low	High	Low	High	High	2.5	0.68	5.4	0.67	10.51
10	High	Low	High	High	Low	2.92	0.75	5.6	0.695	
11	Low	High	High	Low	High	2.81	0.775	5.17	0.703	11.12
12	Low	Low	Low	Low	Low	2.13	0.8	3.65	0.729	9.76
13	Low	Mid	Mid	Mid	Mid	2.51	0.75	4.81	0.703	10.82
14	High	Mid	Mid	Mid	Mid	3.54	0.789	6.54	0.687	12.76
15	Mid	Low	Mid	Mid	Mid	2.89	0.799	5.1	0.729	11.47
16	Mid	High	Mid	Mid	Mid	3.61	0.731	7.29	0.677	13.52
17	Mid	Mid	Low	Mid	Mid	3.52	0.776	6.5	0.696	13.1
18	Mid	Mid	High	Mid	Mid	3.4	0.744	6.48	0.705	13.11
19	Mid	Mid	Mid	Low	Mid	3.22	0.8	5.63	0.714	11.74
20	Mid	Mid	Mid	High	Mid	3.67	0.711	7.86	0.657	13.88
21	Mid	Mid	Mid	Mid	Low	3.51	0.771	6.52	0.698	12.86
22	Mid	Mid	Mid	Mid	High	3.37	0.748	6.38	0.706	12.88
23	Mid	Mid	Mid	Mid	Mid	3.34	0.758	6.52	0.677	13.11
24	Mid	Mid	Mid	Mid	Mid	3.34	0.758	6.52	0.677	13.11

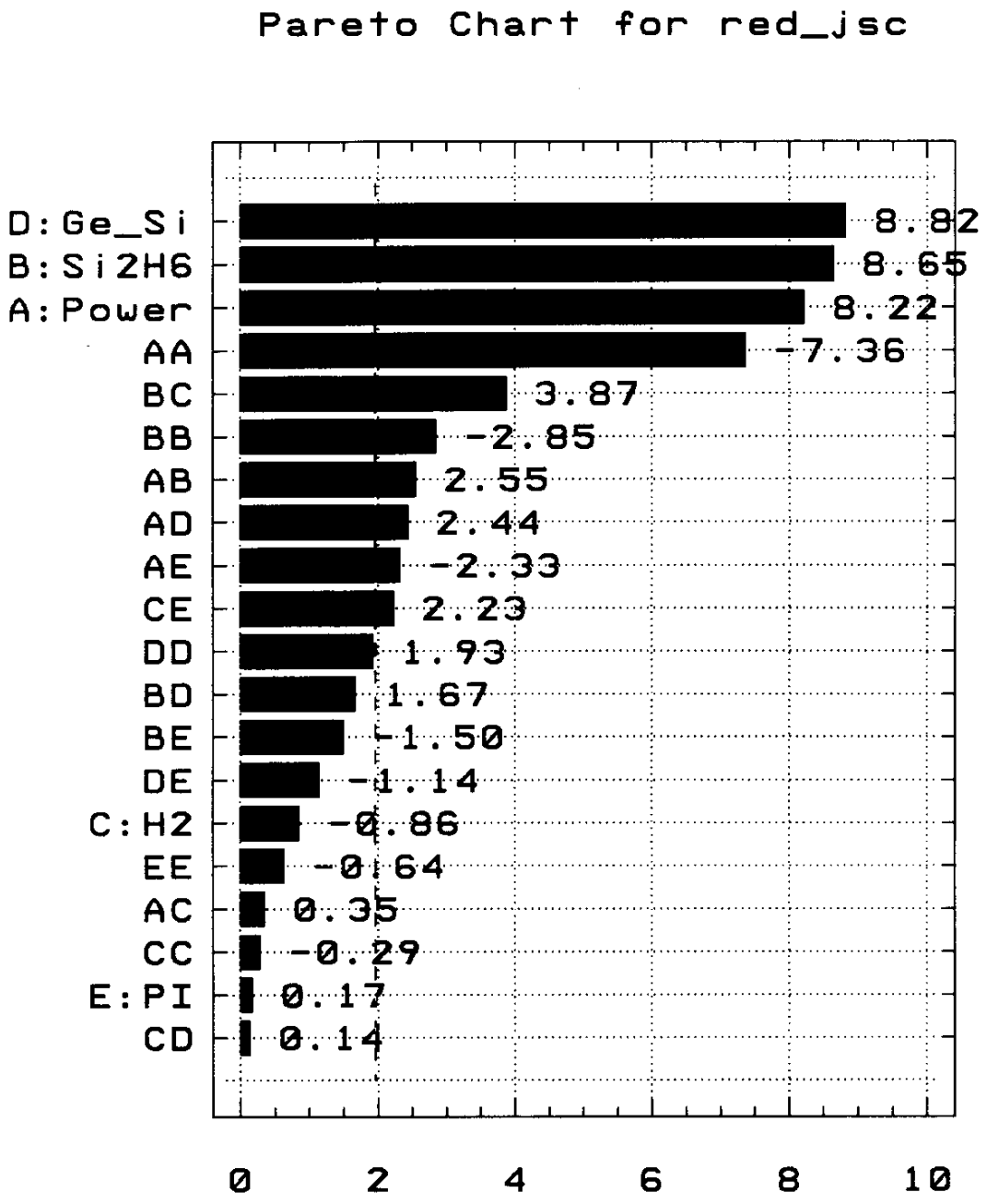

Figure 14-7 Pareto chart for J_{sc} of middle a-SiGe solar cell measured under 530 nm filtered light, for the 5-factor middle cell experimental design.

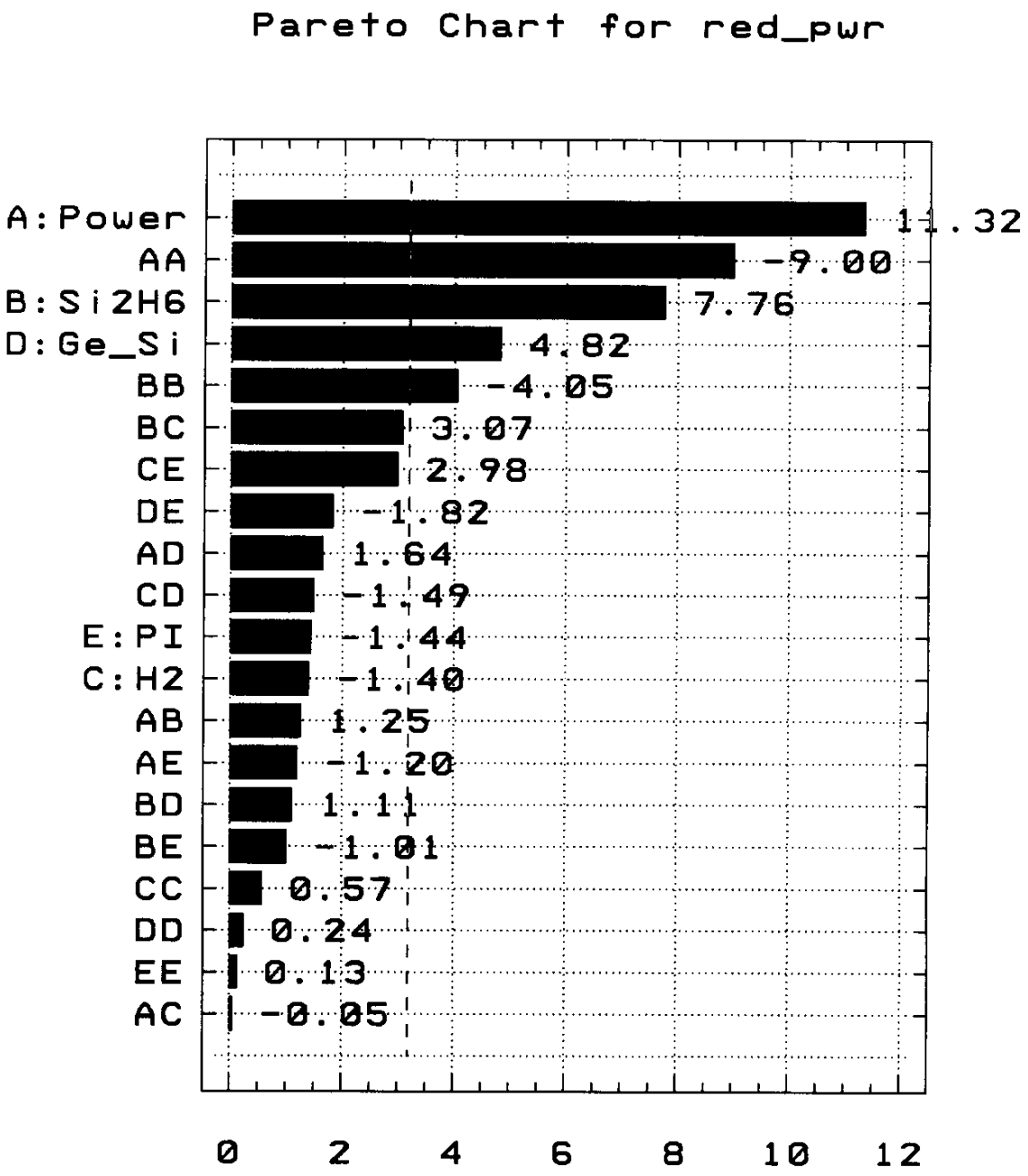

Figure 14-8 Pareto chart for red P_{max} of middle a-SiGe solar cell in the 5-factor middle cell experimental design.

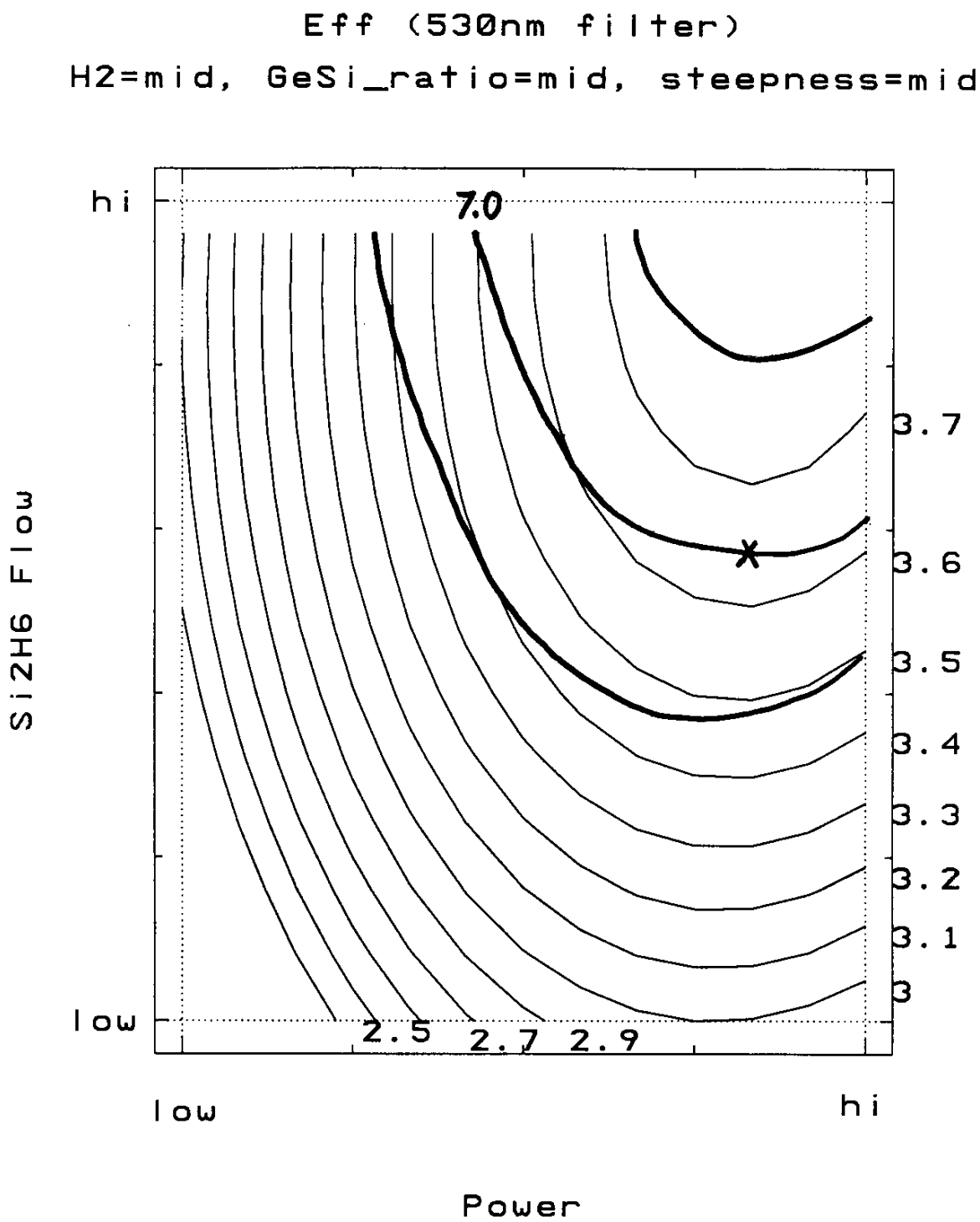

Figure 14-9 Contour plot of the P_{max} as a function of the applied power and Si_2H_6 flow for middle Ge/Si ratio. The dark lines represent the contours with the same J_{sc} value, as marked. The point with the highest P_{max} on the 7.0 mA/cm^2 J_{sc} contour line is marked by a cross, indicating a P_{max} value of 3.64 mW/cm^2.

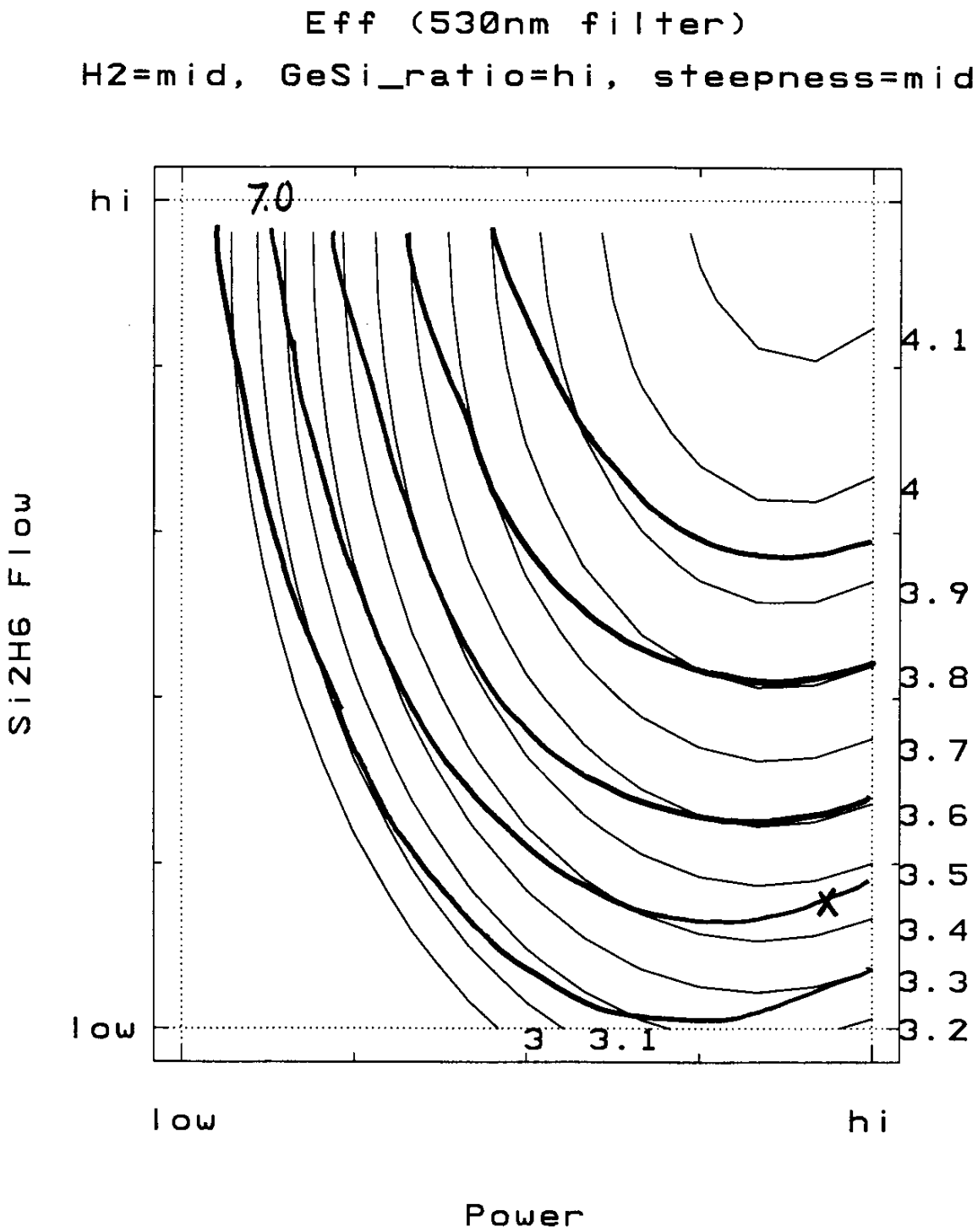

Figure 14-10 Contour plot of the P_{max} as a function of the applied power and Si_2H_6 flow for relatively higher Ge/Si ratio, compared with the plot in Figure 3-12.

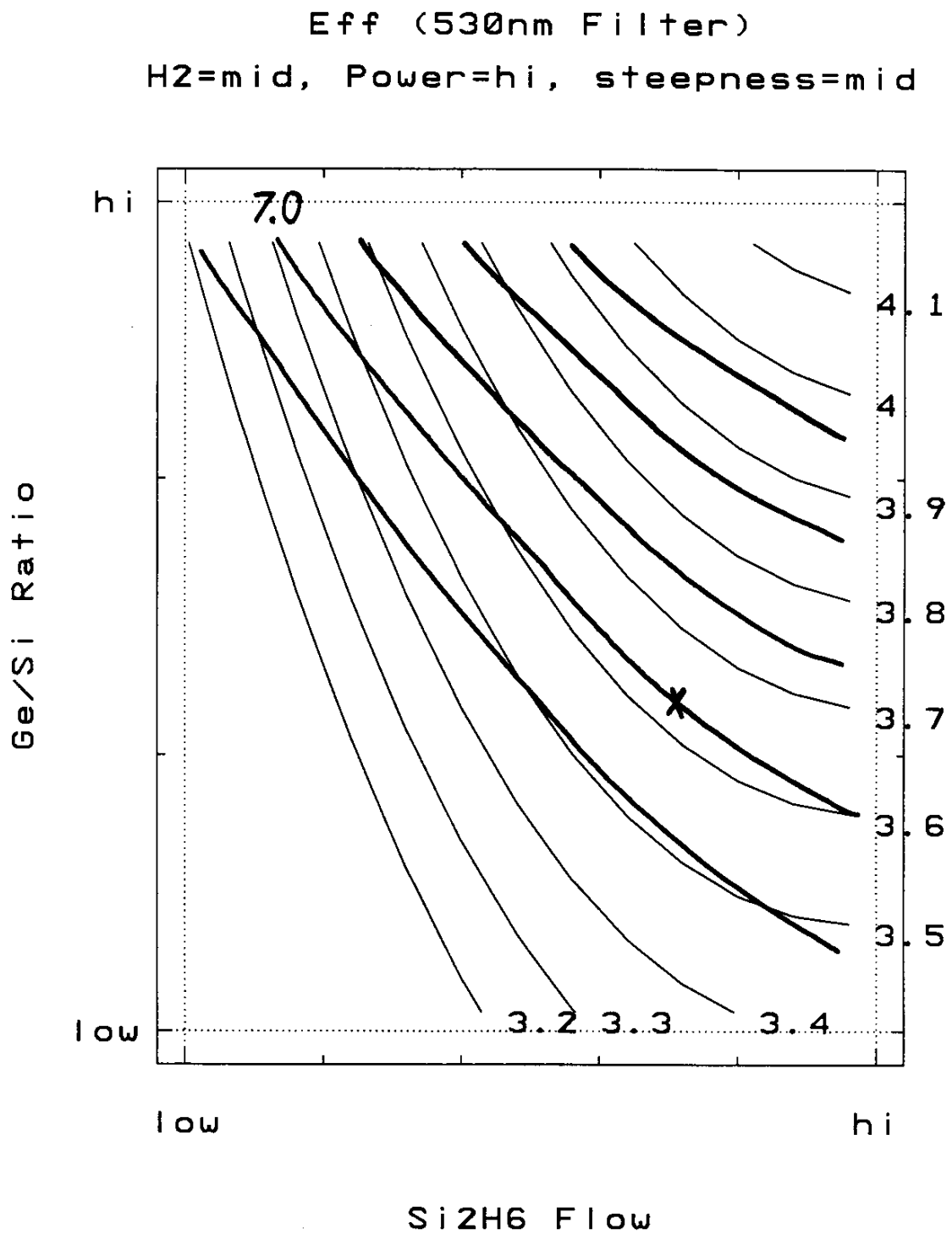

Figure 14-11 Contour plot of the P_{max} as a function of the Si_2H_6 flow and GeH_4/Si_2H_6 ratio with high RF power.

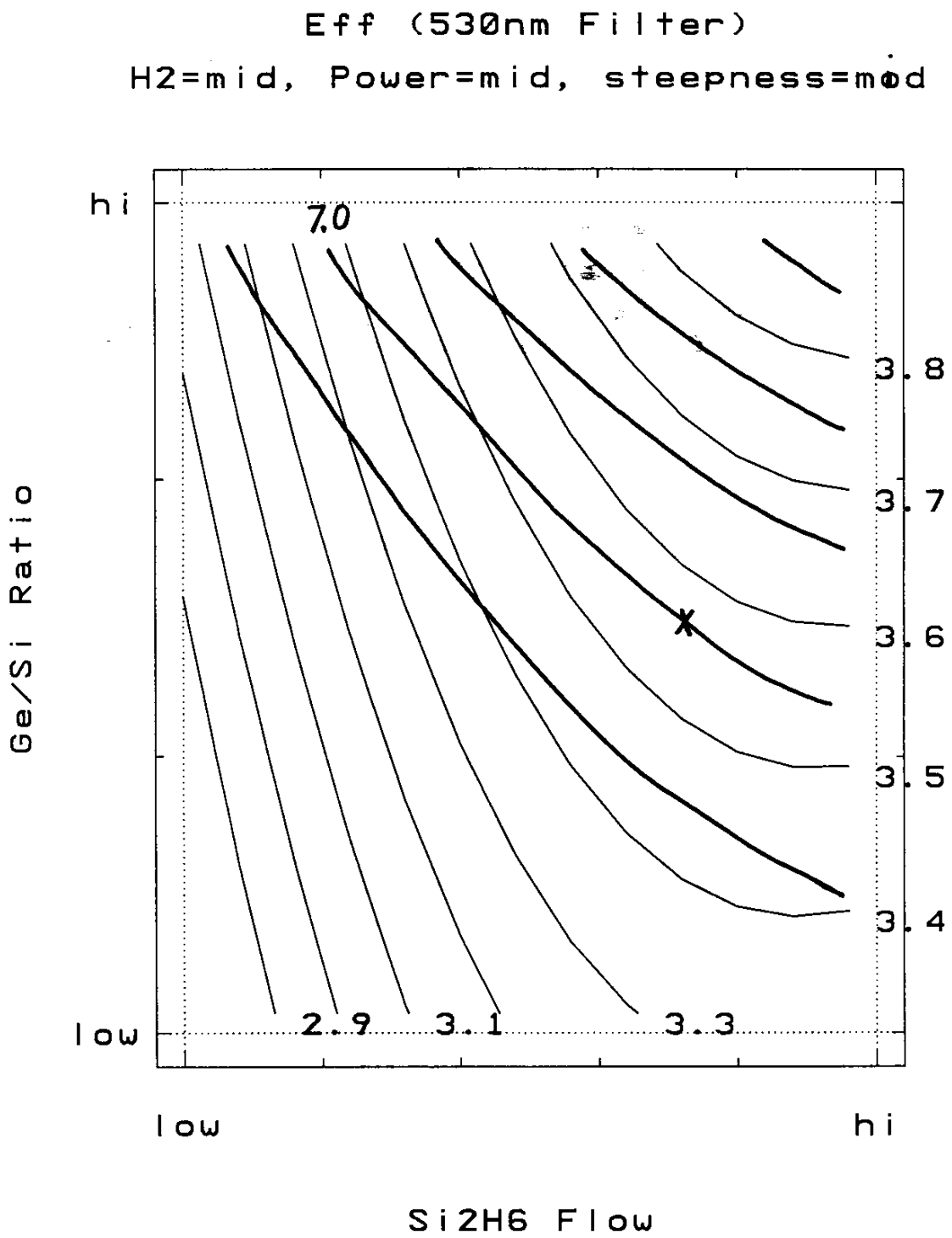

Figure 14-12 Contour plot of the P_{max} as a function of the Si_2H_6 flow and GeH_4/Si_2H_6 ratio with relatively lower RF power.

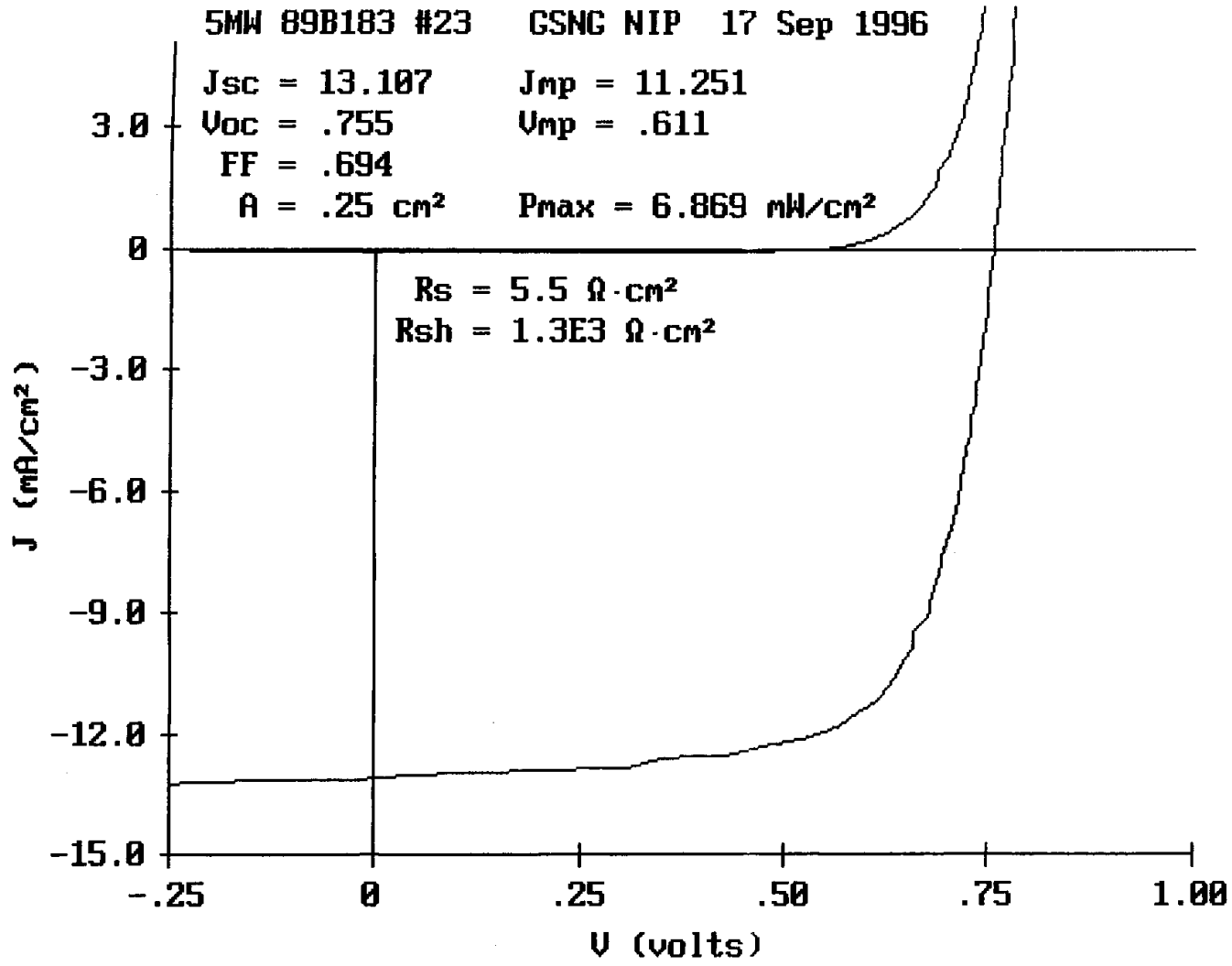

Figure 14-13. J-V curve of a typical a0SiGe middle cell after the preliminary optimization process.

Section 15
Optimization of Large Area Deposition of Ag/ZnO back reflectors

In the ECD/USSC triple-junction solar cell design, a metal/metal-oxide back reflector is used to create multiple passes of photons through the a-Si/a-SiGe/a-SiGe absorbing structure allowing for enhanced absorption of the photons and higher currents. In this report, we limit our discussions to the optimization of Ag/ZnO back-reflector for the 5 MW production line. A reactive magnetron sputtering process is used to prepare the back reflectors. Targets of Ag and ZnO are sputtered in Ar from different sputtering cathodes in this roll-to-roll back-reflector deposition machine.

The deposition of the Ag/ZnO back reflector was optimized to improve its performance. The optimization covers a parameter space of sputtering current, deposition temperature, Ar pressure and the thickness of Ag and ZnO layers. a-SiGe solar cells are deposited on these back-reflectors to evaluate their performance in a solar cell structure. J-V measurements were done on these cells with AM1.5 light and with AM1.5 after a 630 nm and 645 nm long-pass cutoff filters. Table 15-1 displays cell data taken for cells prepared using different ZnO currents and different ZnO targets manufactured by different vendors. In this table, Q is the solar cell short circuit current determined from the integrated quantum efficiency curves over AM1.5 spectrum and P630 is the power determined from the data obtained using the 630 nm filtered light. With increasing ZnO sputtering current, a decrease in J_{sc} is observed, however the FF improves significantly leading to a relatively constant efficiency with increasing ZnO thickness. The increase in FF suggests that we are improving collection with the thicker ZnO layer, however increased absorption by the ZnO lowers the solar cell current.

In another part of the optimization of the Ag/ZnO back reflector, we tested a number of ZnO targets from a variety of vendors to test if one product may be superior over the others. Table 15-2 lists properties for a-SiGe bottom cells deposited in the same deposition run on Ag/ZnO back reflectors made with the ZnO targets manufactured by different vendors L, T and K. As is displayed in the table, the data for the cells prepared with the different ZnO targets are similar within experimental error and are also similar to the reference back reflector used by United Solar for small scale R&D research. This reference back reflector was made under similar conditions to those used to prepare triple-junction cells with world record 14.6% efficiencies. The similarity is also displayed in Figure 15-1 which displays quantum efficiency plots for one of the cells made in the same deposition run on one of the 5MW back reflectors showing a 25.6 mA/cm^2 integrated current from QE and on the reference back reflector. We therefore conclude that the back reflector made in the 5MW line is of high quality.

Table 15-1 Device performance of a-SiGe test solar cells deposited on Ag/ZnO back-reflectors produced in 5MW back-reflector machine with different ZnO sputtering currents.

BR #	Manufacturer	ZnO target	Area	AM1.5 Results				Q>630nm				Q645	FFb	FFr
		Sputter Current		Voc	FF	Q	Rs	Voc	FF	Q	**P630**			
5mw18-**25**	L	Std Current	0.25	0.659	0.458	24.71	13.6	0.621	0.539	11.31	**3.79**	10.36	0.652	0.625
5mw18-**26**		1.5xStd	0.25	0.655	0.547	24.55	7.5	0.616	0.588	10.84	**3.93**	9.86	0.649	0.630
5mw18-**27**		2.0xStd	0.25	0.669	0.563	23.32	7.2	0.627	0.584	10.59	**3.88**	9.61	0.637	0.611
5mw18-**22**	T	Std	0.25	0.645	0.515	25.03	10.8	0.608	0.566	11.44	**3.94**	10.47	0.649	0.621
5mw18-**23**		1.5xStd	0.25	0.640	0.540	24.41	7.2	0.605	0.592	10.98	**3.93**	10.02	0.644	0.617
5mw18-**24**		2.0xStd	0.25	0.648	0.563	24.59	7.2	0.612	0.603	11.09	**4.09**	10.11	0.652	0.635
5mw18-**13**	K	Std	0.25	0.644	0.531	25.16	8.0	0.606	0.575	11.86	**4.13**	10.91	0.639	0.601
5mw18-**14**		1.5xStd	0.25	0.644	0.537	24.58	7.2	0.605	0.588	11.29	**4.02**	10.34	0.642	0.617
5mw18-**15**		2.0xStd	0.25	0.660	0.561	24.30	7.1	0.620	0.595	10.66	**3.93**	9.69		

Table 15-2 Device performance of a-SiGe test solar cells deposited on Ag/ZnO back-reflectors produced in 5MW back-reflector machine using ZnO targets manufactured by different vendors L, T and K.

BR #	Description	Area	AM1.5 Results				Q>630nm				Q645	FFb	FFr
			Voc	FF	Q	Rs	Voc	FF	Q	**P630**			
5mw18-**30**	Manufacture L	0.25	0.655	0.575	24.09	7.2	0.616	0.606	10.83	**4.04**	9.85	0.664	0.643
5mw18-**27**	Manufacture L	0.25	0.669	0.563	23.32	7.2	0.627	0.584	10.59	**3.88**	9.61	0.637	0.611
5mw18-**18**	Manufacture L	0.25	0.672	0.561	24.10	7.8	0.631	0.592	10.65	**3.98**	9.71	0.671	0.641
5mw18-**24**	Manufacture T	0.25	0.648	0.563	24.59	7.2	0.612	0.603	11.09	**4.09**	10.11	0.652	0.635
5mw18-**21**	Manufacture T	0.25	0.650	0.552	24.74	7.1	0.610	0.592	11.33	**4.09**	10.35	0.651	0.632
5mw18-**15**	Manufacturer K	0.25	0.660	0.561	24.30	7.1	0.620	0.595	10.66	**3.93**	9.69		
R2679	Reference	0.25	0.657	0.517	25.11	7.9	0.617	0.578	11.39	**4.06**	10.42	0.636	0.637
R2679	Reference	0.25	0.660	0.541	24.55	5.3	0.625	0.602	11.07	**4.17**	10.12	0.658	0.645
R2679	Reference	0.25	0.657	0.571	24.08	7.1	0.622	0.609	10.7	**4.05**	9.71	0.638	0.625

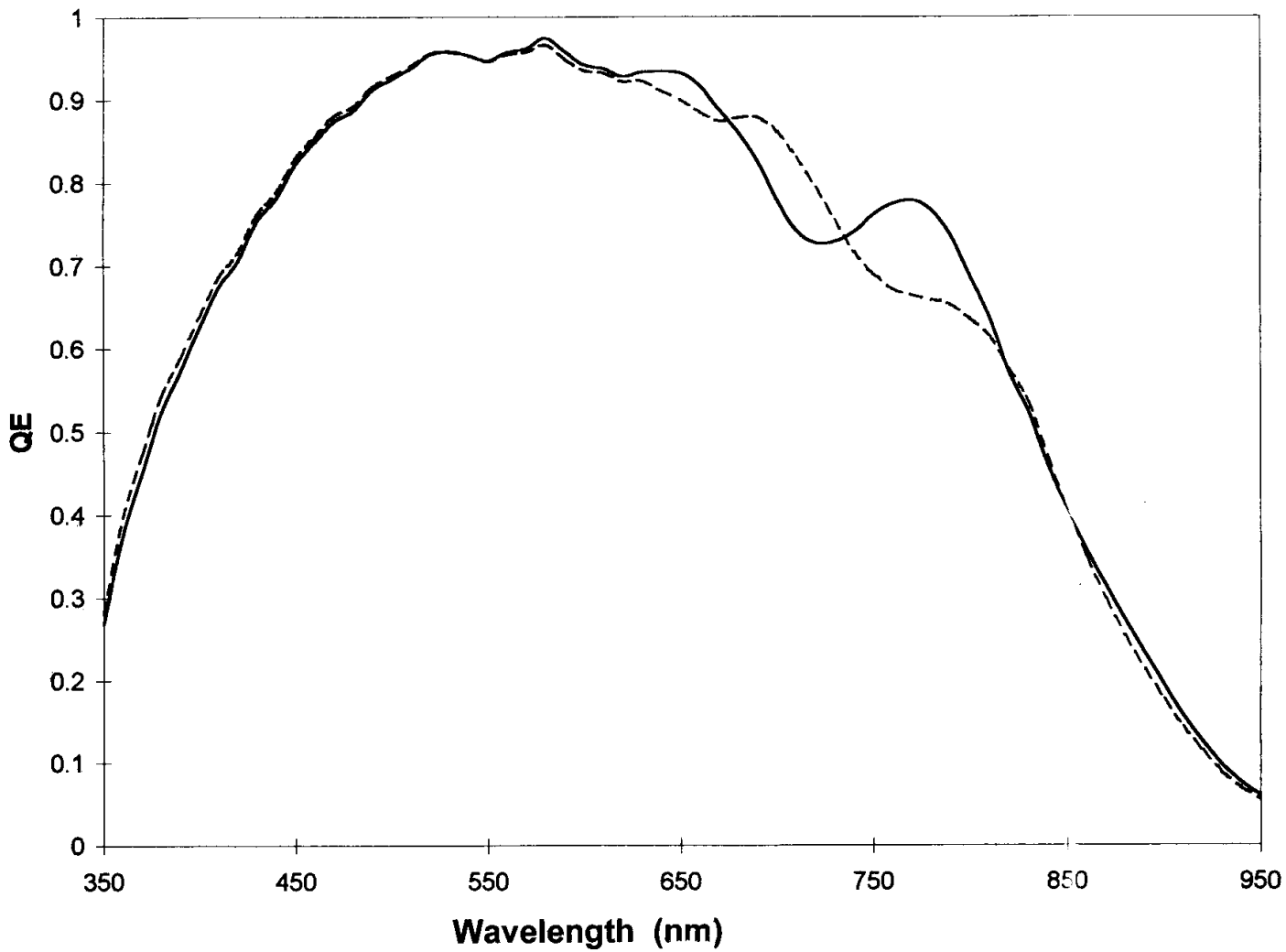

Figure 15-1 QE curves of an a-SiGe solar cell deposited on an optimized Ag/ZnO back-reflector made in the 5MW back-reflector sputtering machine (solid line), showing a J_{sc} of 25.6 mA/cm^2 from the integrated QE, and a reference back-reflector from United Solar's R&D machine (dashed line).

Section 16
Low Cost Deposition of ZnO

In the dc sputtering process presently used to prepare ZnO layers for the metal/ZnO back reflectors in triple-junction structure, ZnO targets are typically used in an Ar atmosphere. However, the cost of these targets is high and contributes a great deal to the overall materials cost for the process. As a cost cutting measure, we have begun a study to test the feasibility of using a Zn metal target reactive sputtering process to prepare ZnO layers for high quality Al/ZnO back reflectors. The cost of a Zn metal target is 1/5 the cost of a ZnO target. In addition to the reduced cost, the use of the Zn metal targets will allow for stable plasmas over a larger range of deposition parameter space as well as higher ZnO deposition rates.

In this process, Zn metal is sputtered in an O_2/Ar gas mixture. To date, we have fabricated over 40 different Al/ZnO back reflectors prepared under various conditions using this new process. The parameters that were varied include the Al and ZnO layer thicknesses, the substrate temperatures, the gas flows and the applied powers. The deposition system used to complete the back reflector fabrication allowed for deposition over a 1 sq. ft. stainless steel substrate. Use of a movable substrate holder allowed for simulation of the movement of the web in our roll-to-roll production process. To test the back reflectors, 2” x 2” pieces were cut from the 1 sq. ft. substrates and a-Si:H single-junction nip solar cells were fabricated using these pieces and a small area R&D semiconductor and ITO/Ag deposition systems. Each system allows for the deposition of layers on four different back reflector pieces in the same deposition run. For each deposition, our standard procedure was to deposit layers on three experimental back reflectors and on a standard back reflector prepared using the 5MW production machine at United Solar.

Table 16-1 below compares the IV data for a-Si:H cells with back reflectors (Zn 39 and Zn 33) prepared using this new technique with the data for a-Si:H cells made using the standard 5MW back reflector(5MWBR78 and 5MWBR82). The semiconductor layers for all of these cells were co-deposited in the same deposition chamber under deposition conditions which were not optimized. ITO and Ag contacts for the cells were also co-deposited in order to minimize any differences in the cells other than the back reflector materials. The data for samples Zn 29, 5MWBR78 and 5MWBR82 are all the same within experimental error. The J_{sc} for sample Zn 33 is higher than the other values, however the FF is lower with an overall slight improvement in efficiency. It can generally be concluded from this data that back reflectors can be made using the new reactive sputtering process which have similar quality to those made using the present 5MW process.

Table 16-1 Comparison of data for a-Si:H cells co-deposited on Al/ZnO back reflectors. Cell measurements completed using AM1.5 light.

Sample	V_{oc} (V)	J_{sc} (mA/cm^2)	FF	P_{max} (mW/cm^2)	R_s (Ωcm^2)
Zn 29	0.952	14.54	0.644	8.91	10.7
Zn 33	0.955	15.06	0.638	9.19	11.5
5MWBR78	0.953	14.45	0.647	8.92	11.9
5MWBR82	0.953	14.30	0.646	8.80	12.5

References

1. S. R. Ovshinsky, J. of Non-Cryst. Solids, 32, 17 (1979), and papers in book series Disordered Materials, published by Institute for Amorphous Study.

2. M. Izu and S. R. Ovshinsky, SPIE Proc. 407, 42 (1983).

3. J. Yang, R. Ross, T. Glatfelter, R. Mohr, G. Hammond, C. Bernotaitis, E. Chen, J. Burdick, M. Hopson and S. Guha, Proc. 20th IEEE PV. Spec. Conf. 241 (1988).

4. S. Guha, J. Yang, P. Nath, and M. Hack, Appl. Phys. Lett. 49, 218 (1986).

5. J. Yang, R. Ross, T. Glatfelter, R. Mohr and S. Guha, MRS Proc. 149, 435 (1989).

6. X. Deng, E. Mytilineou, R.T. Young and S. R. Ovshinsky, MRS Proc. 258, 491 (1992).

7. M. Izu, X. Deng, A. Krisko, K. Whelan, R. Young, H.C. Ovshinsky, K.L. Narasimhan and S.R. Ovshinsky, proc. 23rd IEEE PV Spec. Conf., 919 (1993).

8. X. Deng, M. Izu, K. L. Narasimhan and S. R. Ovshinsky, MRS Proc. 336, 699 (1994).

9. S. Guha, J. Yang, A. Banerjee, T. Glatfelter, K. Hoffman, S. R. Ovshinsky, M. Izu, H.C. Ovshinsky, and X. Deng, Proc. MRS Proc. 336, 645 (1994).

10. X. Deng, K. L. Narasimhan, J. Evans, M. Izu and S. R. Ovshinsky, Proc. of first World Conference on Photovoltaic Energy Conversion (WCPEC), 678 (1994).

11. M. Izu, H. C. Ovshinsky, X. Deng, A. J. Krisko, K. L. Narasimhan, R. Crucet, T. Laarman, A. Myatt, and S. R. Ovshinsky, Proc. of first WCPEC, 820 (1994).

12. X. Deng, S. J. Jones, K. L. Narasimhan, J. Evans, and M. Izu, MRS Proc., 377, 803 (1995).

13. X. Deng, Annual Subcontract Report, FY 1995 (February 1996) NREL/TP-411-20689, 86 (1996).

14. J. Yang, A. Banerjee, S. Guha, in Proc. of NREL/SNL Photovoltaic Program Review Meeting, Nov. 18-22, 1996, Lakewood, CO.

15. M. Izu, H. C. Ovshinsky, S. R. Ovshinsky, in Proc. of NREL/SNL Photovoltaic Program Review Meeting, Nov. 18-22, 1996, Lakewood, CO.

16. J. C. Knights, R. A. Lujan, M. P. Rosenblum, R. A. Street, and D. K. Bieglesen, Appl. Phys. Lett., 38, 331 (1981).

17. T. Aoki, S. Kato, M. Hirose and Y. Nishikawa, Jpn J. of Appl. Phys. 28, 849 (1989).

18. W. A. Turner, S.J. Jones, D. Pang, B.F. Bateman, J.H. Chen, Y.-M. Li, F.C. Marques, A.E. Wetsel, P. Wickboldt, and W. Paul, J. of Appl. Phys., 67, 7430 (1990).

19. F. H. Karg, H. Bohm and K. Pierz, J. of Non-Cryst. Solids, 114, 477 (1989).

20. S. Guha, X. Xu, J. Yang, and A. Banerjee, MRS Proc. 377, 621 (1995).

21. X. Xu, J. Yang, S. Guha, 23rd IEEE PVSC, 971 (1993).

22. Y. M. Li, MRS Proc., 297, 803 (1993), and the references therein.

23. S. Guha, K. L. Narasimhan, and S. M. Pietruzko, J. Appl. Phys. 52, 859 (1981).

24. K. Tanaka and A. Matsuda, Mat. Sci. Report, 2, 139 (1987).

25. J. Yang, X. Xu, and S. Guha, MRS Proc. 336, 687 (1994).

26. L. Yang and L. Chen, MRS Proc. 336, 669 (1994).

27. X. Deng, Phil. Mag. Lett., 61, 281 (1990); W. Spear, and M. Heintze, Phil. Mag. B, 54, 343 (1986).

28. D.L. Williamson, MRS Proc. 377, 251 (1995).

29. S. Fujikake, H. Ohta, A. Asano, Y. Ichikawa and H. Sakai, MRS Symp. Proc. 258, 875 (1992).

30. Y. Ichikawa, S. Fujikake, H, Ohta, T. Sasaki and H. Sakai, 22nd IEEE PVSC, 1296 (1991).

31. W. Ma, T. Saida, C.C. Lim, S. Aoyama, H. Okamoto and Y. Hamakawa, Proc. of 1st WCPEC, 417 (1995).

32. C. R. Wrohski, D. E. Carlson, and R. E. Daniel, Appl. Phys. Lett., 29, 602 (1976)

33. M. Thompson, R. J. Nemanich, and C. C. Tsai, Surface Sci., Vol. 132, 250 (1983).

34. M. Thompson, R. J. Nemanich, and C. C. Tsai, Surface Sci., Vol. 132, 250 (1983).

35. M. Heintze, R. Zedlitz and S.H. Bauer, Mat. Res. Soc. Proc 297, 49 (1993).

36. J. Meier, et. Al, Proc. of 1st WCPEC, 409 (1994).

37. S.J. Jones, X. Deng, T. Liu, M. Izu, MRS Proceedings 1998 (to be published).

38. F. Finger et al., Appl. Phys. Lett, 65, 2588 (1994).

39. M. Heintze, R. Zedlitz and S.H. Bauer, MRS Proc. 297, 49 (1993).

40. For this study, we mostly used Statgraphics Plus software by Manugistics, Inc., Version 7, (1993).

41. X. Deng, S.J. Jones, T. Liu, M. Izu, S.R. Ovshinsky and K. Hoffman, MRS Proc. 467, 795 (1997).

42. In collaboration with J. Yang and S. Guha at United Solar Systems Corp.

REPORT DOCUMENTATION PAGE

Form Approved
OMB NO. 0704-0188

Public reporting burden for this collection of information is estimated to average 1 hour per response, including the time for reviewing instructions, searching existing data sources, gathering and maintaining the data needed, and completing and reviewing the collection of information. Send comments regarding this burden estimate or any other aspect of this collection of information, including suggestions for reducing this burden, to Washington Headquarters Services, Directorate for Information Operations and Reports, 1215 Jefferson Davis Highway, Suite 1204, Arlington, VA 22202-4302, and to the Office of Management and Budget, Paperwork Reduction Project (0704-0188), Washington, DC 20503.

AGENCY USE ONLY (Leave blank)	2. REPORT DATE April 1998	3. REPORT TYPE AND DATES COVERED Final Technical Report

TITLE AND SUBTITLE
Development of High, Stable-Efficiency Triple-Junction a-Si Alloy Solar Cells

5. FUNDING NUMBERS
C: ZAN-4-13318-11
TA: PV804401

AUTHOR(S)
X. Deng, S.J. Jones, T. Liu, and M. Izu

PERFORMING ORGANIZATION NAME(S) AND ADDRESS(ES)
Energy Conversion Devices, Inc.
1675 West Maple Road
Troy, Michigan 48084

8. PERFORMING ORGANIZATION REPORT NUMBER

SPONSORING/MONITORING AGENCY NAME(S) AND ADDRESS(ES)
National Renewable Energy Laboratory
1617 Cole Blvd.
Golden, CO 80401-3393

10. SPONSORING/MONITORING AGENCY REPORT NUMBER
SR-520-24580

SUPPLEMENTARY NOTES
NREL Technical Monitor: K. Zweibel

DISTRIBUTION/AVAILABILITY STATEMENT

12b. DISTRIBUTION CODE
UC-1262

ABSTRACT *(Maximum 200 words)*
This report summarizes Energy Conversion Devices, Inc.'s (ECD) research under this program. ECD researchers explored the deposition of a-Si at high rates using very-high-frequency plasma MHz, and compared these VHF i-layers with radio-frequency (RF) plasma-deposited i-layers. ECD conducted comprehensive research to develop a Fc-Si p^+ layer using VHF deposition process with the objectives of establishing a wider process window for the deposition of high-quality p^+materials and further enhancing their performance of a-Si solar cells by improving its p-layers. ECD optimized the deposition of the intrinsic a-Si layer and the boron-doped Fc-Si p^+ layer to improve the V_{oc}. Researchers deposited wide-bandgap a-Si films using high hydrogen dilution; investigated the deposition of the ZnO layer (for use in back-reflector) using a sputter deposition process involving metal Zn targets; and obtained a baseline fabrication for single-junction a-Si n-i-p devices with 10.6% initial efficiency and a baseline fabrication for triple-junction a-Si devices with 11.2% initial efficiency. ECD researchers also optimized the deposition parameters for a-SiGe with high Ge content; designed a novel structure for the p-n tunnel junction (recombination layer) in a multiple-junction solar cell; and demonstrated, in n-i-p solar cells, the improved stability of a-Si:H:F materials when deposited using a new fluorine precursor. Researchers investigated the use of c-Si(n^+)/a-Si alloy/Pd Schottky barrier device as a tool for the effective evaluation of photovoltaic performance on a-Si alloy materials. Through alterations in the deposition conditions and system hardware, researchers improved their understanding for the deposition of uniform and high-quality a-Si and a-SiGe films over large areas. ECD researchers also performed extensive research to optimize the deposition process of the newly constructed 5-MW back-reflector deposition machine.

SUBJECT TERMS
photovoltaics ; a-Si alloy solar cells ; amorphous silicon solar cells ; triple-junction solar cells ; Schottky barrier device ; wide-bandgap a-Si films ; narrow bandgap materials and devices ; a-Si deposition

15. NUMBER OF PAGES
154

16. PRICE CODE

SECURITY CLASSIFICATION OF REPORT	18. SECURITY CLASSIFICATION OF THIS PAGE	19. SECURITY CLASSIFICATION OF ABSTRACT	20. LIMITATION OF ABSTRACT
Unclassified	Unclassified	Unclassified	UL